RESERVOIR CHARACTERIZATION COMBINING ELASTIC VELOCITIES AND ELECTRICAL RESISTIVITY MEASUREMENTS

A DISSERTATION

SUBMITTED TO THE DEPARTMENT OF GEOPHYSICS

AND THE COMMITTEE ON GRADUATE STUDIES

OF STANFORD UNIVERSITY

IN PARTIAL FULFILLMENT OF THE REQUIREMENTS

FOR THE DEGREE

OF DOCTOR OF PHILOSOPHY

Carmen Teresa Gomez

July 2009

I certify that I have read this dissertation and that, in my opinion, it is fully adequate in scope and quality as a dissertation for the degree of Doctor of Philosophy.

_____

Gary Mavko (Principal Adviser)

I certify that I have read this dissertation and that, in my opinion, it is fully adequate in scope and quality as a dissertation for the degree of Doctor of Philosophy.

_____

Jack Dvorkin

I certify that I have read this dissertation and that, in my opinion, it is fully adequate in scope and quality as a dissertation for the degree of Doctor of Philosophy.

_____

Tiziana Vanorio

I certify that I have read this dissertation and that, in my opinion, it is fully adequate in scope and quality as a dissertation for the degree of Doctor of Philosophy.

_____

Tapan Mukerji

Approved for the University Committee on Graduate Studies

Abstract

The elastic and electric parameters of rocks that can be obtained from seismic and electromagnetic data depend on porosity, texture, mineralogy, and fluid. However, seismic data seldom allow us to accurately quantify hydrocarbon saturation. On the other hand, in the case of common reservoir rocks (i.e., sandstones and carbonates), resistivity strongly depends on porosity and saturation. Therefore, the recent progress of controlled-source-electromagnetic (CSEM) methods opens new possibilities in identifying and quantifying potential hydrocarbon reservoirs, although its resolution is much lower than that of seismic data. Hence, a combination of seismic and CSEM data arguably offers a powerful means of finally resolving the problem of remote sensing of saturation. The question is how to combine the two data sources (elastic data and electrical resistivity data) to better characterize a reservoir.

To address this question, we introduce the concept of P-wave impedance and resistivity templates as a tool to estimate porosity and saturation from well log data. Adequate elastic and resistivity models, according to the lithology, cementation, fluid properties must be chosen to construct these templates. These templates can be upscaled to seismic and CSEM scale using Backus average for seismic data, and total resistance for CSEM data.

We also measured velocity and resistivity in Fontainebleau samples in the laboratory. Fontainebleau formation corresponds to clean sandstones (i.e., low clay content). We derived an empirical relation between these P-wave velocity and resistivity at 40MPa effective pressure, which is around 3 km depth at normal pressure gradients. We were not able to test if this relation could be used at well or field data scales (once appropriate upscaling was applied), since we did not have a field dataset over a stiff sandstone reservoir.

A relationship between velocity and resistivity laboratory data was also found for a set of carbonates. This expression was quadratic, and not linear as in the case of Fontainebleau sandstones. There are other factors that influence this relationship in the case of these carbonates, which include pore geometry, and amount of micritic cement. We observed that the expression is almost linear, but it deviates as we approach lower resistivities. This deviation can be explained by the presence of stiff pores such as moldic or intra-granular pores, which causes high velocity but low resistivity values when water-saturated. In the same way, the effect of micrite cement on velocity is stronger than its effect on resistivity, and that also is responsible for some of the scatter that we observe.

We also modeled both velocity and resistivity using self-consistent approximation with the same pore or inclusion geometries in both carbonate and sandstone laboratory datasets. In the case of carbonates, we found that we had to include needle-like pores to explain the low resistivity but high velocities. Needle is one of the geometries that allow us to have connected stiff pores. However, we also found that a fraction of compliant pores also had to be included in order to explain the velocity measurements on the carbonate dataset. The self-consistent model also approximated well the velocity and resistivity laboratory measurements on the Fontainebleau sandstones, using similar aspect ratios for both the velocity and the resistivity.

As far as semi-empirical and empirical models, we observed how the stiff-sand model fit well the Fontainebleau data at 40MPa, including S-wave velocities. The Raymer-Hunt-Gardner relation also did a good job at predicting P-wave velocity. Archie's equation with cementation exponent between 1.6 and 2.1 fits the resistivity measurements

on the Fontainebleau sandstones. These two relationships can be combined to create a resistivity – P-wave velocity transform for this dataset.

When we attempted to use CSEM data to limit the shallow and low-frequency acoustic impedance trend for seismic inversion, we found that appropriate elastic and resistivity models must be chosen in order to have a good prediction of acoustic impedance, given resistivity. These expressions can be calibrated using well data with particular emphasis to the overburden. If no well log data are available in the shallow section, using the CSEM-derived resistivity data and an adequate cross-property relation (for example, one based on soft-sand model and Archie's equation) can be a good approach to predict the initial low frequency shallow acoustic impedance model. Validation tests showed that using the background trend from CSEM data as a constraint in impedance inversion can give a better fit to the acoustic impedance.

As part of our analysis of gas hydrate bearing sandstones, we found that normalized resistivity versus P-wave impedance templates can also be useful to predict reservoir properties, such as porosity and saturation for a gas-hydrate reservoir at well log scale. Porosity and saturation prediction of the hydrate-bearing layer from seismic data alone is highly dependent on its thickness and the properties of the overburden, and requires well-control data that can point to appropriate models and properties to use for the overburden. However, it would be interesting to test, using a resistivity model obtained from seismic data as the initial input, a CSEM inversion on a gas-hydrate-bearing sandstone.

Acknowledgments

I would like to start by thanking my committee, Jack Dvorkin, Gary Mavko, Tapan Mukerji, and Tiziana Vanorio. I have learned a lot from each of you in my time here. Jack, thanks for your encouragement and advice. Gary, I appreciate a lot your teaching and advice. Tapan, thanks for always having so many interesting suggestions. Tiziana, thanks for your patience and all your help in the lab.

I would also like to thank Rosemary Knight, who taught me a lot in her class, and also while she was a member of my committee. Thanks to Barry Kirkendall, who took some his valuable time to help me better understand some of the lab equipment. Thanks to Steve Graham, and Biondo Biondi, who also took part in some of my annual reviews, asking interesting questions and making good suggestions.

Thanks to the SRB program, their sponsors and also to the SEG Foundation for their support during these four years. Thanks to Tara Illich and Fuad Nijim for their help with all administrative problems that I came across during my time at Stanford.

OHM/RSI and TGS-NOPEC provided some of the data, in particular, Lucy MacGregor and Peter Harris were very helpful. Thanks to Hampson-Russell for providing their software to Stanford University. Bernard Zinszner at the Institut Français du Pétrole provided some of the samples I worked with. I would like to acknowledge Ingrain, Inc. for providing some of the CT scan images. Thanks to Tim Collett, U.S. Geological Survey, for providing some of the data on hydrates.

Marco Voltolini at the University of California, Berkeley made some of the XRD measurements on carbonates shown in Chapter 4. Other XRD measurements and velocity measurements on carbonates were performed by Cinzia Scotellaro, a post-doc in SRB, and now at British Gas. I would also like to thank Stéphanie Vialle, currently working in SRB, for her help with mercury porosimetry measurements.

Thank you to Franklin Ruiz and Ezequiel González. It was nice to meet fellow Venezuelans in SRB, who made me feel welcome. I would also like to thank my officemates: Ramil Ahmadov, and Kevin Wolf. Thanks to all other SRB members I met and learnt from during this time: Kyle Spikes, Kyle Spratt, Kaushik, Ratna, Richa, Tanima, Piyapa, Huyen, Danica.

A few people who I do not see that often anymore, but that I have to thank a great deal are Milagrosa Aldana, John Pigott, John Castagna, Robert Tatham, and Mrinal Sen. They encouraged me to come to Stanford, and I learned a lot from them.

Finally, thanks to all my family and friends, in particular to my mom. Everything that I am is thanks to her. Thanks also to my godmother, my dad, and so many good friends, and a numerous family in Venezuela.

Contents

Abstract…..…..…..

List of Tables

List of Figures

Chapter 1
Introduction

1.1 Motivation and objectives

The elastic and electric parameters of rocks that can be obtained from seismic and electromagnetic data depend on porosity, texture, mineralogy, and fluid. However, seismic data seldom allow us to accurately quantify hydrocarbon saturation. On the other hand, in the case of common reservoir rocks (i.e., sandstones and carbonates), resistivity strongly depends on porosity and saturation. Therefore, the recent progress of controlled-source-electromagnetic (CSEM) methods opens new possibilities in identifying and quantifying potential hydrocarbon reservoirs, although its resolution is much lower than that of seismic data. Hence, a combination of seismic and CSEM data arguably offers a powerful means of finally resolving the problem of remote sensing of saturation. The question is how to rigorously combine the two data sources (elastic data and electrical resistivity data) to arrive at the desired product of porosity and hydrocarbon saturation (i.e., hydrocarbon volume).

The objective of this research study is to develop a methodology for reservoir characterization that incorporates both seismic and resistivity measurements. Analyzing electric and elastic data jointly could help us improve estimates of fluid saturation, and to better describe the pore structure of a rock.

Rock properties such as mineralogical composition, porosity, fluid saturation, pore geometry, as well as their dependence on pressure and temperature affect both the elastic and the electrical properties of rocks. The existence of such relationships provides the foundation for predicting rock properties, and their changes under reservoir conditions, from *in situ* measured physical data.

Rock physics has played a fundamental role in the last decades to understand the relationships between rock properties and their effects on seismic (see Nur and Wang, 1989; Wang and Nur, 1992; Wang and Nur, 2000, for a comprehensive review) and electrical data (e.g., Mavko et al., 1998; and Knight and Endres, 2005, for a comprehensive review). The general objective of rock physics aims at understanding how to translate basic rock properties to geophysical observables (and vice versa) for an enhanced exploration and characterization of the Earth's subsurface.

Our ability to predict rock properties depends on the reliability of such relationships as well as on the limitations of each method. Both seismic and electrical methods, in fact, show inherent limitations that are mostly related to the sensitivity of the velocity and resistivity to a given rock property. Moreover, due to the complexity of the rock system, the inversion of its properties from in-situ measured physical observables is inherently an underdetermined problem. There is, thus, the need to

improve our ability to describe the physical behavior of porous rocks in order to enhance the characterization of rock formations. A way to improve the characterization of rock formations is by increasing the number of *in-situ* physical observables so that their joint inversion in terms of rock properties becomes less non-unique. This calls for the development of physics-based relationships between the acoustic and electric properties to be used for the inversion procedures. One goal of this work is to develop, explore, and verify such relationships by controlled laboratory experiments and theoretical modeling.

Applying laboratory observations and theory at well logging or at surface seismic reflection or CSEM scales is not straightforward. The scales of these datasets are very different; and seismic and resistivity anisotropy and dispersion may play an important role when upscaling. Therefore, one interesting question to address would be: Can we use the same models of elastic and electrical properties, at these very different scales, to estimate reservoir properties? At the well log scale, many available models have already been tested, and prove their effectiveness in certain situations, and their weakness in others. But, it is also interesting to attempt predictions of porosity and saturation at the seismic and CSEM scales using these models.

1.2 Chapter description

Chapter 2 introduces the concept of P-wave impedance – resistivity templates, as a useful tool to combine the analysis of elastic and resistivity data at the well log scale, and also shows the effect of upscaling to seismic and CSEM scales by forward modeling assuming a sand wedge in a shaly background. Different common

geological scenarios are assumed to perform this modeling and observe the effect that the thickness of the reservoir has on our ability to predict its properties using seismic and CSEM data. This work was published in *The Leading Edge* with contributions from Jack Dvorkin and Gary Mavko (Gomez et al., 2008).

Chapter 3 is a study of resistivity, P- and S-wave velocities and their relationships to porosity and permeability in Fontainebleau sandstones. We review relations between porosity and permeability. We measure resistivity as a function of the salinity of the saturating fluid to identify the main mechanism of electrical conduction in these rocks. We then model resistivity as a function of porosity and permeability, and analyze the relationship between these properties. P- and S-wave velocities are also measured as a function of confining pressure, and their relationship with porosity is also modeled. Finally, we also study the relation between velocity and resistivity. Tiziana Vanorio provided suggestions and assistance in the laboratory for this work. Jack Dvorkin contributed in the modeling and analysis.

Chapter 4 describes how velocity and resistivity relate in the case of a carbonate dataset, using controlled laboratory measurements of these properties. We observe how effective medium modeling can help us identify general characteristics of the pore space that will be consistent with the velocity and resistivity measurements. It also shows that since velocity and resistivity are related through porosity, there is a relation between these two properties, but it is actually a very complex one, and also involves permeability, pore shape, and grain size. This work was performed in the Stanford Rock Physics Laboratory with assistance of Tiziana Vanorio and Cinzia

Scotellaro. Jack Dvorkin and Gary Mavko gave suggestions in the analysis of the data. Some of this work has been accepted as a presentation and abstract in the *2009 Society of Exploration Geophysicists (SEG) Annual Meeting.*

Chapter 5 is a review and modeling chapter where we describe the controlled-source electromagnetic (CSEM) technique, which is currently used to measure resistivity remotely offshore. We do not process field EM data, but we work with these data, therefore it is important to understand the principles behind it. To accomplish this, we perform forward EM modeling, and also forward seismic modeling and compare the resolution of these two techniques.

Chapter 6 is an application to field data of the rock physics P-wave impedance – resistivity templates. We also show how templates can be upscaled and used with field data to predict porosity and saturation. We demonstrate how to integrate the interpretation of seismic and EM data to predict reservoir properties, using seismic impedance and CSEM resistivity sections. This work was published in *The Leading Edge* with contributions from Jack Dvorkin and Gary Mavko (Gomez et al., 2008).

Chapter 7 presents a different way of integrating seismic and CSEM data, by using the CSEM-derived resistivity to estimate a low frequency P-wave impedance trend to use as initial input for seismic inversion. It can be difficult to define an initial model for acoustic impedance for seismic inversion, in particular in the shallow section where no well log data may be present. CSEM data can help define an initial acoustic impedance model, in particular in the shallow interval, using a rock physics resistivity – P-wave impedance transform. The initial idea for this work was published in *The*

Leading Edge together with Tapan Mukerji, and Gary Mavko (Mukerji et al., 2009). Later progress will be published in the *2009 SEG Annual Meeting Abstract Volume*.

Chapter 8 is a forward modeling catalogue of gas hydrate reservoirs. When inverting EM data in an area where gas hydrates are present, any prior information we can obtain from seismic data can be very useful. We model P-wave impedance as a function of porosity and gas hydrate saturation, in order to predict resistivity. We study the role of seismic resolution and the properties of the overburden in our ability to predict resistivity from seismic attributes. Jack Dvorkin contributed in the modeling and analysis included in this chapter as well.

Chapter 9 presents conclusions, and summarizes our results, and discusses them in an integrated framework, particularly how to use different approaches to combine elastic and resistivity data to help in understanding and estimation of reservoir properties.

Chapter 2
Hydrocarbon Volume Estimate from Elastic and Resistivity Data

2.1 Abstract

The volume of hydrocarbon in place, which is the product of porosity and saturation, is the ultimate target of exploration and development. Seismic reflections depend on the contrasts of the elastic properties (impedance and velocity), which, in turn, are predominantly affected by porosity and mineralogy. On the other hand, resistivity, which is one of the quantities provided by electromagnetic methods, strongly reacts to a combination of porosity and saturation. The latter is impossible to estimate without making an assumption about the former. Neither seismic nor resistivity data, if analyzed separately, can provide the desired estimate of hydrocarbon in place. The question is how to use these two data sources together. We offer a solution by combining two theoretical models, one that relates the elastic-wave velocity to porosity, mineralogy, and pore fluid, and another that relates resistivity to porosity, saturation, cementation and tortuosity. These two models allow us to produce

rock-physics templates of the normalized resistivity versus acoustic impedance that serve to solve for porosity and saturation from these two inputs. We show examples of such templates for a sandstone reservoir with methane hydrate as well as with oil and gas. This concept is based on rock-physics models and, therefore, is amenable to upscaling, which is required to interpret field measurements. We show how the thickness of the reservoir plays an important role in the effectiveness of this technique at the field scale.

2.2 Introduction

The volume of hydrocarbon in place, which is the product of porosity and saturation, is the ultimate target of exploration and development. Currently, reflection-seismic profiling is the most widely used method of exploring the subsurface. Recently electromagnetic remote sensing, such as CSEM (controlled-source electromagnetic profiling), is gaining acceptance in the industry.

Seismic reflections depend on the contrasts of the elastic properties (impedance and velocity) which, in turn, are predominantly affected by porosity and mineralogy. The elastic properties of rock may also strongly depend on the saturation and the type of saturating fluid. However, their dependence on partial hydrocarbon saturation (if the latter is larger than zero and smaller than one) is weak (Figure 2.1). As a result, it is often difficult to extract saturation from seismic data. One of the few successful attempts to extract saturation from seismic data use P-to-S (PS) converted waves, in

particular an attribute called PS elastic impedance (PSEI) at near and far offsets (Gonzalez et al., 2003).

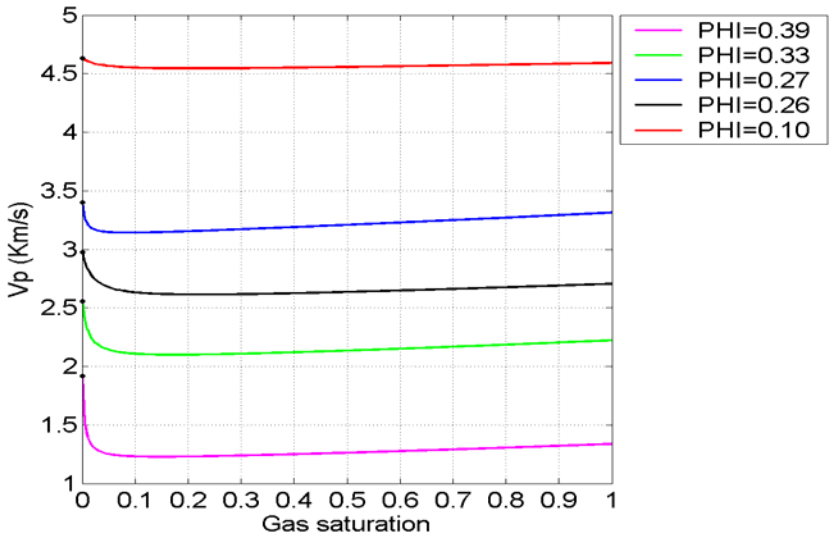

Figure 2.1: P-wave velocity (Km/s) versus gas saturation. Blue and red lines are for sands with porosities (PHI): 0.27 and 0.10 and properties as given in Gomez and Tatham (2007). Pink, green and black lines are sands with porosities (PHI): 0.39, 0.33 and 0.26, and properties as given in Domenico (1974).

On the other hand, resistivity, which is one of the quantities provided by electromagnetic methods, strongly depends on a combination of porosity and saturation, but the latter is impossible to estimate without making an assumption about the former. Therefore, neither seismic nor resistivity data, if analyzed separately, can provide the desired estimate of hydrocarbon in place. The question that we address in this chapter, and through this thesis, is how to integrate these two data sources.

Here we discuss a physics-driven solution which combines two theoretical models, one that relates the elastic-wave velocity to porosity, mineralogy, and pore fluid and

the other that relates resistivity to porosity and saturation. This approach allows us to produce templates of the normalized resistivity versus the acoustic impedance that we use to solve for porosity and saturation from these two inputs. We show examples of such templates for a sandstone reservoir with methane hydrate as well as with oil and gas. Our model-driven templates are flexible: they can be constructed to honor the site-specific rock properties to account for a variety of variables, such as diagenetic cementation and depositional sorting, as well as the presence of shale.

2.3 Rock Physics Impedance – Resistivity Templates

Consider a clean, unconsolidated gas sand in which porosity (ϕ) varies from 0.1 to 0.4 and water saturation (S_w) is between 0.2 and 1.0. In Figure 2.2 we display the elastic properties as computed from the soft-sand model (Dvorkin and Nur, 1996), which is appropriate to describe the elastic properties of unconsolidated sand and shale. We observe that the P-wave impedance (I_P) strongly reacts to ϕ but only weakly depends on S_w, unless $S_w = 1.0$. Poisson's ratio (ν) also helps discriminate between wet and gas-filled sediment but fails to quantify S_w.

Figure 2.3 (left), where the same sand is used, reaffirms the fact that S_w cannot be quantified from I_p. Indeed, the S_w contour lines are essentially vertical for $S_w < 1$. In the same figure (right) we display the normalized resistivity R_t / R_w (R_t is the measured resistivity and R_w is that of water) as calculated from Archie's resistivity equation. S_w strongly reacts to R_t / R_w; however, it cannot be quantified without

knowing ϕ. Indeed, at $R_t / R_w = 100$, S_w can be 0.25 for $\phi = 0.4$ or about 0.70 for $\phi = 0.2$.

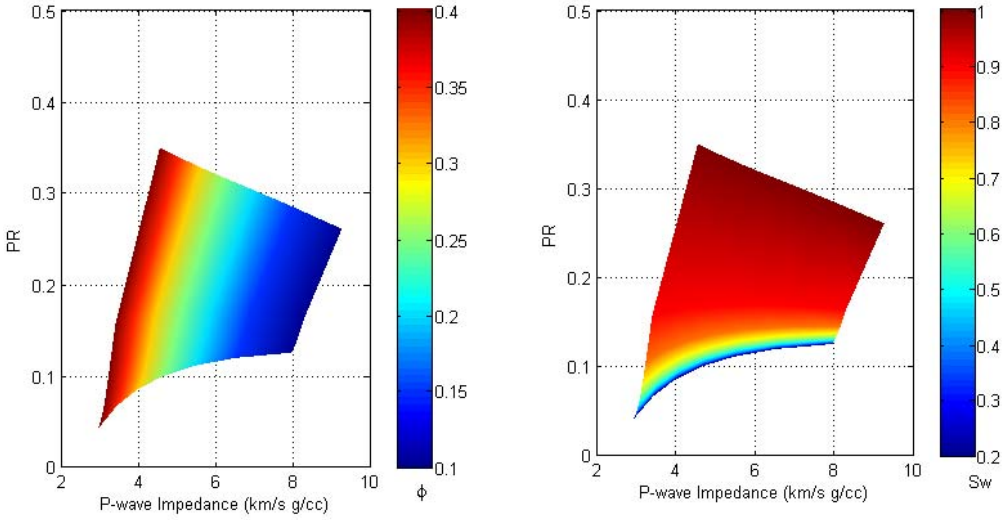

Figure 2.2: Poisson's ratio (PR) versus the acoustic or P-wave impedance for unconsolidated clean gas sand, color-coded by the total porosity (left) and water saturation (right), assuming pore pressure 30 MPa, temperature of 80°C, and gas gravity 0.65.

Using the same transforms, one among ϕ, S_w, and I_p and the other among ϕ, S_w, and $R \equiv R_t / R_w$, we create a P-wave impedance-resistivity mesh (Figure 2.4). The intersection of the two measurements is projected upon the saturation and porosity contours to yield (in this example) $\phi = 0.20$ and $S_w = 0.50$. Having both measurements helps constrain porosity and saturation, whereas each of the two measurements taken separately can yield only wide ranges of these variables.

In subsequent sections and chapters of this thesis, we will refer to this P-wave impedance-resistivity mesh as: a rock physics impedance-resistivity template. The term rock physics template (RPT) was first introduced by Ødegaard and Avseth

(2003). Avseth et al. (2005) define an RPT as a chart of locally constrained rock physics models for prediction of lithology and hydrocarbons. In general, these charts are acoustic impedance versus Vp/Vs ratio crossplots, which can be used for rock physics analysis. Avseth et al. (2005) also extends them to other seismic attributes, such as acoustic impedance versus shear impedance, or Lamé's parameter (λ) versus shear modulus (μ). The charts or templates, which we have created of P-wave impedance and resistivity, are also made of locally constrained models, and allow the prediction of porosity and saturation. Previous knowledge of lithology and pore fluid properties are required to create them; therefore, they can be used as a complement to Ødegaard and Avseth (2003)'s RPT.

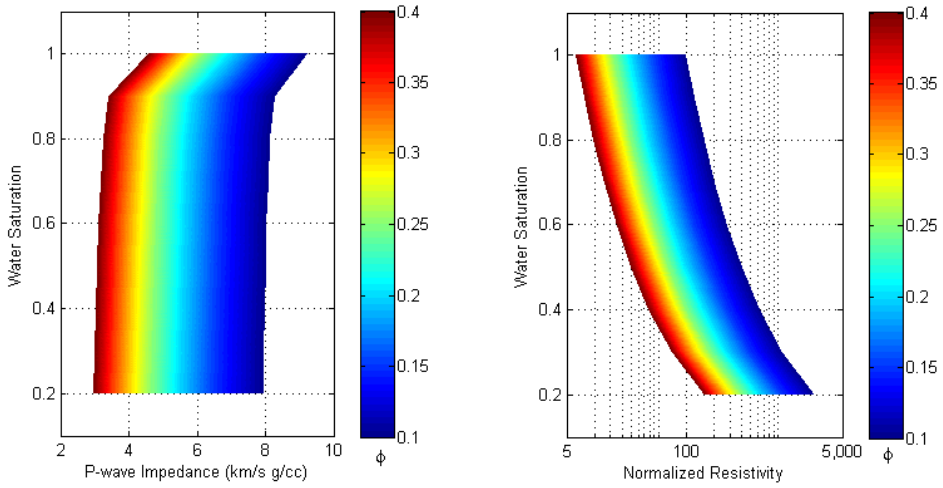

Figure 2.3: Water saturation versus the *P*-wave impedance (left) and versus the normalized resistivity (right), color-coded by the total porosity for the same unconsolidated clean gas sand as in Figure 2.2.

The power of this simple approach is its flexibility: there are many available rock-physics models of velocity-porosity and resistivity-porosity-saturation relations that can be used to produce site-specific templates that honor texture (e.g., cemented versus uncemented rock) as well as lithology. For example, in Figure 2.5 we display a template of I_p versus R, where the soft-sand model is replaced by the stiff-sand model (Gal et al., 1998), a case that is relevant for contact-cemented rock. As expected, the same impedance and resistivity inputs produce larger porosity and gas saturation than in Figure 2.4, simply because at the same porosity, cemented rock has a higher velocity than its uncemented counterpart. This result illuminates the importance of using the right model for the right rock. This model can be found using "rock-physics diagnostics" as discussed in, for example, Dvorkin et al. (2002 and 2004).

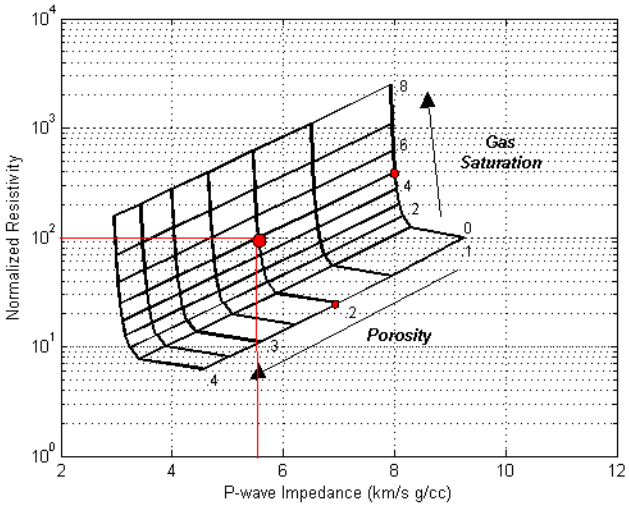

Figure 2.4: Normalized resistivity versus the P-wave impedance template for the same unconsolidated clean gas sand as in Figure 2.2. The large red circle is the intersection of the hypothetical resistivity and impedance data with small red circles showing its projections on the porosity and saturation contours.

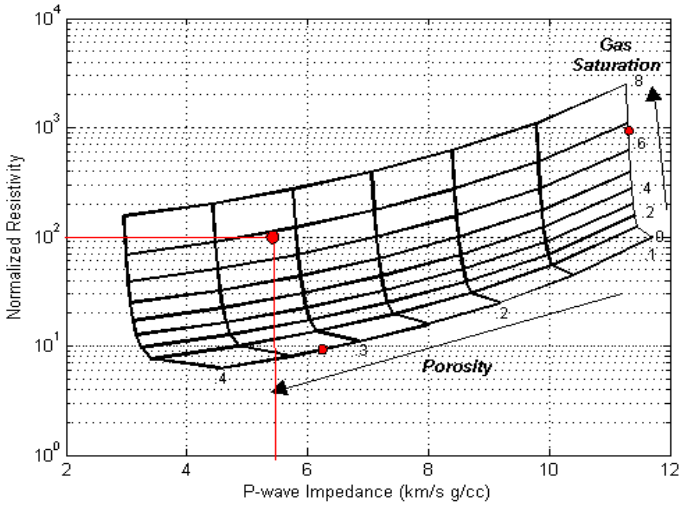

Figure 2.5: Same as Figure 2.4 but for cemented sandstone (using the stiff-sand model).

This flexibility accommodates not only the rock type but also the fluid, or more generally, the pore-filling material. To build a relevant I_p versus R template (Figure 2.6), we select the elastic and resistivity models describing a hydrate reservoir as established for the Mallik 2L-38 hydrate well (Canada) by Cordon et al. (2006). The log data superimposed upon this rock-physics mesh indicate that the porosity of the reservoir is about 0.3 with a hydrate saturation up to 0.8, which is consistent with the values directly observed in the well. A detailed treatment of this case is described in Chapter 8 of this thesis.

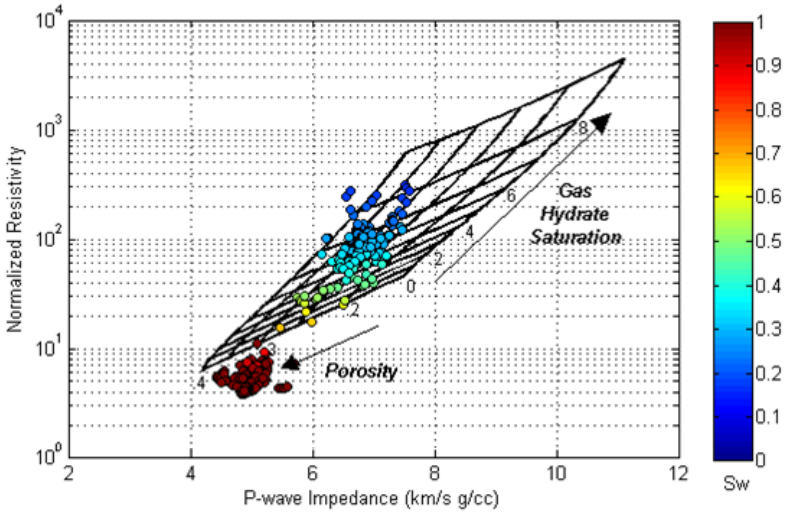

Figure 2.6: Same as Figure 2.4 but for a methane-hydrate reservoir. The well data (symbols) are color-coded by water saturation (one minus hydrate saturation). Dark blue indicates high amounts of hydrate. The red and brown symbols are for shale and thus fall outside of the mesh which is built for clean sand.

2.4 Effect of Reservoir Thickness: Wedge Modeling

As the thickness of the reservoir decreases, both the seismic and resistivity responses are affected. To study how these changes in the seismic and electric responses can affect our ability to predict porosity and saturation, we model four different scenarios.

In the following example we consider a blocky gas sandstone sandwiched between two shale half-spaces with identical properties. First, we assume that a soft sandstone wedge is surrounded by a soft shale, where elastic properties depend on porosity, which varies mainly as a function of sorting (Dvorkin and Nur, 1996). Second, we assume both sand and shale are contact-cemented rocks, using the stiff sand model (Gal et al., 1998). Third, we assume that a soft sandstone is embedded in a stiff shale,

and finally (fourth) a stiff sandstone embedded in a soft shale. All of these settings are geologically plausible.

For each scenario, we vary the shale porosity, $\phi(SH)$, from 0.5 down to 0.1 and the sand porosity, $\phi(SS)$, from 0.35 down to 0.2. The coordination number used to model both sand and shale is 6, the formation water resistivity is 0.1 ohm·m, and the critical porosity is 0.4. We also assume a clay content of 0.05 for the sand, and 0.8 for the shale. Archie's equation (Archie, 1942), assuming a=0.89, and m=n=2, is used for all models in this example, although in general, these empirical constants will depend on the particular reservoir.

We model a gas sandstone reservoir with thickness changing from 25 m down to 2 m. Upscaling is performed using a Backus average with a running window of 12.5 m for the P-wave impedance, and an arithmetic average (equivalent to combining layers as resistors in series) with a running window of 150 m for resistivity. The window for P-wave impedance corresponds to a quarter of the seismic wavelength assuming a frequency of 50 Hz and an average seismic velocity of 2500 m/s. While the window for the resistivity is around 10% of the burial depth, which is a rough estimate of the resolution expected for these data (Strack, 1992).

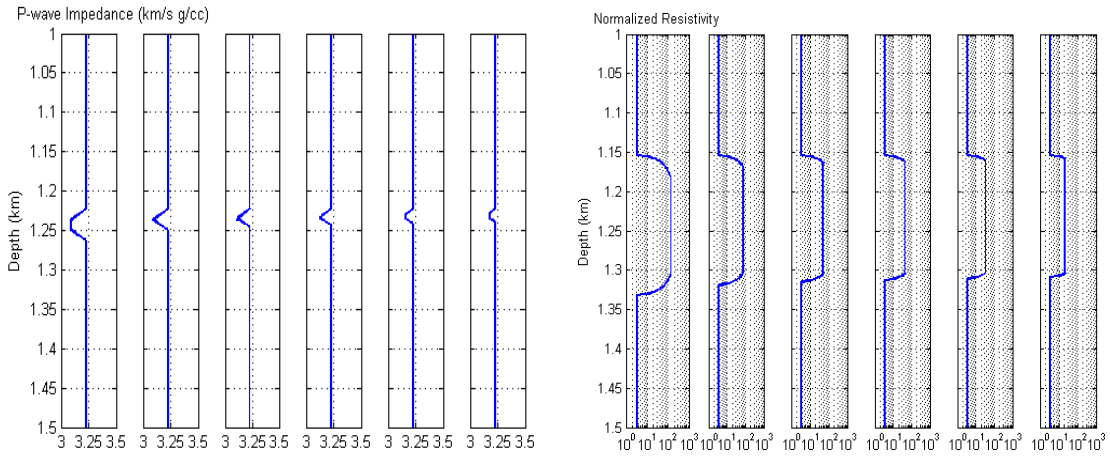

Figure 2.7: 90% gas-saturated sandstone of 35 % porosity and 5 % clay content embedded in a shale of 50 % porosity and 80% clay content. Left: P-wave impedance from soft sand model, upscaled using the Backus average. Right: Resistivity modeled using Archie's equation (a=0.89 and m=n=2), upscaled using the arithmetic average. Thickness of the gas sand from left to right in each panel is 25, 12, 8, 6, 4 and 2 meters.

One such realization is shown in Figure 2.7, for a shale with porosity 0.5 and sandstone with porosity 0.35 and gas saturation 0.9, using the soft-sand model to compute the elastic properties of both sand and shale. Resistivity and P-wave impedance are plotted versus depth for a variety of sand thicknesses. The top, leftmost panel of Figure 2.8 shows the normalized resistivity versus P-wave impedance in the middle of the gas interval for each of the thicknesses show in Figure 2.7. In this particular case, we observe that the upscaled P-wave impedance of the gas sand increases as its thickness drops, although not as dramatically as the normalized resistivity drops. The normalized upscaled resistivity changes from 100 to 20, while the upscaled P-wave impedance changes from 3.1 km/s g/cc to 3.2 km/s g/cc as the thickness decreases from 25 to 2 m.

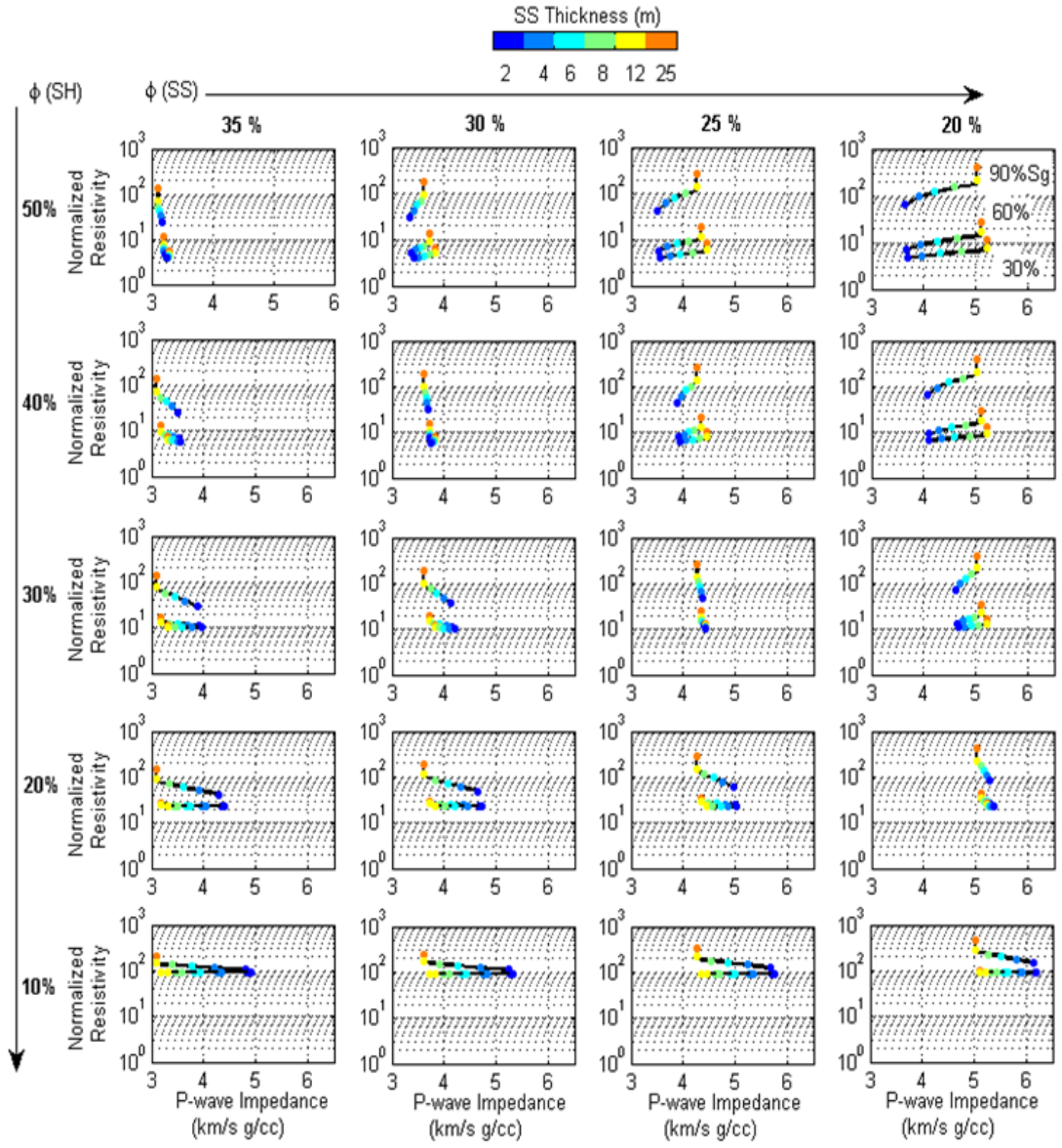

Figure 2.8: Varying porosity of the sand, from 0.35 to 0.20, along the columns and porosity of the surrounding shale, from 0.50 to 0.10, along the rows. The three different trends in each case are for gas saturation (Sg) 0.3, 0.6 and 0.9. Colors are the thickness of the sand in meters (see colorbar on top). P-wave impedance is modeled using the soft sand model for sand and shale with a coordination number 6 and a critical porosity 0.4. Resistivity is modeled using Archie's equation (a=0.89 and m=n=2). The data points shown are those of impedance and resistivity in the middle of the gas interval after upscaling using Backus average (12.5 m running window) and arithmetic average (150 m running window) for P-wave impedance and resistivity, respectively.

For high-porosity soft sand embedded in high-porosity soft shale (see the four upper panels of Figure 2.8 for sand porosity of 0.35 and 0.30 and shale porosity of 0.50 and 0.40, and also the case of a 0.25 porosity sand embedded in a 0.40, 0.30 or 0.20 porosity shale), the upscaled P-wave impedance has similar values for all thicknesses. Resistivity, on the other hand does reduce significantly as the thickness decreases, particularly for gas saturation 0.90, and there is poor separation between the resistivity values for saturations 0.60 and 0.30. This poor separation is mainly because EM data has lower resolution than seismic field data. As the background shale and sand resistivities become more similar, as in the case when the gas saturation is low, it becomes harder to discern the embedded sand. The same observation can be made when the porosity of the sand and shale are equal.

Another observation from this first model, using soft-sand equations, is that if the porosity contrast between the shale and the sand is strong, and as we decrease the thickness of the reservoir from 12 down to 2 meters, the upscaled P-wave impedance increases if the porosity of the shale is smaller than the porosity of the sand (up to 2 km/s g/cc in the case of shale porosity 0.1 and sand porosity 0.35), and decreases if the porosity of the shale is larger (up to 1.5 km/s g/cc in the case of shale porosity of 0.50 and sand porosity of 0.2). Also, if we have high-porosity sand (e.g., 0.35) surrounded by low-porosity shale (e.g., 0.1), it is harder to distinguish the gas sand, since after upscaling it will have the normalized resistivity closer to that of the background shale.

If we now keep the same sandstone modeled using the soft-sand model, but use the stiff-sand model to estimate the shale P-wave impedance (Figure 2.9), our results are

very similar to those obtained using the soft sand model for both sand and shale, except that there is a large contrast in the upscaled P-wave impedance (more than 2 km/s g/cc) as the thickness decreases when the contrast in porosity between sand and shale is the largest. (See the two extreme cases in the upper right corner and in the lower left corner of Figure 2.9, respectively.)

Next, we use the stiff-sand model for both sandstone and shale intervals (Figure 2.10). In this case, when the porosity of the shale is large compared to that of the sand, the upscaled P-wave impedance decreases as the thickness of the sand decreases (about 3 km/s g/cc for a shale with porosity 0.5 and a sand with porosity 0.2). However; when the shale has low porosity (which is more appropriate for the model used) with respect to the sand, as the thickness decreases, the upscaled P-wave impedance increases. This increase is around 2 km/s g/cc or less. Again, when the shale has low porosity, it is harder to discriminate between high and low gas saturation (e.g., 0.90 versus 0.30 gas saturation).

Figure 2.11 shows modeling assuming the same stiff-sand model for the reservoir, but replacing the stiff shale with soft shale. The resulting model is quite similar to using the stiff-sand model for both sand and shale, which confirms that the model choice for the shale is much less important than either the model choice for the sandstone or the porosity choice for the shale.

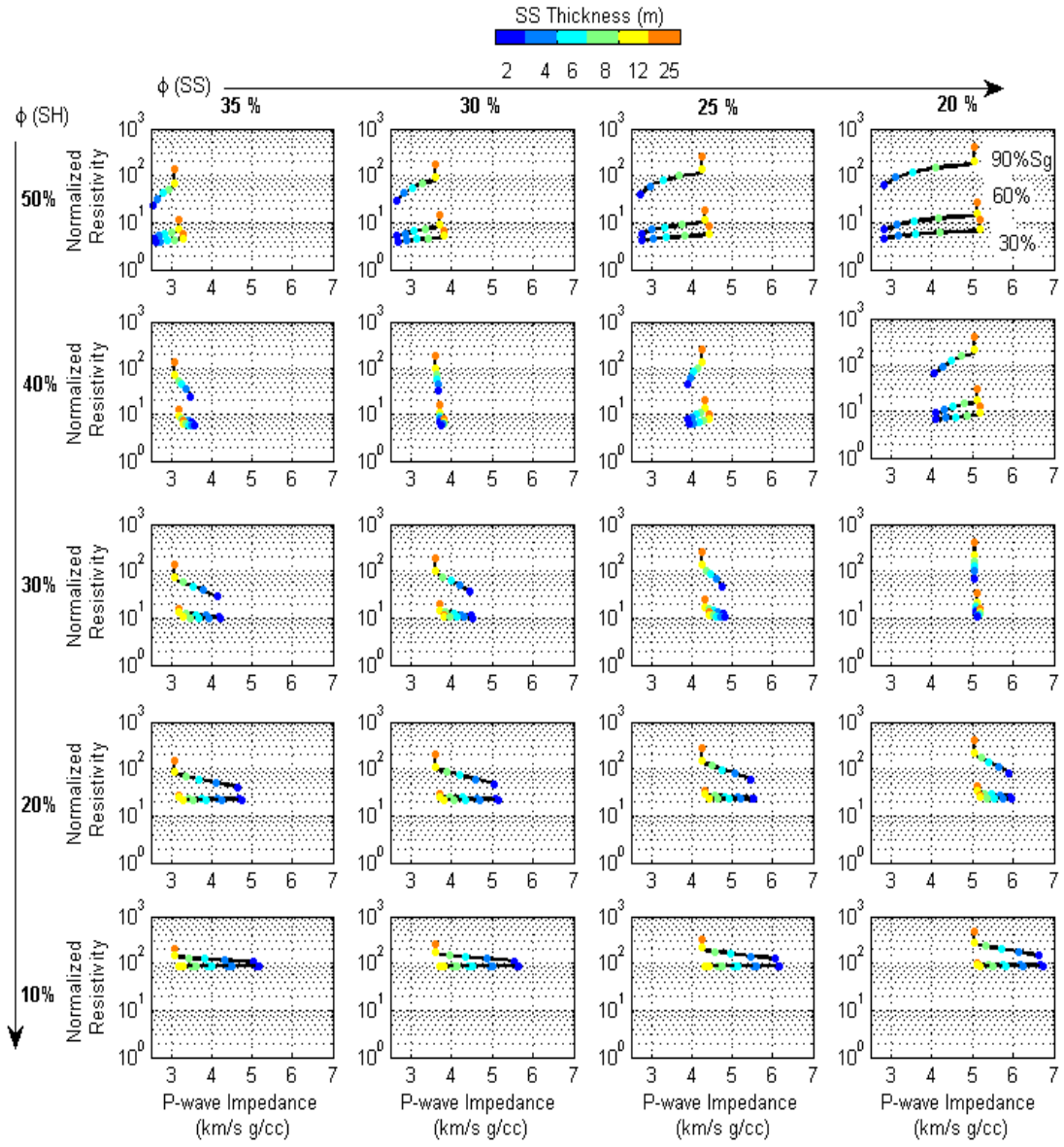

Figure 2.9: Same as Figure 2.8, but using the soft-sand model for the sandstone interval and the stiff-sand model for the surrounding shale.

We also used the Raymer-Hunt-Gardner relation (Raymer et al., 1980) to model the elastic properties of the sand and shale (Figure 2.12). In this case, our results were very similar to those we obtained using the stiff-sand model. In both cases, we observe

that discriminating gas saturation is highly dependent on the properties of both the sandstone and the surrounding shale.

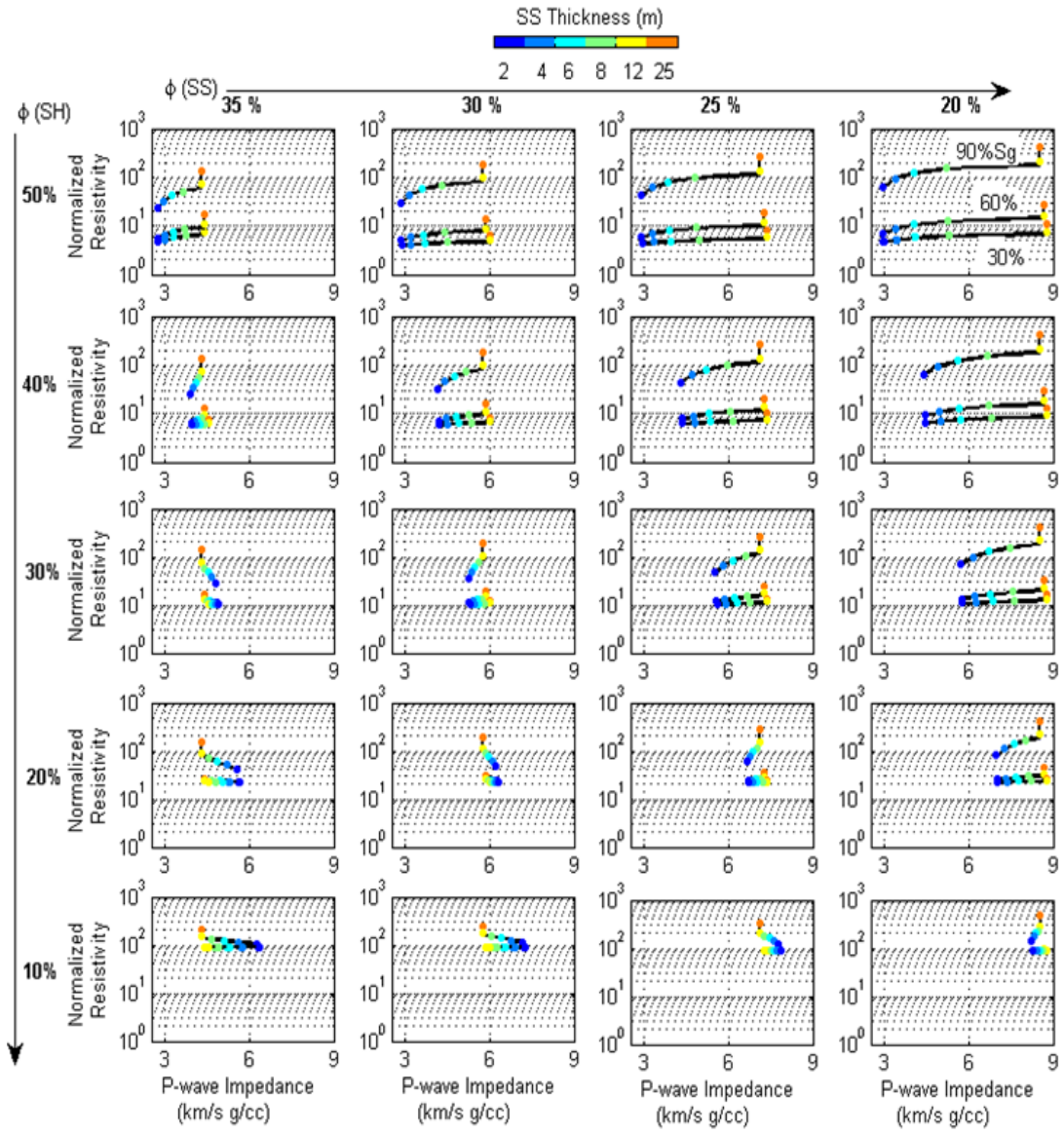

Figure 2.10: Same as Figure 2.8, but using the stiff-sand model to obtain the elastic properties of sand and shale.

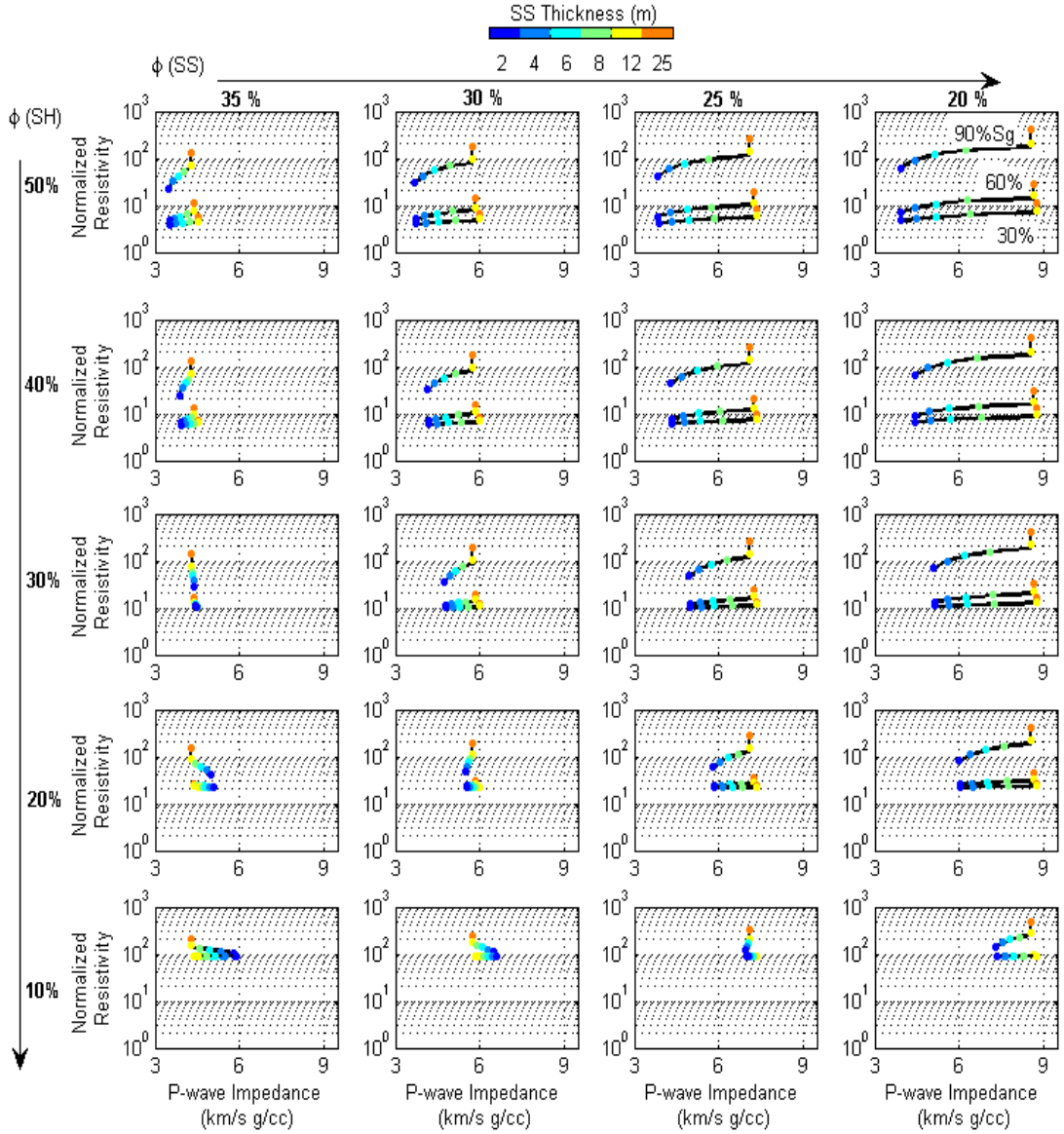

Figure 2.11: Same as Figure 2.8, but using the soft sand model to obtain the elastic properties of the surrounding shale, and the stiff sand model in the case of the sandstone interval.

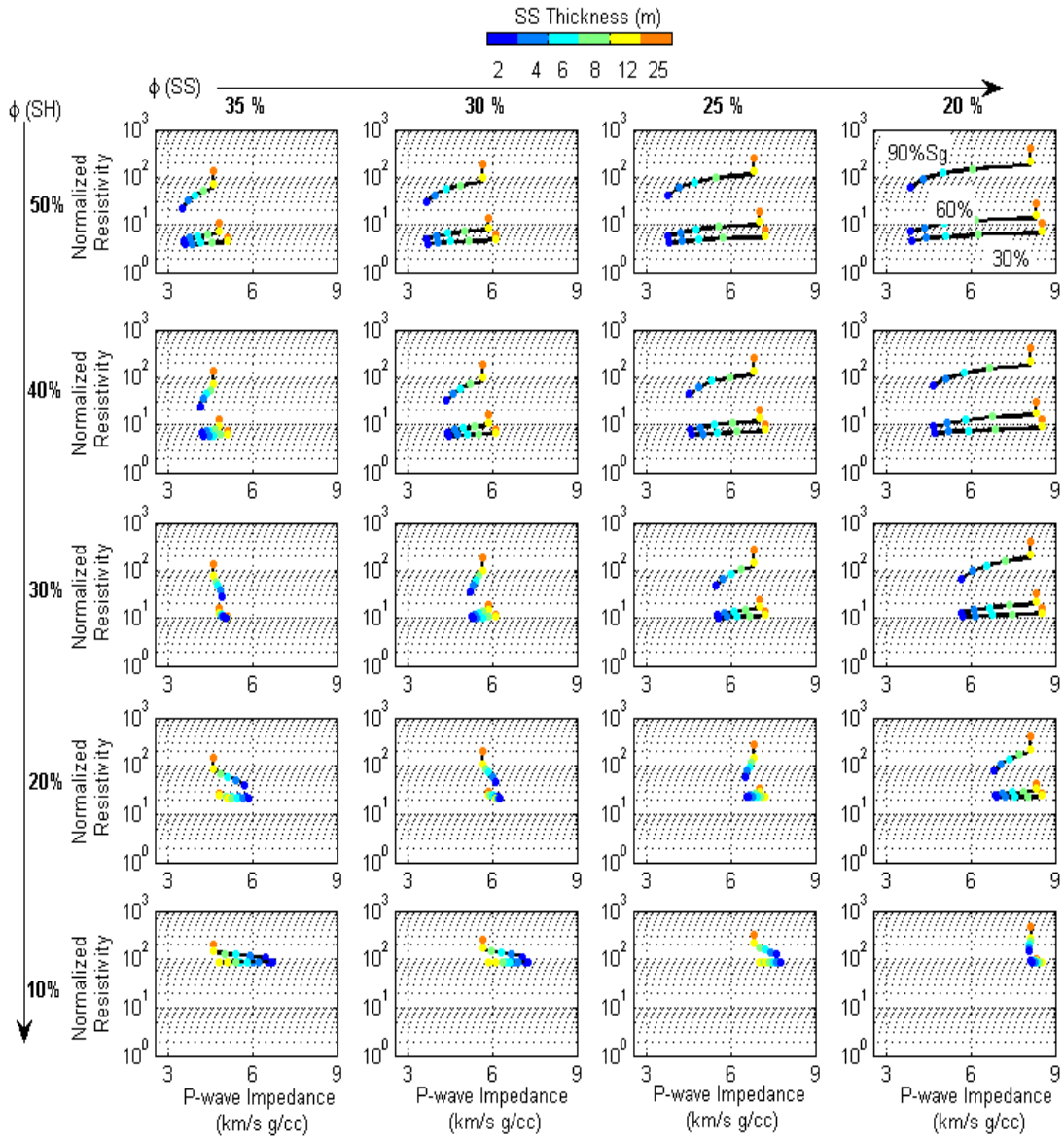

Figure 2.12: Same as Figure 2.8, but using the Raymer-Hunt-Gardner relation (Raymer et al., 1980) to model the elastic properties of both sandstone and shale.

Stiff sand may have a cementation exponent (m) larger than 2 in Archie's equation, since as sand becomes more cemented (stiff), the value of m tends to increase (Knight and Endres, 2005). Hence, we reproduce the same stiff-sand model for both sand and shale as before, but increasing the m exponent to 2.6 to observe

how this changes our modeling results (Figure 2.13). As we increase m, the normalized resistivity values are overall larger, but the shape of the curve, and the effect of the reservoir thickness is basically the same as with a lower m value.

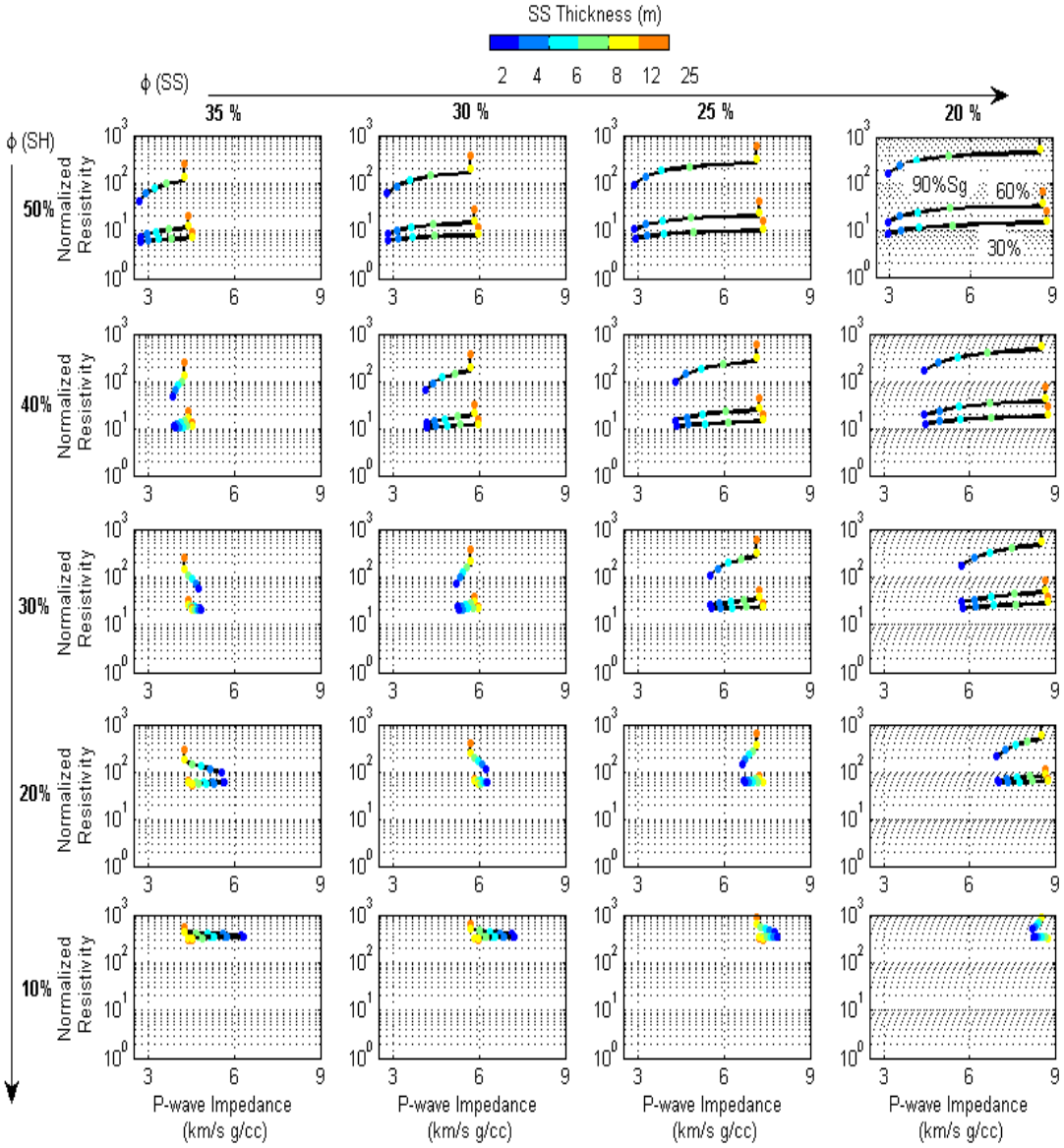

Figure 2.13: Same as Figure 2.10, but using cementation exponent (m) 2.6.

2.5 Discussion and conclusions

By combining two theoretical models, one that relates the elastic properties of rock to porosity, mineralogy and saturation, and the other that relates resistivity to porosity and saturation, we create templates of the normalized resistivity versus P-wave impedance. We can generate these templates at the well-log scale to obtain simultaneous estimates of porosity and saturation.

The answer is not unique. Many parameters can vary away from well control, including the geometry of the reservoir as well as the shale and reservoir properties. For an exhaustive interpretation, all parameters must be varied within reasonable ranges and probability distributions. This will eventually yield not a single answer but probabilistic distributions of porosity and saturation. We envision that the approach discussed here may produce useful invariants, such as porosity times saturation times thickness (or net-to-gross), which should be relied upon in reserve estimates. This is a subject of future work where the existing arsenal of stochastic modeling can be used within the framework presented here.

Finally, we must reiterate that the rock-physics models for the impedance-resistivity templates should be selected to reflect the geologic nature of rock in terms of both elastic behavior and resistivity (the latter, for example, by using the Waxman-Smits-Juhasz equation instead of Archie's law). In the same way as we upscale to analyze the effect of reservoir thickness, we can upscale the rock-physics templates. Upscaling the rock-physics templates will allow us to apply this quantitative interpretation approach to field data, as we will discuss in Chapter 6.

Chapter 3
Porosity, Permeability, Resistivity and Velocity Relations for Fontainebleau Sandstones

3.1 Abstract

The objective of this chapter is to experimentally revisit the relations among the resistivity, elastic-wave velocity, porosity, and permeability in Oligocene Fontainebleau sandstone samples from the Ile de France region, around Paris, France. We find that these samples follow a permeability-porosity relation given by Kozeny-Carman's equation with tortuosity 2.5 and percolation porosity 2%, for a mean grain size 250 microns.

In our resistivity measurements, we saturated the samples with brine (40,000 ppm NaCl salinity). All results reported below relate to 100% water saturation resistivity estimates, assuming a saturation exponent, n=2. In our subsequent effective-medium modeling we assigned very high resistivity to the mineral phase (10^{15} ohm m). We modeled resistivity as a function of porosity using the differential effective medium

(DEM) and self-consistent approximations (SC), as well as a semi-empirical model by Archie. Results show that when brine is modeled as the background and quartz grains as the inclusions, DEM underpredicts the measurements; therefore, it can be used as a lower bound. Using SC modeling with grain aspect ratio 1, and pore aspect ratio between 0.02 and 0.10, the experimental data fall into this theoretical range. The SC curve with the pore aspect ratio 0.05 appears to be close to the values measured in the entire porosity range. Archie's relation with the cementation exponent between 1.6 and 1.8 matches the data. We observe that as the porosity decreases, the cementation exponent required to match the data increases as well.

We also measured elastic-wave velocity on these dry samples for confining pressure between 0 and 40 MPa. We used a loading and unloading cycle and did not find any significant hysteresis in the velocity-pressure behavior. For the velocity data, using the self-consistent model with a grain aspect ratio 1 and pore aspect ratios 0.2, 0.1, and 0.05 fit our data at 40 MPa, while pores aspect ratios ranging between 0.1, 0.05, and 0.02 are a better fit for the data at 0 MPa. As expected, the stiff sand model and Raymer-Hunt-Gardner equation provide good predictions for the measured velocity at 40 MPa.

Our data exhibit an approximate linear trend between the P-wave velocity and the decimal logarithm of the normalized resistivity, with a large scatter at low porosity. This scatter correlates with the differences in measured permeability. The Faust (1953) equation appears to be an upper bound for our data (resistivity versus velocity) while a combination of the stiff sand model and the modified lower Hashin-Shtrikman

bound for resistivity serves as the lower bound. Also, a combination of the stiff sand model and Archie's resistivity equation with the cementation exponent between 1.6 and 2.1 covers the range of our data.

3.2 Introduction

Velocity and resistivity of rocks depend on porosity, texture, mineralogy, and pore fluid. Some of the earliest laboratory measurements showing the variation of the acoustic properties of rocks as functions of porosity, saturation, and pressure were by Wyllie et al. (1956, 1958). These studies showed that porosity undoubtedly is the primary factor affecting P- and S- wave velocities. Later studies (Nur and Simmons, 1969; Domenico, 1976; Mavko, 1980; Murphy, 1984) have refined our understanding of rock properties showing how pore type and pore fluid distribution (i.e., saturation heterogeneity) may contribute to variations in the P- and S- wave velocities. Pore geometry, in particular, affects pore stiffness which, in turn, influences the velocity sensitivity to pressure (Mavko, 1980; Mavko and Nur, 1978; O'Connell and Budiansky, 1974) as well as to saturation (Mavko and Mukerji, 1995).

Similarly, Archie (1942) was the first to show that the ratio of the conductivity of the pore fluid to the bulk conductivity of fully-saturated and clean sandstones corresponds to the formation factor, F, which is related to porosity through the following relation:

$$F = \frac{a}{\phi^m} \tag{3.1}$$

The *m* and *a* coefficients, known as the cementation exponent and tortuosity factor, are usually determined empirically. In Equation 3.1, *a* is close to 1, and was first introduced by Wyllie and Gregory (1953). The *a* coefficient may be considered a reservoir constant according to Worthington (1993), although originally Wyllie and Gregory (1953) considered it a function of porosity and formation factor of the original unconsolidated aggregate before cementation. When the dominant electrical conduction mechanism is ionic diffusion in the pore fluid, as in the case of clean well-sorted sands, *a* has to be one, because as porosity tends to one, the conductivity of the rock is equal to the conductivity of the fluid (Mavko et al., 1998). The coefficient *m* is also called the porosity exponent and different studies have related it to grain and pore shape (Jackson et al., 1978; Ransom, 1984). According to Knight and Endres (2005), *m* depends on the geometry of the system or the connectedness of the pore space, and it is called the cementation factor because of the importance of cementation in determining microgeometry. The *m* coefficient is close to 2 in sandstones, but it can be as high as 5 in carbonate rocks (Mavko et al., 1998). The dependency of the *a* and *m* coefficients on rock properties has been the subject of multiple studies (see Worthington, 1993 for a review). Such studies report a large number of factors affecting those constants, including porosity, type of porosity, tortuosity, pore geometry, degree of cementation, sorting, grain shape, packing of grains, pressure and wettability. Schön (1996) reports that both parameters, *a* and *m*, are controlled by pore channel geometry, including pore shape and connectivity.

In this study, we measure porosity, permeability, resistivity and velocity in Fontainebleau sandstones. We first examine the permeability – porosity relation, and compare it to the Kozeny-Carman (Carman, 1961) relation, and a previous study by Bourbie and Zinszner (1985). We then analyze how porosity and permeability relate to resistivity using effective medium models, such as differential effective medium (DEM) (Bruggeman, 1935; Berryman, 1995) and self consistent (SC) (Landauer, 1952; Berryman, 1995), and a semi-empirical model by Archie (1942). We follow a similar procedure for P-wave and S-wave velocities as a function of porosity, using effective medium models, including also DEM and SC, and semi-empirical models, including the stiff sand model (Gal et al., 1998), the Raymer-Hunt-Gardner relation (Raymer et al., 1980), and Wyllie's time-average equation (Wyllie et al., 1958).

Elastic and electrical methods can contribute in different ways to characterizing rock. Each of them has limitations that can be overcome by integration with the other. The literature shows that laboratory studies performing joint measurements and analysis of velocities and resistivity of sedimentary rocks are quite scarce (i.e., Polack and Rapoport, 1956, 1961; Parkhomenko, 1967; Knight, 1991; Carrara et al., 1999. All these studies only use P-wave velocity and resistivity). In particular, there are no laboratory studies that use P-, S-wave velocities and resistivity together to better estimate porosity and permeability of reservoir rocks. Therefore, we examine the relation between resistivity and velocity, and how these two properties relate to porosity and permeability.

3.3 Method

The set of core plugs in this study comprises 23 Oligocene Fontainebleau sandstones, collected at outcrops in the Ile de France region, around Paris, France. The core plugs have a diameter around 2.5 cm, and a length ranging between 2.3 and 3.9 cm. Resistivity was measured at 1 kHz at benchtop conditions using the 4-electrode method, with the benchtop set-up that is part of the Core Lab's Advanced Resistivity System Model 300. The instrumental error for the measured resistivities is +/- 10 %.

Core plugs were saturated with a 40,000 ppm NaCl solution. Their water resistivity was monitored for a 48-hour period before the saturated rock resistivity measurements were performed, in order to reach a chemical equilibrium between the rock and the fluid. The resistivity of water was monitored before performing each measurement. The temperature of the water was 21±1 degrees Celsius, and its resistivity 0.17 ± 0.01 ohm m. One-hundred percent water saturation was not reached for these samples, particularly the low porosity ones, with an average saturation of 80%, latter determined by weighting the samples. Archie's equation was used to estimate the resistivities at full saturation (R_0) from the measured resistivity (R_t) at saturation S_W assuming a saturation exponent (n) of 2, as it follows:

$$R_0 = R_t S_W^{\,n} \tag{3.2}$$

For 9 of the 23 core plugs, measurements of P- and S-wave velocity were also performed under variable confining pressure, at one atmosphere pore pressure. Confining pressure was increased to 40 MPa, with 5 MPa increments. The plugs were jacketed with rubber tubing to isolate them from the confining pressure medium. The

pulse transmission technique was used to measure P-wave velocity at 1 MHz frequency and S-wave velocity at 0.7 MHz. The error for the velocity measurements is around +/- 1%. Three linear potentiometers were used to measure length changes of the samples as a function of stress. These length changes were related to changes in porosity by assuming that pore contraction was the main cause of strain (i.e., we assume that the mineral was incompressible).

Helium porosity, Klinkenberg-corrected nitrogen permeability, length, diameter and weight of all these plugs were also measured. Helium porosity and total porosity estimated from volume and weight are essentially the same, as we can observe from Figure 3.1. Mineralogy of these samples is 100% quartz, with an average grain size of 250 micrometers (Bourbie and Zinszner, 1985) (see also CT scan sections in Figure 3.2). All the measurements are included at the end of this chapter in Tables 3.2 through 3.5.

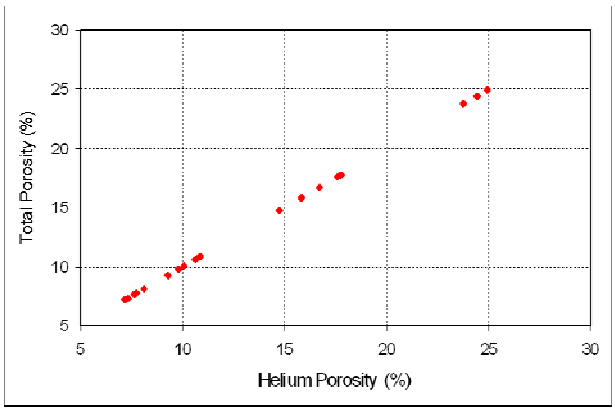

Figure 3.1: Total porosity estimated from volume and mass versus porosity measured using Helium porosimeter.

3.4 Permeability versus Porosity Measurements and Modeling

The core plugs measured for this analysis were compared to core plugs from the same region studied by Bourbie and Zinszner (1985), and Doyen (1988). We find that they follow a similar permeability versus porosity trend (Figure 3.3). If we compare this permeability-porosity trend with that given by Kozeny-Carman's relation, we observe that with tortuosity 2.5, percolation porosity 2%, and grain size 250 μm, the fit is satisfactory (Figure 3.4). The grain size that we use in this fit agrees with observations by Bourbie and Zinszner (1985), who found that these samples were composed of sub-spherical quartz grains (more than 99.8% quartz) with diameter around 250 microns.

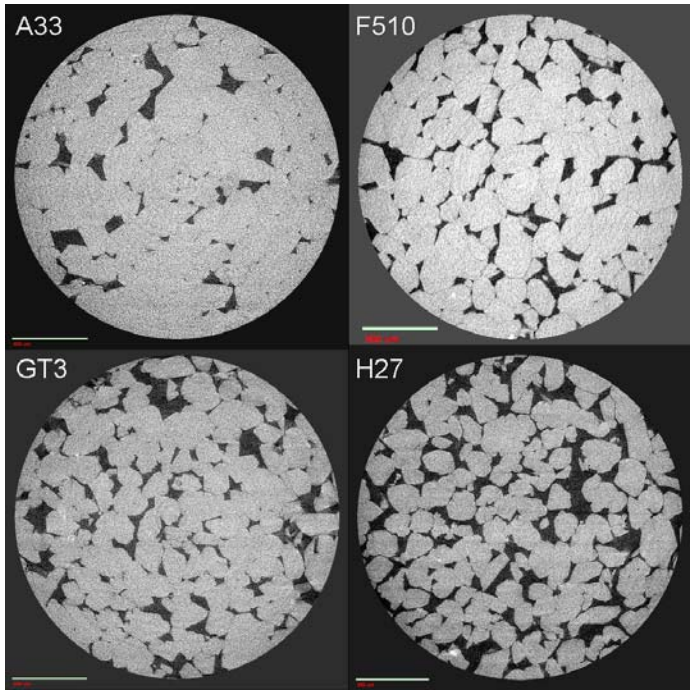

Figure 3.2: CT scans for Fontainebleau samples: A33, F510, GT3 and H27. The scale given as a green line in the bottom left corner is 500 μm. These plugs have the following porosity and permeability: 7% and 12.5mD for A33, 15% and 592mD for F510, 16.7% and 704mD for GT3, and 25% and 3630mD for H27.

The Kozeny-Carman's relation that we are applying here was published by Mavko and Nur (1997) and introduced the percolation porosity (ϕ_P):

$$\frac{k}{d^2} = \frac{1}{72}\frac{(\phi - \phi_P)^3}{[1-(\phi-\phi_P)]^2\tau^2}, \tag{3.3}$$

where k is permeability, d is the grain diameter, τ is tortuosity and ϕ is porosity. Percolation porosity corresponds to that below which the remaining porosity is disconnected and does not contribute to flow, and generally it is of the order of 1 to 3 % (Mavko et al., 2009).

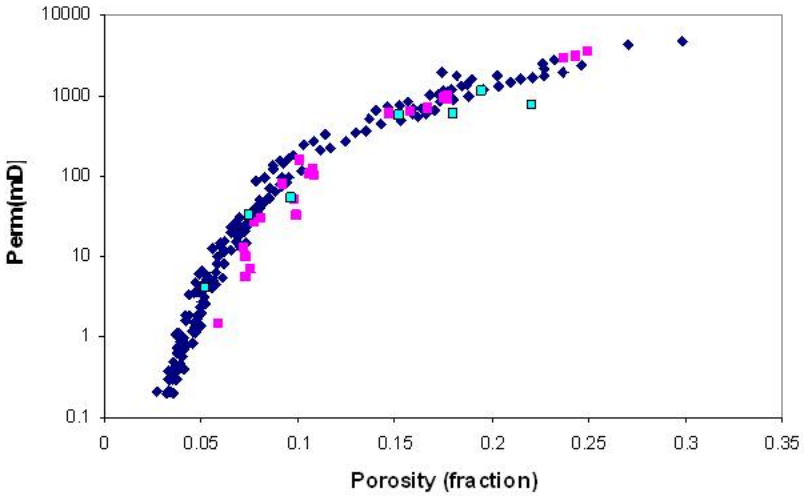

Figure 3.3: Permeability versus porosity for samples from Bourbie and Zinszner (1985) in blue, Doyen (1988) in cyan, and this study in magenta.

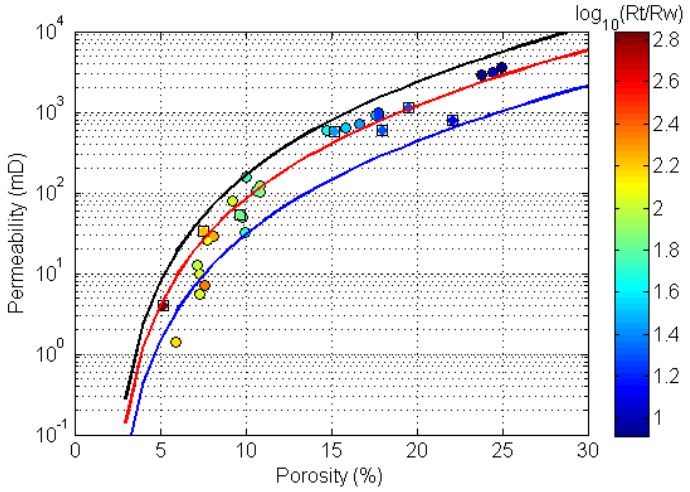

Figure 3.4: Permeability versus porosity for samples of this study as circles, and those from Doyen (1988) as squares with circles inside, colorcoded by log10(Rt/Rw). Kozeny-Carman modeling curves for tortuosity 2.5 and percolation porosity 2% are plotted for grain sizes 350, 250, and 150 μm (from black to blue).

As Bourbie and Zinszner (1985) pointed out, two different permeability-porosity linear trends in the log-log scale can be defined, one for the high porosity, and one for the low porosity samples (Figure 3.5). For the high porosity samples, the porosity exponent is around 3, as expected from the Kozeny-Carman's relation. However, as porosity decreases, the exponent is larger, in our case close to 5. This is due to the fact that at lower porosities, some of the pore fraction is not contributing to the permeability, which is the amount of porosity lower than the percolation porosity. If the logarithm of permeability is plotted versus that of the difference between total porosity and percolation porosity, a single linear trend can be identified which is given by $k = 0.0241(\phi - \phi_P)^{3.792}$ (Figure 3.5). In this equation, the porosity is not input as a fraction but as a percentage.

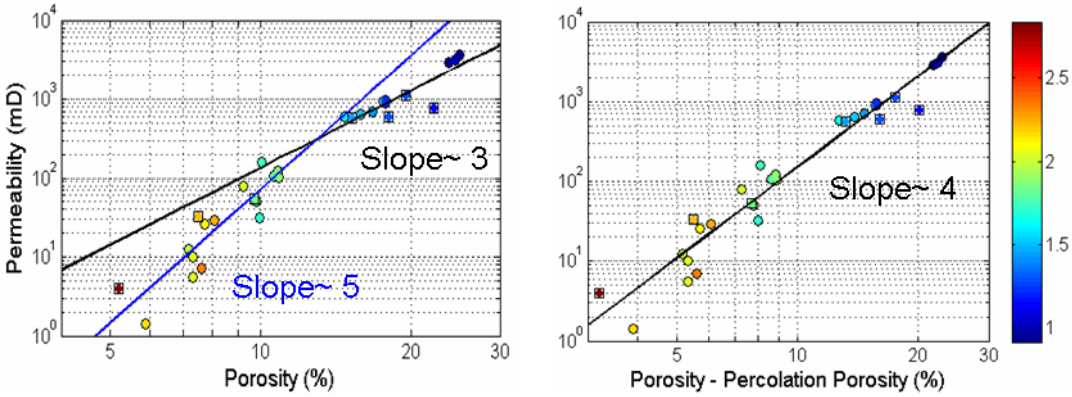

Figure 3.5: Permeability versus porosity on the left, and porosity minus percolation porosity in log-log scale for samples of this study as circles, and those from Doyen (1988) as squares, colorcoded by log10(Rt/Rw). Two linear trends can be identified on the left, one for the low porosity samples in blue (slope~5), and one for the high-porosity samples in black (slope~3). On the right a single trend can be identified.

3.5 Resistivity relation with salinity of the saturating fluid, porosity and permeability

To test our set-up, we measure the resistivity on 4 of the samples with brine of salinities 11,000; 40,000; and 100,000 NaCl ppm. We applied Equation (3.2) to compute the conductivities at full water saturation. Plotting this rock conductivity at S_w =1 versus the conductivity of the saturating water (Figure 3.6), we can fit lines that cross the origin for each of the four samples. This behavior is what we expect in clean sandstones where no clay is present (Waxman and Smits, 1968; Waxman and Thomas, 1974; Thomas, 2007). In general, at around 20,000 NaCl ppm water salinity, we would expect that the data would deviate from this line, but our measurement at 11,000 ppm still fits lines that cross the origin for the four samples, which is the

behavior that is expected in clean sandstones (Waxman and Smits, 1968; Waxman and Thomas, 1974; Thomas, 2007).

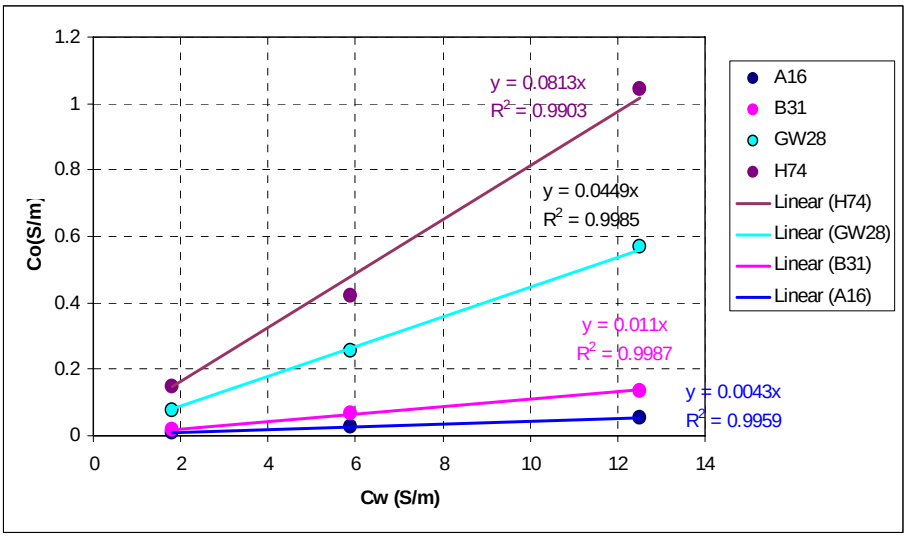

Figure 3.6: Conductivity measured for the core at 100% saturation versus water conductivity for 4 different samples measured at 3 different salinities:10,000; 40,000 and 100,000 NaCl ppm. Linear fits crossing the origin are also shown.

It is important to point out that the absence of clay minerals does not prevent surface conduction from occurring. Surface conduction can occur even in the case of the presence of only quartz, and no clay minerals. Revil and Glover (1997) show that surface conduction can be significant in a quartz matrix if water conductivity is below 0.01 S/m. However, this measurement condition does not apply to our case.

In our experiments measuring resistivity of 23 core plugs, we used 40,000 NaCl ppm salinity brine at 21 °C. Therefore under this salinity and temperature conditions, the effects due to surface conduction are negligible compared to ionic conduction (Waxman and Smits, 1968; Waxman and Thomas, 1974). The resistivity at S_W =1 was

estimated from measured resistivity using Equation (3.2). All results reported below relate to these 100% water saturation resistivity estimates.

Plotting resistivity versus porosity, we find that the measurements fall between the lower and the modified upper Hashin-Shtrikman bounds (Wempe, 2000), assuming a quartz matrix with resistivity of 10^{15} ohm m, critical porosity 0.4, and percolation porosity 0.02 (blue and red curves in Figure 3.7). If we compare our measurements to the differential effective medium model for grains of quartz suspended in water, we find that this model underpredicts the measurements (magenta curve in Figure 3.7). At the same time, the self-consistent effective medium modeling does fit the data (Figure 3.8), in particular if we use ellipsoidal inclusions with aspect ratios between 0.02 and 0.1.

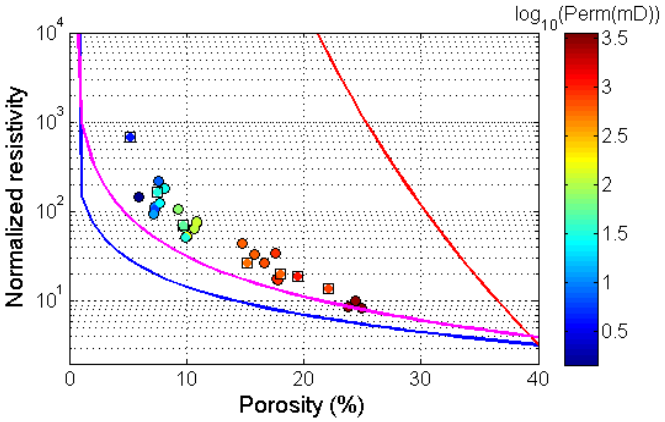

Figure 3.7: Lower and modified upper HS bounds (blue and red curves), and DEM modeling for inclusions with aspect ratio of 1 in a background of water (magenta curve). Circles are data from this study, and squares are data from Doyen (1988). The data are colorcoded by the decimal logarithm of the permeability in mD.

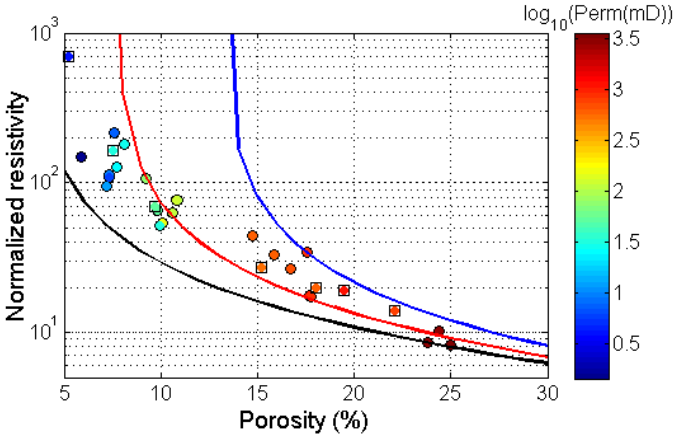

Figure 3.8: Self-consistent modeling for grain aspect ratio of 1, and pore aspect ratio of 0.1 in blue, 0.05 in red, and 0.02 in black. Circles are data from this study, and squares are data from Doyen (1988). The data are colorcoded by the decimal logarithm of the permeability in mD.

Archie's equation with cementation exponents (*m*) between 1.6 and 2.1 matches these data well (Figure 3.9). These *m* values are the typical values used for clean sandstones, and agree with previous studies in Fontainebleau sandstones, such as that by Durand (2003) that gives values between 1.54 and 1.75. Knackstedt et al. (2007) estimate *m* from numerical experiments and also compute it for measurements by Jacquin (1964) and Doyen (1988) and obtain values between 1.5 and 2.25. Hausenblas (1995) also obtains cementation exponent between 1.7 and 1.8 for four Fontainebleau samples with porosities between 6.2 and 7.5%.

We observed that the cementation exponent changes as porosity changes; therefore, we can summarize our results in a table (Table 3.1) where we report the cementation exponents that best fit the data for each porosity range.

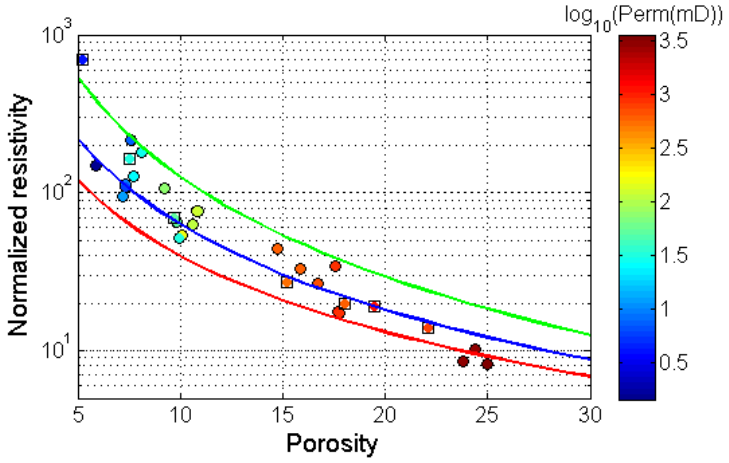

Figure 3.9: Archie's modeling for a=1, and cementation exponent of 1.6 in red, 1.8 in blue and 2.1 in green. The data are colorcoded by the decimal logarithm of permeability in mD.

Porosity (%)	*m*
5 to 7	1.8 - 2.1
9 to 22	1.8
23 to 25	1.6

Table 3.1: Porosity or cementation exponent that best match the data for given ranges of porosity.

Raiga-Clemenceau (1977) gave a relation between permeability and the cementation exponent:

$$m = 1.28 + \frac{2}{\log k + 2}, \tag{3.4}$$

where k is permeability in mD. If we use this relation, we find cementation exponents between 1.64 and 2.21 (Figure 3.10), which are similar to the values discussed above.

The cementation exponent seems to show some dependence on porosity, tending to be higher as porosity decreases. Olsen et al. (2008) give an empirical relation to derive the cementation exponent from porosity, permeability and specific

surface area. This relation is between cementation exponent (m) and specific surface area (S) laboratory data:

$$m = 0.09 \ln S + 1.98 . \tag{3.5}$$

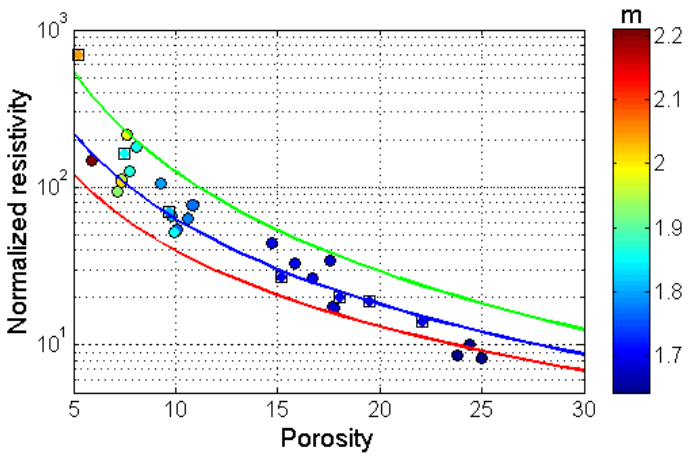

Figure 3.10: Archie's modeling for a=1, and cementation exponent of 1.6 in red, 1.8 in blue and 2.1 in green. Data points are colorcoded by the cementation exponent (m) estimated from Equation (3.4).

The cementation exponent in Equation (3.5) was derived from Archie's equation assuming a = 1, and resistivity and porosity measurements at fixed water resistivity. Specific surface area was measured using the nitrogen adsorption method (Brunauer et al., 1938). It is then expressed in terms of porosity (ϕ), permeability (k) and a constant c, using Kozeny's equation:

$$k = c\frac{\phi^3}{S^2}, \tag{3.6}$$

Using Equations (3.6) and (3.5), we obtain the final relation that Olsen et al. (2008) use to estimate the cementation exponent from porosity and permeability:

$$m = 0.09 \ln\left(\sqrt{\frac{c\phi^3}{k}}\right) + 1.98 . \tag{3.7}$$

The constant c is, according to Olsen et al. (2008), close to 0.25, but depends on porosity. From Equation (3.6) and one of the common forms of Kozeny-Carman, this constant can be expressed in terms of tortuosity as:

$$c = \frac{1}{2\tau^2}. \tag{3.8}$$

If the tortuosity is 1.41, c is 0.25, but if the tortuosity is 2.5, as we assumed for our previous Kozeny-Carman modeling, the constant c is 0.08. If we estimate the cementation exponent assuming c = 0.25 and c = 0.08, we obtain m 1.6 and 1.8, respectively, which is close to the values we had found match the data (Figure 3.11). Hence, we have observed that changing c does not greatly affect the estimate of m, and this semi-empirical formula (Equation 3.7) gives a good estimate for cementation exponent to be used in Archie's equation.

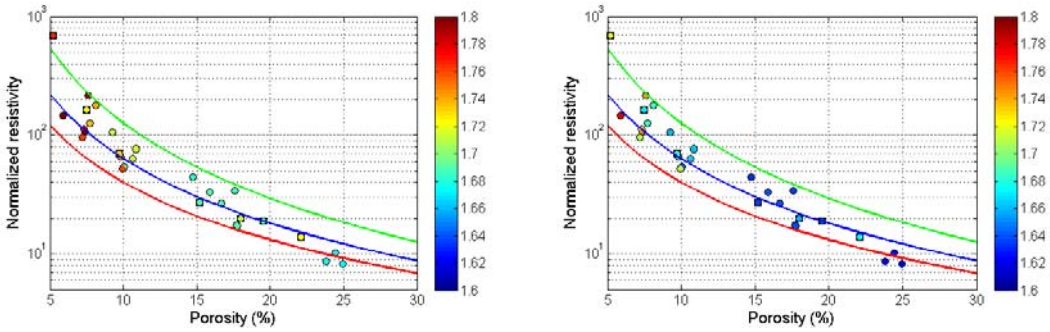

Figure 3.11: Archie's modeling for a = 1, and cementation exponent 1.6 in red, 1.8 in blue, and 2.1 in green. Circles are data from this study, and squares are data from Doyen (1988). The data are colorcoded by the cementation exponent estimated from Equation 3.7 with c = 0.25 on the left and c = 0.08 on the right.

Estimating permeability from resistivity has been a problem examined by different authors, including Archie (1942), who shows an average trend of formation factor versus permeability for sandstones, but recognizes that the scatter is too large to establish a definite relation between the two properties. Worthington (1997) revisits this study by Archie and shows how formation factor (normalized resistivity) F decreases as permeability increases according to the following relation:

$$k = \left(\frac{b}{F}\right)^{1/c}. \tag{3.9}$$

where b and c are positive empirical constants.

Worthington (1997) argues that as water salinity decreases, or grain size decreases, or the clay content increases, the relation between resistivity and permeability changes and resistivity actually increases as permeability increases in the following form:

$$k = gF^{h}. \tag{3.10}$$

where g and h are positive empirical constants.

Some other relations derived between formation factor and permeability incorporate other parameters, such as the characteristic length of the pore space (Katz and Thompson, 1986; Johnson et al., 1986), the porosity, the specific surface area and the cementation exponent (Schwartz et al., 1989)

If we plot our measured formation factor versus permeability, we find significant scatter, particularly at high resistivity. Still, a trend between these two variables in the form of Equation 3.9 can be defined as follows:

$$k = \left(\frac{702.01}{F} \right)^{1/0.54} . \qquad (3.11)$$

The R^2 for this trend is 0.92, but the norm of the residuals is 132 mD (due to large data scatter at low porosity), hence, it is not very precise and has to be used with caution (Figure 3.12).

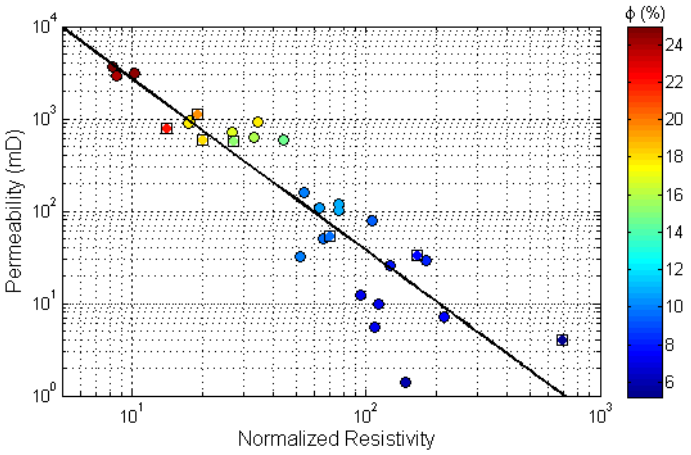

Figure 3.12: Permeability versus normalized resistivity colorcoded by porosity for same samples as those in Figure 3.10. The solid black line corresponds to Equation 3.11.

3.6 Velocity, confining pressure, porosity, and permeability

P- and S-wave velocities were measured as functions of confining pressure for 9 samples as shown in Figure 3.13 (P wave in blue and S wave in red). Porosities of the plugs ranged from 0.06 to 0.25. Filled circles in Figure 3.13 represent measurements as we were increasing confining pressure, and open circles are the measurements taken as pressure was decreasing.

These samples do not show velocity hysteresis as we load and unload them, except for sample A11. In the case of A11, the velocities have almost the same values at zero

pressure for loading and unloading, which means that we possibly did not wait long enough when we took the measurement at 5 MPa for equilibrium to be reached.

Poisson's ratio for these sandstones is between 0.02 and 0.16 (Figure 3.14), which is close to the values expected for dry sandstones, according to Mavko et al. (1998).

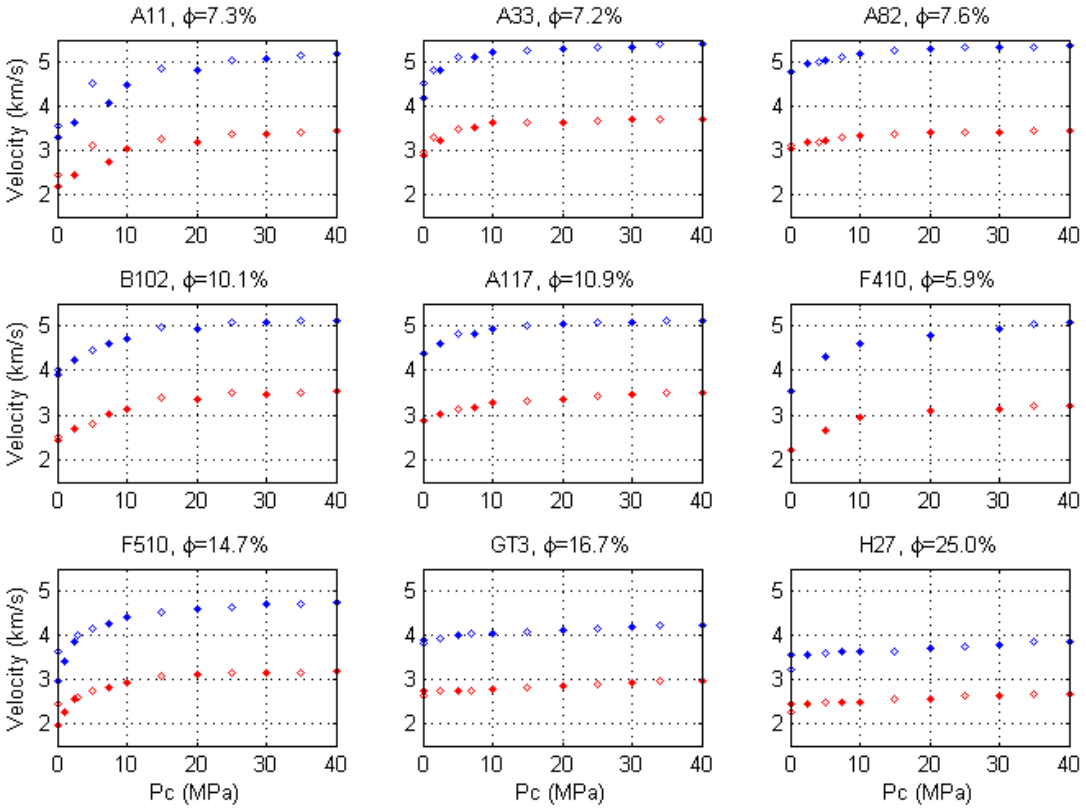

Figure 3.13: P-wave (in blue) and S-wave (in red) velocity (km/s) as a function of confining pressure for 8 different coreplugs of Fontainebleau sandstone.

Samples A11, A33 and A82 have similar porosity, close to 7%, but their permeabilities are 9.98, 12.45 and 7.08 mD, and formation factors 113, 95, and 216, respectively. We observe here a correlation between resistivity and permeability for these three samples, the smaller the permeability the larger the resistivity.

Core plugs A11 and A33 show larger dependence of the velocities on pressure than core plug A82, which has the lowest permeability and largest formation factor of the three. This conforms with the fact that A82 is the least compliant of the three samples.

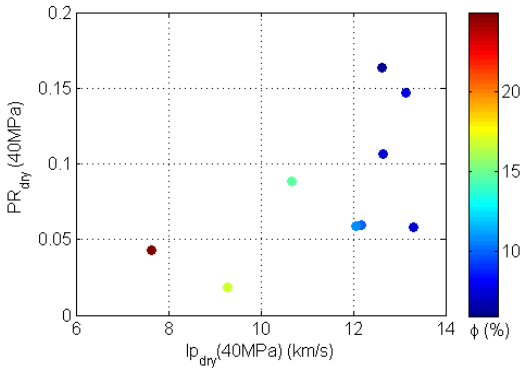

Figure 3.14: Poisson's ratio (PR) versus P-wave impedance measured at 40 MPa confining pressure colorcoded by porosity for the same 9 Fontainebleau core plugs shown in Figure 3.13.

CT scans for these three samples (Figure 3.15) show that A82 have relatively small macropores, on the order of 100 microns or less, while A11 and A33 have larger macropores, up to 200 microns. This difference in macroporosity may be responsible for the measured larger permeability and lower resistivity in A11 and A33.

We performed mercury intrusion porosimetry in small drilling fragments (mass =1-1.5 g) of samples A11, A33 and A82, in order to study the distribution of pore access diameters. This technique measures the volume of mercury that penetrates a sample as a function of pressure (Aligizaki, 2006). Results are generally reported using cumulative intrusion curves and differential pore size distribution plots. Cumulative intrusion curves are plots of the cumulative volume of mercury intruded in the sample versus the pore throat or pore access diameter. The differential pore size

distribution is the differential of the volume of mercury intruded in the sample versus the pore access diameter. A contact angle between sandstone and mercury of 140 degrees was used for our calculations (Metz and Knofel, 1992; Spearing and Matthews, 1991; Milsch et al., 2008).

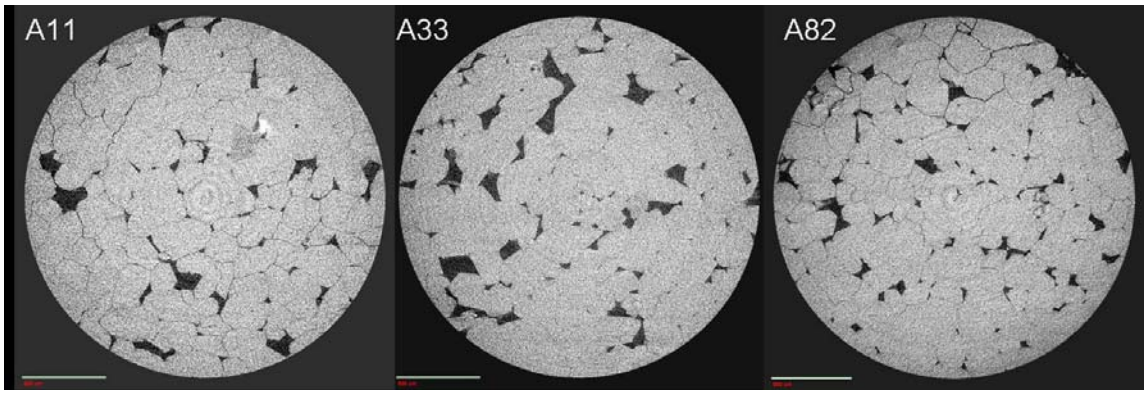

Figure 3.15: CT scans for three Fontainebleau core plugs: A11, A33 and A82, all with similar porosity, around 7%. The scale, given as a green line in the bottom left corner, is 500 μm.

Porosity estimates obtained from mercury porosimetry are 8.68% for A11, 7.18% for A33, and 8.77% for A82. Helium porosity measured for the corresponding core plugs were: 7.33% for A11, 7.18% for A33, and 7.61% for A82. The cumulative intrusion curves (shown in red in Figure 3.16) reveal that samples with the largest porosity, A82 and A11, also have the largest number of pore throats with diameter larger than 10 μm. The average pore diameters are 7.0 μm for A11, 3.8 μm for A33 and 3.2 μm for A82. The median pore diameters are 13.0 μm for A11, 8.8 μm for A33 and 9.4 μm for A82. These pore throat distributions are similar as far their mean and median, but they are multimodal (see differential pore size distributions in blue in Figure 3.16). Comparing the differential pore size distributions, samples A11 and A33

show narrower distributions of pore throat sizes than sample A82. Sample A82 has a large amount of pore throats with diameters less than 0.1 μm, shown as several peaks in the differential pore size distribution, while A11 and A33 only show pore throats with diameters larger than 0.1 μm, correlating with the fact that A82 is the least permeable of the three samples.

We also obtained estimates of total pore area for these samples, which were very similar for A11 and A33: 0.025 m^2/g, and 0.031 m^2/g, respectively. Sample A82, had 0.046 m^2/g total pore area. If we compute the specific surface area multiplying by the grain density 2.65 g/cc, we obtain 0.066×10^6, 0.122×10^6 and 0.082×10^6 1/m for A11, A33 and A82. A specific surface area can be computed from the median pore radius (r) as $2/r$ (Milsch et al., 2008), and we obtain: 0.31×10^6, 0.46×10^6 and 0.43×10^6 1/m for A11, A33 and A82. The difference between the two estimates may be due to the fact that the first estimate uses all the cumulative mercury porosimetry information (pressure, volume, surface tension), while the second methodology uses only the median pore radius as input. From these specific surface areas, we can estimate cementation exponents using Equation (3.5). For the first specific surface area estimate, we obtain: m=1.74, 1.79 and 1.75, and for the second: m=1.87, 1.91 and 1.90 for A11, A33 and A82. We can compare these values with the actual values obtained from the porosity and resistivity measurements: m=1.78, 1.71 and 2.13 for A11, A33 and A82. We approach the actual m with our first estimate in the case of A11 and A33; however, even in that case, we fail to predict m for sample A82, which have the most heterogeneous pore size distribution, as we had observed in Figure 3.16.

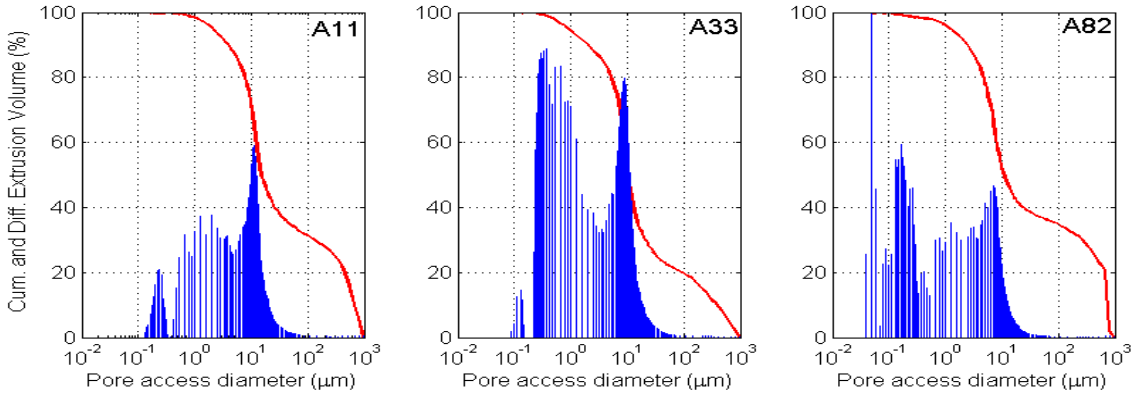

Figure 3.16: Cumulative intrusion curve in red, and differential pore size distribution in blue for core plugs A11, A33 and A82.

Velocities were measured under dry conditions while resistivity was measured under water saturated conditions. We applied Gassmann's equations to estimate the P-wave and S-wave velocities for 100% water-saturated conditions. The rest of the analysis that we show is on the velocity data after performing Gassmann's fluid substitution to 100% water saturation.

Plotting the fully water saturated velocities as a function of porosity (Figure 3.17), we observe that those measured at 40 MPa confining pressure fall very close to the modified upper Hashin-Shtrikman bound shown in blue (MH+ curve in Figure 3.17). In this example, this bound is obtained assuming a critical porosity 0.45.

The differential effective medium (DEM) model fits the laboratory data when we assume a quartz matrix and water-filled ellipsoidal inclusions with aspect ratios between 0.02 and 0.1 for 0 MPa confining pressure, and between 0.05 and 0.2 for 40 MPa confining pressure. Using the self-consistent approximation to model P-wave and

S-wave velocity (Figure 3.18), we observe good fit using the same aspect ratios as for DEM.

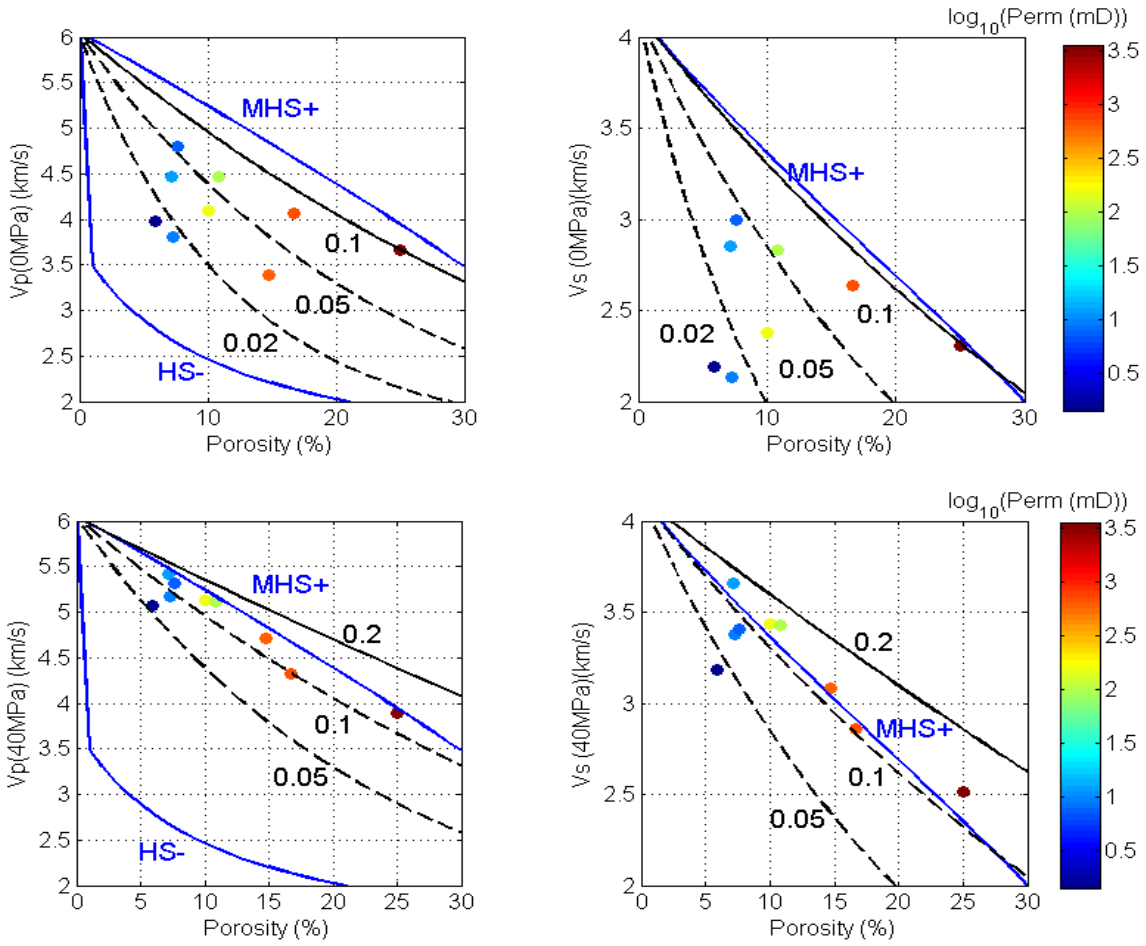

Figure 3.17: P-wave velocity (on the left) and S-wave velocity (on the right) measured at 0 MPa (on top) and 40 MPa (below) confining pressure versus porosity colorcoded by permeability. Velocities were measured at dry conditions, and then Gassmann's fluid substitution was applied. HS- is the lower Hashin-Shtrikman bound. MHS+ is the modified Hashin-Shtrikman bound with a critical porosity of 45%. The black lines are DEM models for different pore aspect ratios.

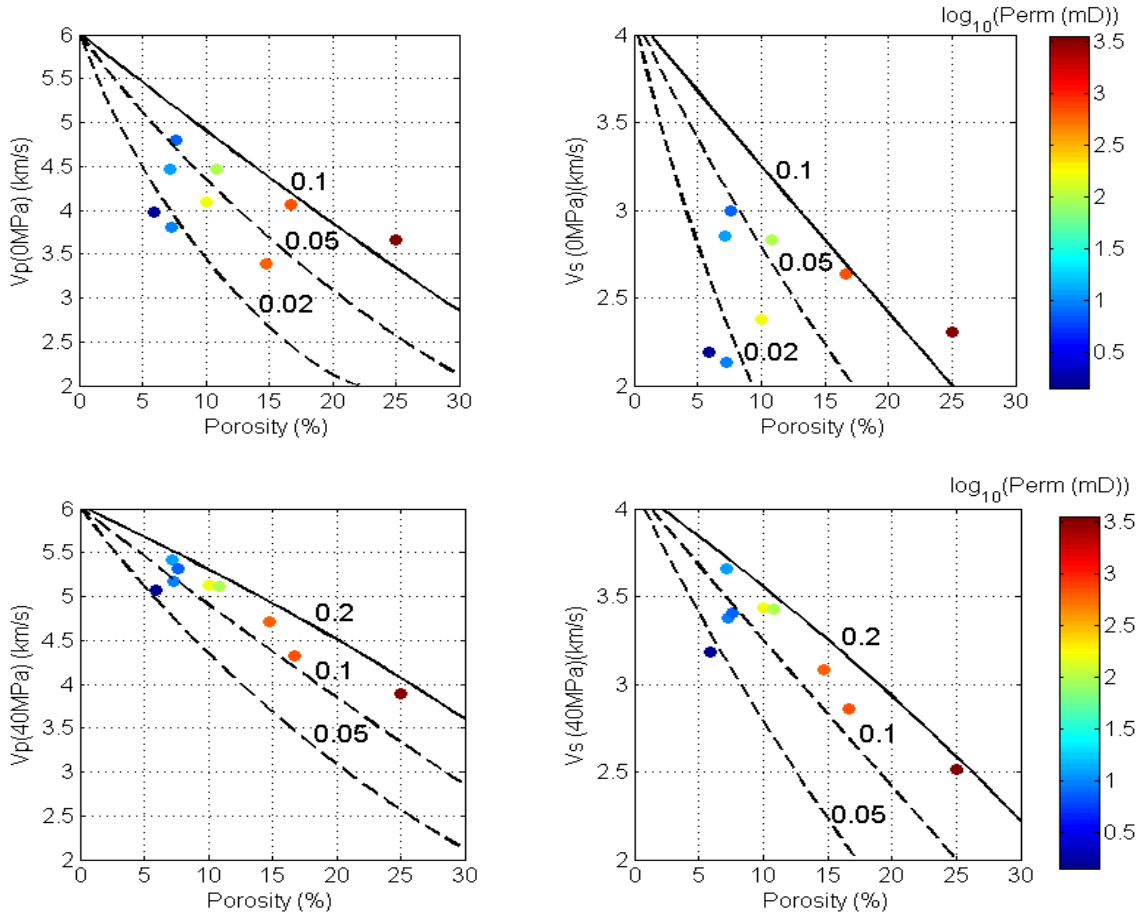

Figure 3.18: Same as Figure 3.17. Black line is the self-consistent model for quartz grains of aspect ratio 1 and different pore aspect ratios.

We also used semi-empirical equations, such as the stiff sand model (Gal et al., 1998), Wyllie's time average (Wyllie et al., 1963), and Raymer-Hunt-Gardner (Raymer et al., 1980) to model the velocity data. In Figure 3.19 we observe that assuming a 100% quartz matrix (solid line) in the stiff sand model, a coordination number 9 and a critical porosity 40%, we obtain a satisfactory fit to most data points for both P- and S-wave velocities at 40 MPa confining pressure, but, as expected, the fit is not satisfactory at 0 MPa confining pressure. We also show the stiff-sand model

estimate assuming 90% quartz and 10% clay as part of the matrix (dashed line in Figure 3.19).

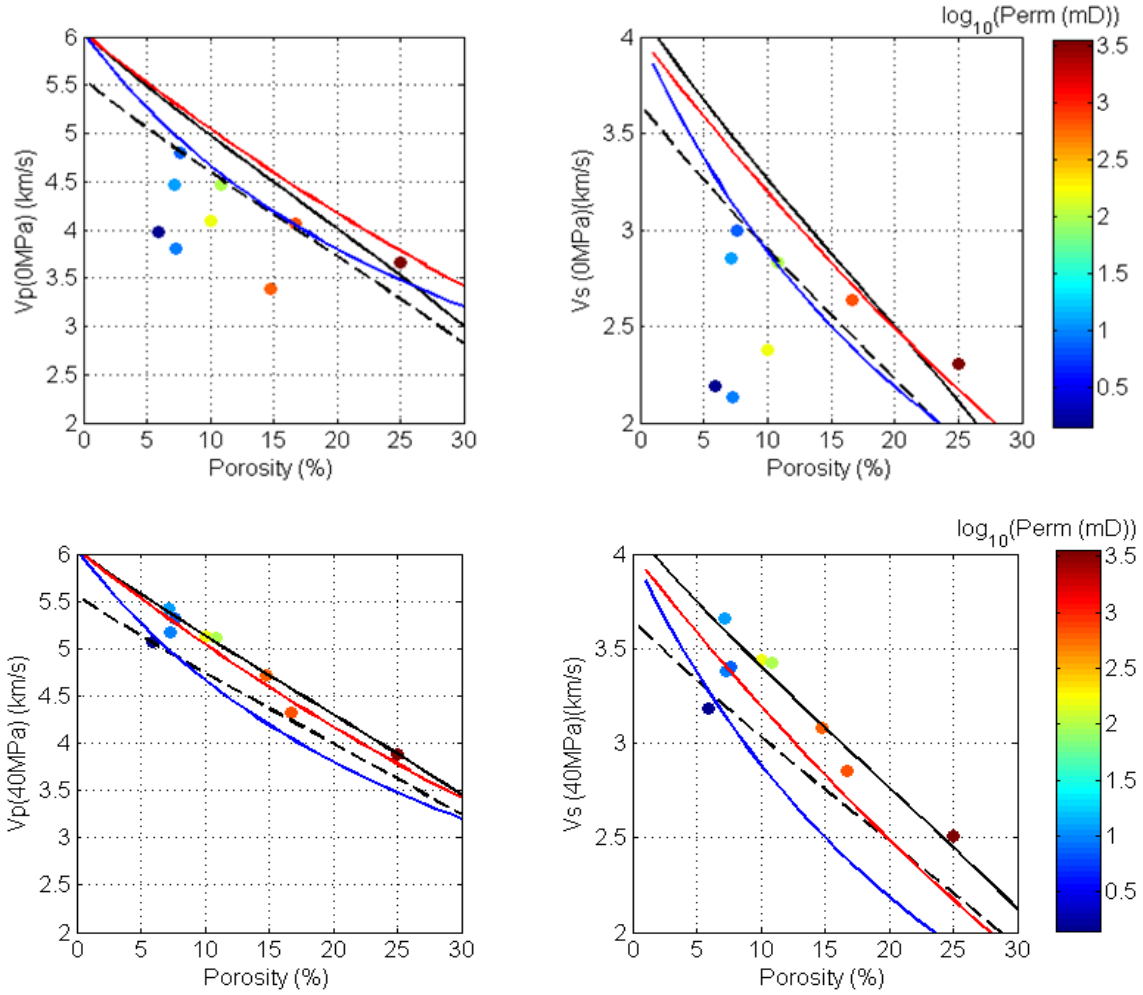

Figure 3.19: Same as Figure 3.18. Solid black line is for the stiff sand model, assuming 100% quartz. Dashed black line is the stiff sand model assuming 90% quartz and 10 % clay. P-wave velocity using Wyllie time average equation is in blue, and using Raymer-Hunt-Gardner's equation is in red. S-wave velocities were estimated from Wyllie's and Raymer-Hunt-Gardner's P-wave velocity using Greenberg-Castagna.

S-wave velocity was computed from P-wave velocity for Wyllie's time average and Raymer-Hunt-Gardner estimates using Greenberg and Castagna (1992) empirical

relations. At 0 MPa confining pressure, these models do not match our data. At 40 MPa confining pressure, Wyllie's time average underpredicts both P- and S-wave velocities, while Raymer-Hunt-Gardner works well for P-wave velocity, but the Greenberg-Castagna equations underpredict the S-wave velocity.

S-wave velocity versus P-wave velocity plots are commonly used to estimate lithology and pore fluid (Mavko et al., 1998). We show these plots (Figure 3.20) for the velocities measured at 40 MPa confining pressure. The best-fit linear relation we have found for these samples (Gassmann-substituted wet samples) is:

$$V_S(km/s) = 0.68 \cdot V_P(km/s) - 0.14 \qquad (3.12)$$

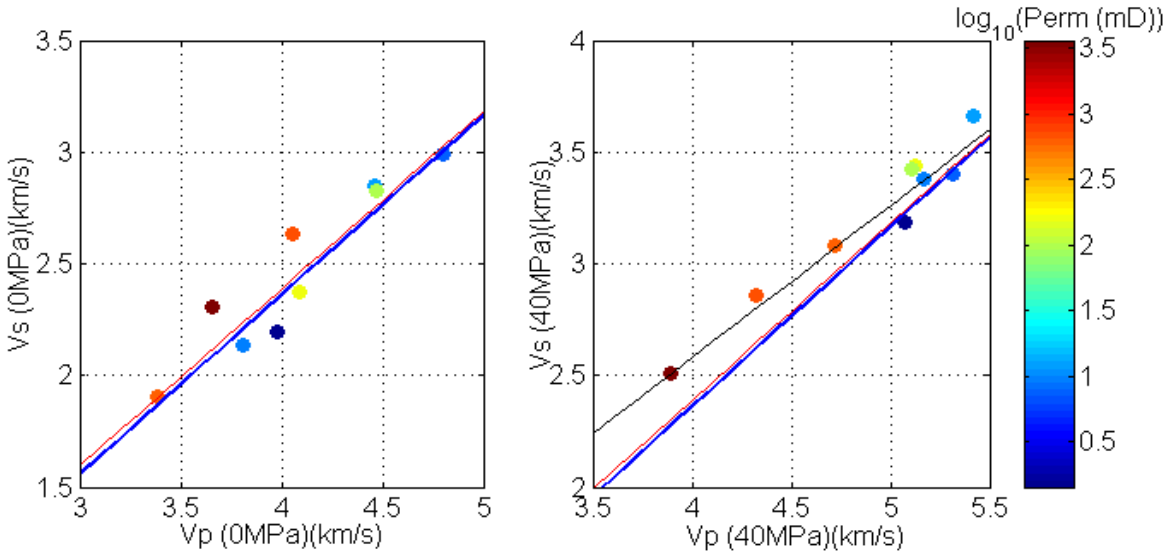

Figure 3.20: S-wave velocity versus P-wave velocity colorcoded by permeability at 0 MPa on the left and at 40 MPa on the right. The blue line is using Castagna et al. (1993) relation (Equation 3.13), and red line is using Han et al. (1986) relation (Equation 3.14). The black line on the right is the best linear fit to the plotted data, as given by Equation 3.12 (the norm of the residuals is 0.223).

Our measurements at 0 MPa confining pressure follow published trends for S- versus P-wave velocity, such as those by Castagna et al. (1993) and Han et al. (1986), given by the following linear trends:

$$V_S(km/s) = 0.804 \cdot V_P(km/s) - 0.856 \quad (3.13)$$

$$V_S(km/s) = 0.794 \cdot V_P(km/s) - 0.787 \ , \quad (3.14)$$

respectively.

At 40 MPa confining pressure, our S-wave velocity values are larger than those predicted by these models from the measured Vp. Fontainebleau sandstones are very clean sandstones, therefore, it is expected that their Vs/Vp ratio is high (Castagna et al., 1993).

3.7 Relation between Velocity and Resistivity

P-wave velocity is highly dependent on pressure, while the dependence of resistivity on confining pressure is reportedly not as strong, in particular for clean sandstones (Lewis et al., 1988; Sharma et al., 1991; Milsch et al., 2008). Formation factor of sandstones can be estimated as a function of pressure (P) using a power law (Schön, 1996):

$$F(P) = F_0 P^g \ , \quad (3.15)$$

where F_0 is the formation factor or normalized resistivity at zero pressure, and g is an empirical constant. For North Sea and Alaskan sandstones measured by Palmer and Pallat (1991), Schön (1996) estimates g to be 0.055.

Plotting the P-wave velocity versus the decimal logarithm of formation factor at 0 MPa confining pressure, we observe a large scatter of the data and a poor linear fit ($R^2 = 0.33$) (Figure 3.21). If we estimate formation factor at 40 MPa using Equation (3.15), and g of 0.055, and plot it versus the P-wave velocity measured at 40 MPa confining pressure, the data scatter is smaller, and we obtain a better linear fit to the data ($R^2 = 0.84$). In clean sandstones, it is expected that both resistivity and P-wave velocity are mainly a function of porosity, and therefore a relation between these two properties can be derived.

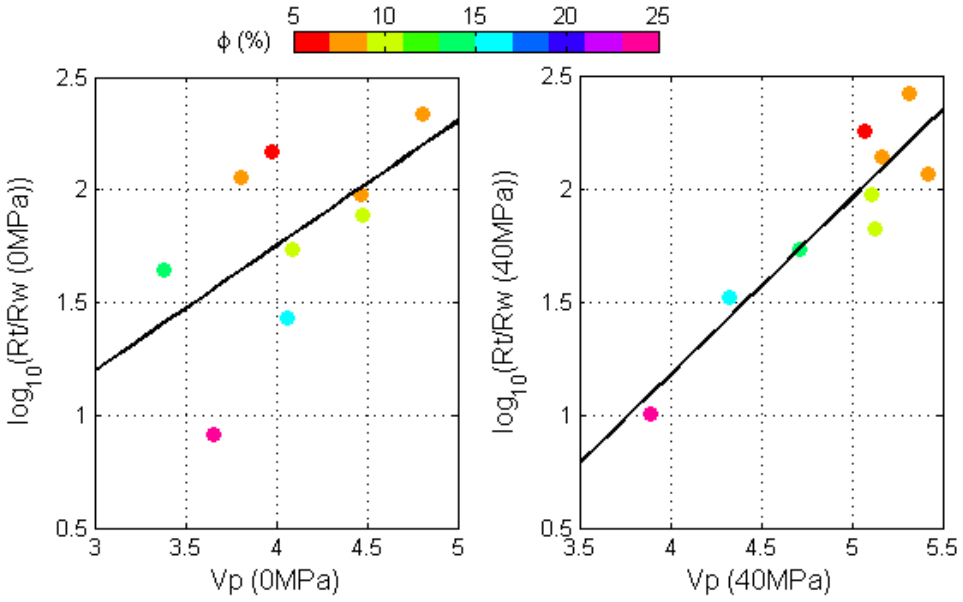

Figure 3.21: Normalized resistivity or formation factor versus P-wave velocity measured at 0 MPa confining pressure on the left and at 40 MPa on the right. Gassmann fluid substituted velocity is plotted, colorcoded by porosity. A linear fit is also plotted.

The empirical equation that we obtain between normalized resistivity and P-wave velocity in km/s at 40 MPa is the following:

$$\log_{10}(Rt/Rw) = 0.782 \cdot V_P(km/s) - 1.954 . \quad (3.16)$$

The data points corresponding to samples A117 and B102 fall above and below the linear trend in Figure 3.21, respectively (see Figure 3.22 for labeled data points). We observe the same for samples A82, A11 and A33. Core plugs A117 and B102 have porosity around 10%, and permeabilities 103 and 157 mD, correspondingly. Samples A82, A11 and A33 have porosity around 7%, and permeabilities 7.08, 9.98 and 12.45 mD, respectively. Therefore, the scatter in resistivity versus velocity for these samples correlates with permeability.

We also applied P-wave velocity – resistivity transforms to compute resistivity as a function of P-wave velocity. First, we used Faust (1953) relation between velocity and resistivity:

$$\frac{R_t}{R_W} = \frac{1}{Z}\left(\frac{V_P}{\gamma}\right)^6 \quad , \quad (3.17)$$

where γ is 2.888, if velocity is in km/s. Z is the depth of the sandstone in kilometers. Assuming a confining pressure of 23 MPa/km, and since the measurement was taken at 40 MPa, we can estimate that corresponds to Z =1.74 km. As Hacikoylu et al. (2006) showed, we observe that Equation (3.17) overestimates the resistivity (blue curve in Figure 3.22).

Hacikoylu et al. (2006) derived a velocity – resistivity transform for friable shaley sandstones, whose velocities followed the soft sand model (Dvorkin and Nur, 1996). The sandstones in this study are stiffer, and their velocities are better modeled using the stiff sand model by Gal et al. (1998) (see Figure 3.19). A P-wave velocity –

resistivity transform can be obtained by combining the stiff sand model and the lower Hashin-Shtrikman bound for resistivity as a function of porosity, as derived by Berryman (1995), and modified by Hacikoylu et al. (2006):

$$\frac{R_t}{R_w} = 2 + \left[\frac{1.56 - 1.5\phi}{\phi - 0.04} \right]. \tag{3.18}$$

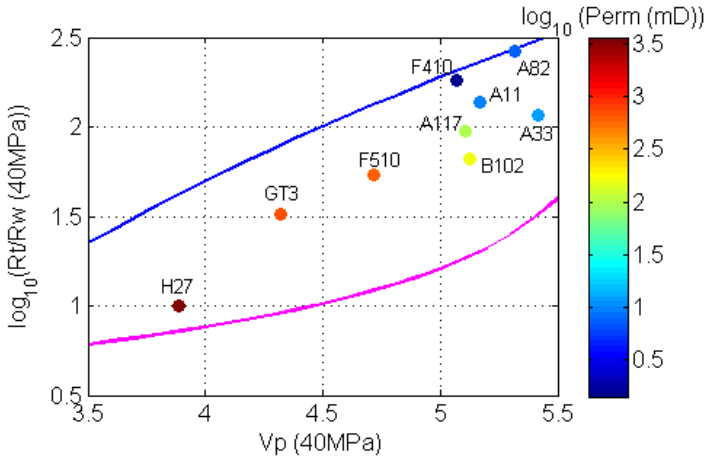

Figure 3.22: Same as Figure 3.21, but colorcoded by the decimal logarithm of permeability in mD. Resistivity curves computed using P-wave velocity – resistivity transform derived from stiff sand model and a modified lower Hashin-Shtrikman (Hacikoylu et al., 2006) in magenta, and from Faust (1953) in blue.

The transform we obtain by combining it with the stiff sand model is:

$$\frac{R_t}{R_W} = 2 + \left[\frac{0.500 + 0.177 \cdot V_P(km/s)}{(0.686 - 0.118 \cdot V_P(km/s))} \right]. \tag{3.19}$$

These two models, Faust (1953) and stiff sand combined with the resistivity low bound, work as lower and upper bounds for the resistivity versus P-wave velocity data, respectively (Figure 3.22).

If instead of using the low bound for resistivity, we use Archie's equation, we find a transform that can predict resistivity from the velocity data (Figure 3.23):

$$\frac{R_t}{R_W} = \left[\frac{8.49}{(6.00 - V_P(km/s))} \right]^m . \qquad (3.20)$$

This transform depends on the cementation exponent (m). We used m =1.6, 1.8 and 2.1 (obtained earlier in this chapter from our resistivity – porosity modeling) to compare them with our data (Figure 3.9).

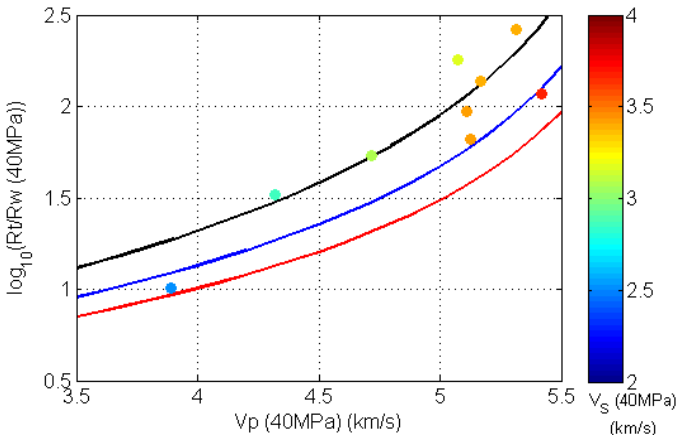

Figure 3.23: Same as Figure 3.22, but colorcoded by S-wave velocity. Resistivity curves computed using P-wave velocity – resistivity transform derived from stiff sand model and Archie is displayed. Red is for a cementation exponent in Archie of 1.6, blue is for 1.8 and black 2.1.

3.8 Conclusions

After examining the permeability - porosity relation of 23 Fontainebleau sandstones, we found that they follow Kozeny-Carman's relation with tortuosity 2.5 and percolation porosity 2%, for a mean grain size, as observed from CT scan, 250 microns. Two different linear trends, one for low porosities and one for high

porosities, in the logarithm of permeability versus logarithm of porosity domain can be defined too, which are similar to those found by Bourbie and Zinszner (1985). A single trend can be defined if we plot the logarithm of permeability versus the logarithm of porosity minus the percolation porosity.

As we saturate four samples with water with three different salinities: 10,000, 40,000 and 100,000 NaCl ppm, we find these samples follow a linear trend with intercept at the origin, which means they are clean sandstones, with no significant presence of clay minerals that contribute to the resistivity.

Plotting the normalized resistivity measurements as a function of porosity, we find they fall between the lower and modified upper Hashin-Shtrikman bounds for sandstones. Differential effective medium model assuming water as the background and quartz grains as the inclusions underpredicts the measurements, but it could be used as narrower lower bound.

Self-consistent approximation using a grain aspect ratio of 1, and pore aspect ratios of 0.02, 0.05 and 0.1 are very close to the resistivity values measured in the laboratory; therefore it can be a good model to use to predict resistivity in clean sandstones given fluid and mineral properties.

Archie's relation predicts the normalized resistivity measurements given the porosity. An average cementation exponent between 1.6 and 1.8 works for most of our samples, although as porosity decreases, the cementation exponent seems to increase.

We derive a permeability versus formation factor relation from the laboratory data, which has a high R^2, but the norm of the residuals is also high. We conclude that

overall formation factor is not a good predictor of permeability, even in the case of clean sandstones.

After measuring P-wave and S-wave velocity as a function of confining pressure, we do not observe hysteresis, as we load and unload the sample. We can model the velocity data using self-consistent approximation with a grain aspect ratio of 1, and pore aspect ratios of 0.2, 0.1 and 0.05 at 40 MPa confining pressure, and pore aspect ratios of 0.1, 0.05 and 0.02 at 0 MPa confining pressure. The stiff sand model and Raymer-Hunt-Gardner equation are also good models for the P- and S-wave velocity of these clean sandstones at 40 MPa confining pressure.

Finally, we found a linear fit between the P-wave velocity and the decimal logarithm of the normalized resistivity, with deviations that correlate with differences in permeability. Faust's relation and a combination of stiff sand model and the modified lower Hashin-Shtrikman bound for resistivity can be used as upper and lower bounds for the resistivity as a function of velocity, respectively. Combining the stiff sand model and Archie for cementation exponents between 1.6 and 2.1, we can model resistivity as a function of P-wave velocity.

SAMPLE	Porosity	Perm (mD)	Sw	R (ohm m)	R/Rw
A11	0.07	10	0.80	29.81	112.94
A16	0.07	6	0.70	37.44	108.01
A33	0.07	12	0.80	24.99	94.95
A82	0.08	7	0.65	88.29	216.49
A87	0.10	50	0.76	19.34	65.67
A89	0.08	26	0.82	32.08	126.43
A117	0.11	103	0.75	23.47	76.76
B31	0.11	107	0.85	14.91	63.47
B86	0.09	78	0.85	25.02	106.07
B101	0.11	121	0.84	18.23	76.54
B102	0.10	157	0.90	11.28	54.23
B108	0.08	29	0.83	44.69	179.50
F510	0.15	592	0.90	9.24	44.28
GT3	0.17	704	0.91	5.47	26.79
GW18	0.16	637	0.91	6.70	32.98
GW19	0.18	912	0.92	6.91	34.19
GW23	0.18	965	0.92	3.55	17.56
GW28	0.18	896	0.86	3.94	17.32
H27	0.25	3630	0.89	1.76	8.24
H42	0.24	2894	0.88	1.87	8.59
H74	0.24	3079	0.85	2.38	10.18
F410	0.06	1	0.70	51.24	147.38
F570	0.10	32	0.71	17.40	51.88

Table 3.2: Porosity is the Helium porosity, permeability is in mD, Sw is the water saturation reached for resistivity measurements, R is measured resistivity in ohm m, R/Rw is the normalized resistivity or formation factor computed using a saturation exponent (n) of 2, and Rw=0.17 ohm.m.

SAMPLE	A11		SAMPLE	A33		SAMPLE	A82	
Pc (Mpa)	Vp (km/s)	Vs (km/s)	Pc (Mpa)	Vp (km/s)	Vs (km/s)	Pc (Mpa)	Vp (km/s)	Vs (km/s)
Loading								
0	3.28	2.17	0	4.17	2.89	0	4.78	3.04
2.5	3.62	2.45	2.5	4.81	3.24	2.5	4.96	3.17
7.5	4.06	2.74	7.5	5.13	3.51	5	5.05	3.23
10	4.48	3.05	10	5.21	3.62	10	5.20	3.35
20	4.81	3.19	20	5.31	3.65	20	5.30	3.41
30	5.07	3.36	30	5.35	3.69	30	5.32	3.42
40	5.17	3.43	40	5.42	3.72	40	5.38	3.46
Unloading								
35	5.15	3.42	35	5.40	3.72	35	5.34	3.46
25	5.05	3.37	25	5.34	3.68	25	5.32	3.42
15	4.84	3.27	15	5.27	3.64	15	5.24	3.36
5	4.50	3.12	5	5.09	3.48	7.5	5.10	3.29
1.5	-	-	1.5	4.81	3.31	4	5.01	3.19
0	3.57	2.44	0	4.51	2.96	0	4.78	3.13

Table 3.3: P- and S-wave velocity in km/s measured in one loading and unloading cycle for samples A11, A33 and A82.

SAMPLE	A117		SAMPLE	B102		SAMPLE	F510	
Pc (Mpa)	Vp (km/s)	Vs (km/s)	Pc (Mpa)	Vp (km/s)	Vs (km/s)	Pc (Mpa)	Vp (km/s)	Vs (km/s)
Loading								
0	4.37	2.89	0	3.92	2.43	0	2.98	1.96
1	-	-	1	-	-	1	3.40	2.27
2.5	4.59	3.02	2.5	4.23	2.69	2.5	3.84	2.55
7.5	4.81	3.15	7.5	4.59	3.03	7.5	4.26	2.80
10	4.94	3.29	10	4.72	3.15	10	4.39	2.93
20	5.05	3.35	20	4.95	3.36	20	4.58	3.10
30	5.09	3.45	30	5.06	3.48	30	4.71	3.16
40	5.12	3.51	40	5.13	3.53	40	4.74	3.18
Unloading								
35	5.11	3.49	35	5.13	3.51	35	4.71	3.17
25	5.07	3.44	25	5.09	3.50	25	4.63	3.13
15	5.02	3.31	15	4.97	3.38	15	4.52	3.08
5	4.81	3.12	5	4.46	2.80	5	4.16	2.75
3	-	-	3	-	-	3	4.01	2.61
0	4.37	2.89	0	4.00	2.51	0	3.84	2.46

Table 3.4: P- and S-wave velocity in km/s measured in one loading and unloading cycle for samples A117, B102 and F510.

SAMPLE	GT3		SAMPLE	H27		SAMPLE	F410	
Pc (Mpa)	Vp (km/s)	Vs (km/s)	Pc (Mpa)	Vp (km/s)	Vs (km/s)	Pc (Mpa)	Vp (km/s)	Vs (km/s)
Loading								
0	3.90	2.73	0	3.57	2.45	0	3.55	2.22
2.5	-	-	2.5	3.57	2.46	2.5	-	-
5	4.00	2.74	7.5	3.63	2.48	5	4.31	2.65
10	4.04	2.78	10	3.63	2.49	10	4.80	2.98
20	4.12	2.84	20	3.69	2.56	20	4.80	3.11
30	4.17	2.91	30	3.78	2.62	30	4.95	3.15
40	4.23	2.97	40	3.86	2.67	40	5.08	3.22
Unloading								
34	4.22	2.95	35	3.84	2.66	35	5.06	3.21
25	4.15	2.88	25	3.73	2.61	25	-	-
15	4.08	2.81	15	3.63	2.55	15	-	-
7	4.03	2.75	5	3.58	2.46	8	4.78	2.99
2.5	3.92	2.74	2.5	-	-	2.5	4.59	2.91
0	3.80	2.62	0	3.23	2.27	0	4.29	2.68

Table 3.5: P- and S-wave velocity in km/s measured in one loading and unloading cycle for samples GT3, H27 and F410.

Chapter 4
Effective Medium Modeling of Laboratory Velocity and Resistivity Data on Carbonates from the Apulia Platform, Italy

4.1 Abstract

This chapter describes joint effective-medium modeling of elastic and resistivity laboratory data obtained on a set of outcrop carbonate samples from the Apulia Platform in Italy. The challenge is to model both the elastic-wave velocity and resistivity using a single theoretical approach. The candidate models are (a) the differential effective-medium (DEM) theory and (b) the self-consistent approximation (SC). DEM predicts resistivity, but underpredicts P-wave velocity, when we assume that the mineral phase corresponds to the inclusions and the pore fluid is the background. However, DEM does accurately describe the elastic properties when pores are assumed as inclusions; but it fails to describe resistivity, because it lacks adequate pore connectivity. SC treats both rock components, the pores and the matrix,

as conceptually symmetric, thus implicitly providing the connectivity needed to match the measured resistivity. Therefore, SC makes it possible to match both the elastic data and the measured resistivity using one set of model parameters.

We show that SC is a robust approach to modeling both velocity and resistivity in our carbonate rock samples, particularly when using needle-like pores, which tend to be stiff but well connected.

Carbonate rocks in general have inter- and intra-granular porosity, both of which affect their elastic and electrical properties. We model P-wave velocity and resistivity laboratory measurements taking into account these two types of porosity separately, using the self-consistent approximation for each. We use needle-like inter-granular pores in the model, since they are stiff and well-connected as is observed in these carbonate samples. We consider two models of intra-granular pores: stiff pores with an aspect ratio 0.5, and needles. The small resistivity values observed at low porosities could not be explained here, since for this model almost no conduction seems to occur through the intra-granular pores. One way to address this problem is to model the intra-granular porosity using Archie's equation for resistivity, in which case, as intra-granular porosity increases, resistivity decreases, and the laboratory measurements are better modeled. The inter-granular porosity in this case is still modeled using the self-consistent approximation.

4.2 Introduction

Carbonate rocks have a complex pore network, composed of inter- and intra-granular porosity. Here, we model velocity and resistivity laboratory measurements in

a consistent manner for a set of carbonate rocks from the Apulia Platform in Italy that includes the Mt. Acuto (Late Cretaceous), Peschici (Paleocene – Eocene) and Gravina formations (Late Pliocene – Late Pleistocene) (for a more detailed description, see Vanorio et al., 2008). The depositional settings range from platform to basin. The Apulia Platform is part of the Apennine thrust belt, and is bounded by basinal deposits. This platform was a relatively small isolated carbonate bank out of the reach of terrigenous sediments throughout the Jurassic and the Cretaceous (Bosellini et al., 1999). During the Oligocene through the Pliocene, thrusted sheets were emplaced due to convergence from the southwest, which then formed the Apennines Mountains and also a foreland basin. This basin was filled by Pliocene-Quaternary terrigenous deposits (Borgomano, 2000).

The samples in this study cover a wide range of porosity (5 to 52 %), and their lithologic composition is mostly calcite, with some samples having significant dolomite fractions. The resistivity and velocity measurements for this case will be modeled using both theoretical and empirical models. The purpose is to better understand the porous network (porosity and permeability) of these carbonate samples, and how these characteristics reflect on their elastic and electrical properties.

4.3 Method

Resistivity measurements were conducted on 125 core plugs: 31 from the Mt. Acuto formation (MA), 51 from the Peschici formation (FP), and 43 from the Gravina formation (GR and MAT). The core plugs have a diameter of approximately 2.5 cm, and vary in length between 2.4 and 3 cm. Resistivity was measured at 1 kHz at

benchtop conditions using the 4-electrode method, with the benchtop set-up that is part of the Core Lab's Advanced Resistivity System Model 300. The instrumental error for the measured resistivities is 10%.

Core plugs were saturated with a calcium carbonate solution, and their water resistivity was monitored for a 48-hour period before the saturated rock resistivity measurements were performed. A calcium carbonate solution was used to ensure that the solution was in chemical equilibrium with the sample, and to minimize dissolution. The resistivity of water was recorded before performing each measurement. At the time of the measurements, the resistivity of the water was 28 ± 5 ohm m. One-hundred percent water saturation was not reached in these samples, particularly in those with low porosity; The average saturation was 90%. Archie's equation was used to estimate the resistivities at full saturation (R_0) from the measured resistivity (R_t) at saturation S_W, assuming a saturation exponent (*n*) of 2, as follows:

$$R_0 = R_t S_W^{\,n}. \tag{4.1}$$

The P-wave (1 MHz frequency) and S-wave (700 kHz frequency) ultrasonic velocities were measured at dry bench-top conditions by Cinzia Scotellaro (Vanorio et al., 2008). The error for the velocity measurements is around +/- 1%. We used Gassmann's (1951) fluid substitution to predict the velocities at full water saturation. This was to avoid velocity dispersion effects that would be associated with fluid-saturated ultrasonic measurements. Another reason to use Gassmann's equation is that the systems to measure velocity and resistivity are not integrated, so two separate

saturation processes are required, and it is not trivial to repeat saturations in carbonate samples with complex microstructure. Figure 4.1 compares velocity measurements performed under saturated conditions (Vanorio et al., 2008) to the corresponding Gassmann's modeled velocities for the samples under study. We observe that Gassmann's equation, as expected, underpredicts the ultrasonic velocity, in particular for the high porosity (low-velocity) samples.

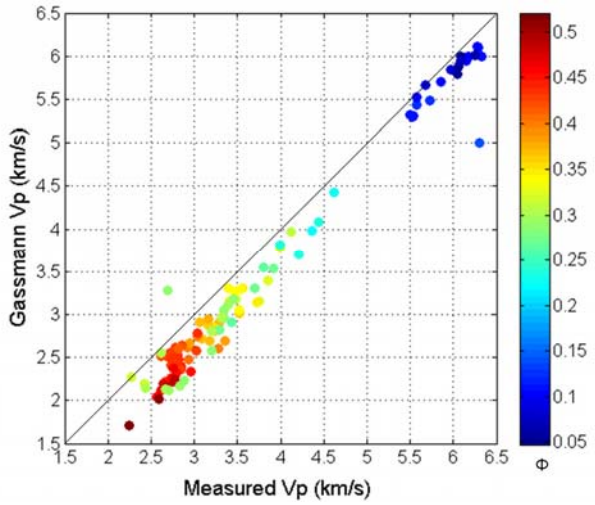

Figure 4.1: Gassmann-computed velocity versus measured ultrasonic velocity for the carbonate samples under study, colorcoded by porosity.

The mineralogical composition of the samples was estimated by X-ray diffraction (XRD) analysis, and porosity was computed from the composition, the dry weight, and the volume of the samples (see Tables 4.1 through 4.3 at the end of this chapter). This porosity was compared to porosity measured using Helium porosimetry, showing close agreement (Figure 4.2). Therefore, we assumed the computed porosity to be the total porosity of the samples. All these porosity, permeability and XRD measurements were performed by Cinzia Scotellaro (Vanorio et al., 2008). Some of the XRD

measurements were performed by Marco Voltolini at the University of California, Berkeley.

Klinkenberg-corrected nitrogen permeability measurements are available for some of the samples (Vanorio et al., 2008). All the data measured for this set of samples is displayed in Tables 4.4 through 4.6 at the end of this chapter.

Measurements performed by Carrara et al. (1999) on samples from the Gravina formation are also included in this study. For these measurements, the resistivity of the saturating water was 78 ohm·m. The data available for these samples included weight, length, diameter, dry-rock P-wave velocity, saturation and resistivity. The porosity of the samples was recomputed using the mineralogy identified for Gravina Formation samples by Vanorio et al. (2008).

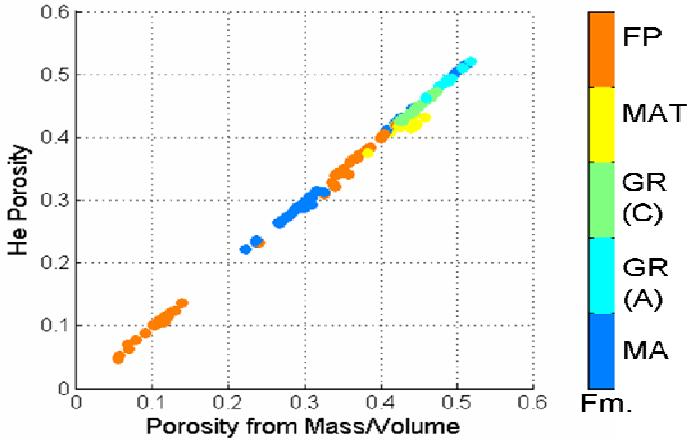

Figure 4.2: Porosity obtained from Helium porosimeter versus that estimated from dry weight, volume and X-ray diffraction mineralogy. The data are color-coded by formation.

4.4 Differential Effective Medium versus Self-Consistent Effective Medium Modeling

Previous work that has attempted joint effective-medium modeling of elastic velocities and electrical resistivity includes that by Sheng and Callegari (1984). They implemented differential effective-media (DEM) modeling for sandstones with a range of P-wave velocities between 4.5 and 6 km/s, and normalized resistivities – measured resistivity normalized by the resistivity of the saturating water – between 10^2 and 10^5 ohm·m. In contrast, previous velocity and resistivity measurements by Carrara et al. (1999) for Gravina limestone samples showed normalized resistivity values on the order of 1 to 5 ohm·m, and velocities around 2 km/s. They modeled both their velocity and resistivity measurements using the harmonic average of the solid and fluid elastic moduli and density for the effective elastic properties, and the harmonic average of their resistivities for the effective resistivity; this assumes very compliant and conductive rocks.

For electrical conduction to occur, pore connectivity is very important. If pores saturated with a conductive fluid are added as inclusions in an isolating calcite matrix, DEM theory predicts that resistivity will be very high for almost all porosities, as shown in blue in Figure 4.3b. Therefore, even though DEM modeling assuming pores as inclusions tends to work well for elastic data (see blue line in Figure 4.3a), it does not adequately explain the electrical behavior observed in our carbonate samples.

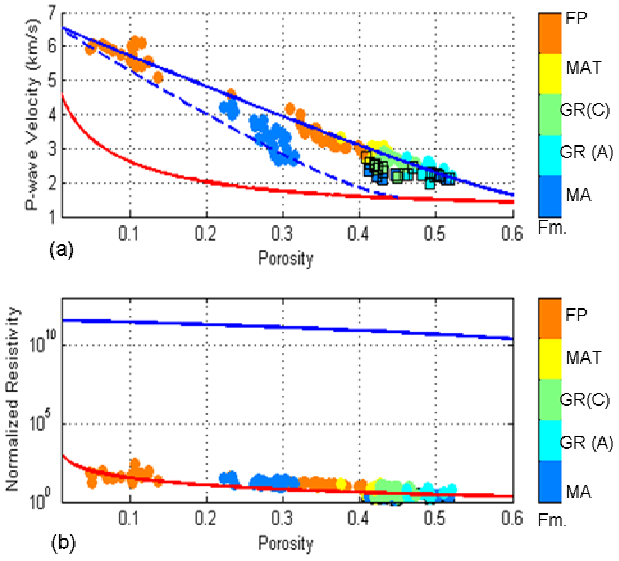

Figure 4.3: DEM modeling of velocity and normalized resistivity. Open squares are measurements from Carrara et al. (1999). The red curves are the DEM model assuming the water-saturated pore space as the background and the mineral grains (calcite) as the inclusions. The blue curves are the DEM model assuming calcite as the background and the water-saturated pores as the inclusions. For the velocity, we used modified DEM (Mukerji et al., 1995), assuming critical porosity 0.65 (solid line) and 0.45 (dashed line). Spherical inclusions are used.

On the other hand, if we add calcite grains in a conductive background, using DEM theory, we find that the predicted electrical behavior is closer to that observed for our water-saturated carbonate rocks even at low porosity, as shown in red in Figure 4.3b; however, the velocities predicted by DEM in this case will be too low and cannot explain the measurements (see red curve in Figure 4.3a).

The self consistent (SC) effective-medium estimate is symmetric for all the constituents. This is in contrast with DEM modeling, where one of the components has to be chosen as the host to the others (Berryman, 1995). This is an important difference, particularly when jointly modeling elastic and electrical properties.

Hence, we applied SC effective medium modeling, assuming solid spherical calcite grains. We tested pores shaped as spheres, oblate ellipsoids with aspect ratio 0.10, needles, and different combinations of all three. We found that a combination of needle-like and ellipsoidal pores of aspect ratio between 1 and 0.10, provides reasonably accurate approximations simultaneously for the measured velocity and normalized resistivity versus porosity (Figure 4.4).

The SC estimates for normalized resistivity are still below some of the measured values and above some others, but are generally consistent with the behavior exhibited in the data (Figure 4.4b). The results still show scatter, especially at low porosities. Some of the low-resistivity values can be better modeled by including pores of aspect ratios lower than 0.1, but these data would underestimate the P-wave velocity values, because lowering the aspect ratio makes the pores more compliant (Mavko et al., 1998). S-wave velocity can also be adequately modeled using the same combination of ellipsoidal and needle-like pores as we use for P-wave velocity (Figure 4.5).

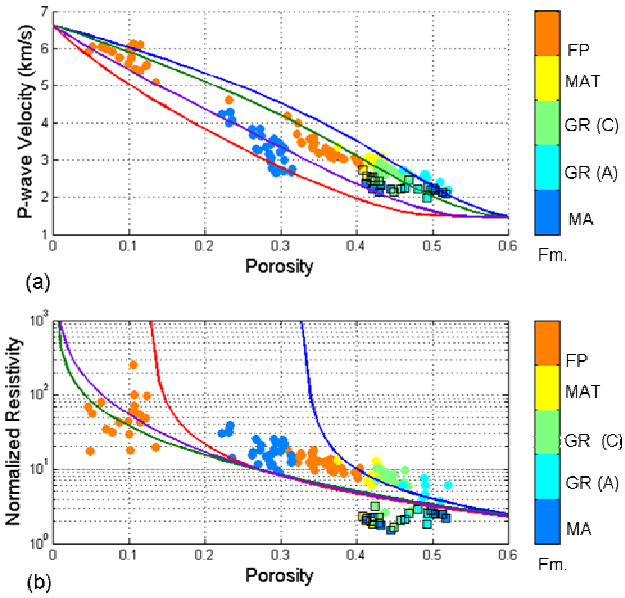

Figure 4.4: SC modeling of velocity and normalized resistivity for same plugs as those in Figure 4.2. We assume grains with aspect ratio 1. The blue line is for pores with aspect ratio 1, the red line is for pores of 0.10 aspect ratio, the green line is for needle-like pores, and the purple line is for a combination of 50% needle-like pores and 50% ellipsoidal pores of aspect ratio 0.10.

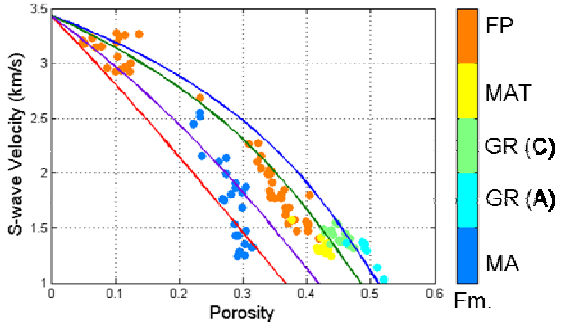

Figure 4.5: Same as Figure 4.4a but for S-wave velocity.

4.5 Modeling Resistivity using Archie's Equation and Velocity using the Stiff-Sand Model

One of the most common models for resistivity in sedimentary rocks, including carbonates, is Archie's equation. In the case of carbonates, the cementation exponent m is interpreted as an indicator of the type of porosity. Assuming a=1, typical values of m given by Schön (1996) include:

- m = 1.7 to 1.8 for chalky limestones,
- m = 1.8 to 2.0 for crystalline and granular carbonates, and
- m = 2.1 to 2.6 for carbonates with vugs.

For our dataset, we observed that the high-porosity carbonates tend to be granular carbonates; however they seem to be better modeled with a high m, characteristic of carbonates with vugs. Some of the carbonates, particularly at low porosities, appear to be better fit by the m exponent corresponding to chalky carbonates or even lower (between 1.5 and 1.8).

The elastic properties of carbonates can also be modeled using semi-empirical models, such as the stiff-sand model. At zero porosity, the elastic properties are those of the mineral phase, and at critical porosity are those given by the Hertz-Mindlin theory (Mindlin, 1949). For the stiff-sand model, these two end-points are connected by the modified upper Hashin-Shtrikman bound (Gal, et al., 1998).

The stiff-sand model fits the data if we use a calcite mineral frame with a critical porosity 0.55, for both P-wave and S-wave velocity (Figure 4.7). Some of the samples have dolomite; therefore, they are better fit when calcite is replaced by dolomite in the

modeling. Another possible explanation for the underprediction of the model for some of the samples is that the critical porosity could be larger than 0.55, which can happen in the case of chalks (Nur et al., 1998). The Mt. Acuto (MA) samples (in blue) are better modeled using a smaller critical porosity, such as 0.4, which is the typical value used for sandstones (Nur et al., 1998).

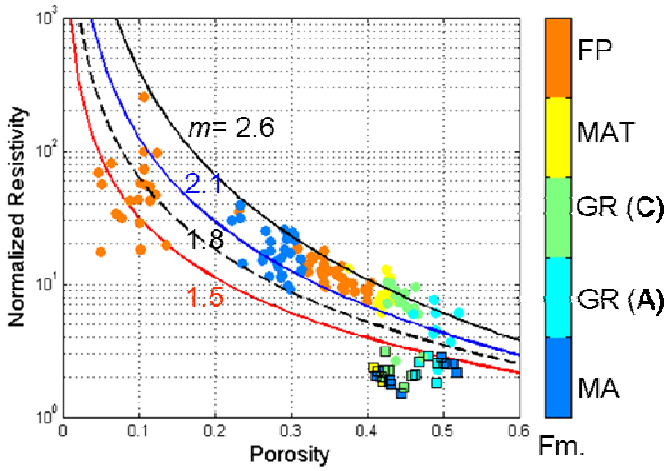

Figure 4.6: Modeling of normalized resistivity, for same plugs as those in Figure 4.4, using Archie (1942)'s equation with m= [1.5, 1.8, 2.1, 2.6], from top to bottom curve, and a =1.

4.6 Modeling Velocity and Resistivity including Inter- and Intra-Granular Porosity Effects

The samples used in this study have not only inter-granular porosity, but also moldic porosity, with numerous fossils that enhance intra-granular porosity (Vanorio et al., 2008). The combination of the two has important effects on the elastic and electrical properties of these rocks.

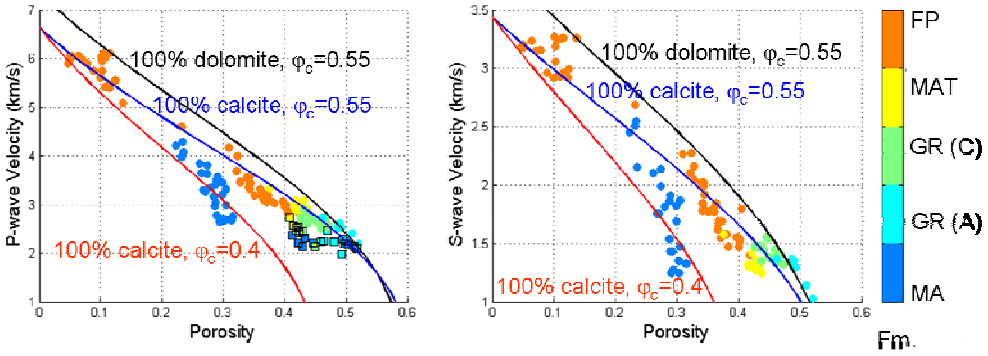

Figure 4.7: Modeling of P-wave velocity on the left, and S-wave velocity on the right, for the same plugs as those in Figure 4.6, using 100% dolomite matrix and 55% critical porosity in black, 100% calcite matrix and 55% critical porosity in blue, and 100% calcite and 40% critical porosity in red.

One way to include both the inter- and the intra-granular porosity effects in our analysis is to model these rocks as packs of porous grains, where one of the pore networks (e.g., within the grains or intra-granular) is modeled using an effective medium model, and the other pore network (e.g., inter-granular) is modeled using semi-empirical relations or other effective-medium approximation. Previous studies that have taken this approach include Ruiz and Dvorkin (2007), and Sen (1997).

Ruiz and Dvorkin (2007) introduced the porous-grain–stiff-sand (PGST) model. In their work, each grain's elastic modulus is computed using differential effective-medium theory. Then, the stiff-sand model (Gal et al., 1998) is used to model the elastic moduli of the pack of porous grains. Sen (1997) implemented a similar model for resistivity of carbonate rocks with micro-porosity. An effective-medium model (either Maxwell-Garnett, self-consistent, or differential effective medium) was used to

model the rock as a whole, and each component of the rock was modeled, obeying Archie's relation (Archie, 1942).

Our approach is to model the velocity and resistivity of a pack of porous grains using the SC effective-medium approximation, assuming that the aspect ratio of the solid inclusions is 1.0, and that the rock includes a combination of needle-like and ellipsoidal pores of aspect ratio 0.1 (60% and 40% of the pores by volume, respectively) for the inter-granular porosity. Four different intra-granular porosities are modeled: 1, 5, 10 and 20%. To obtain the elastic moduli, the intra-granular porosity is modeled using the SC approximation for pores with an aspect ratio 0.5. Assuming the intra-granular pores with this high aspect ratio results in high resistivity for all total porosity values below the intra-granular porosity, as we can see in Figure 4.8. This is because of the low connectivity of round inclusions. Also, since the intra-granular pores are very stiff, the P-wave velocity for the rocks with higher intra-granular porosity is larger. This model works for most of our samples, particularly those with porosity above 20%. A very similar result can be obtained using Sen's (1997) approach by modeling the pack of porous grains using SC, and the intra-granular pores using Archie's relation and a cementation exponent of 2.6 (Figure 4.9).

Our next approach is to model the pores within the porous grains as needles, which resulted in the collapse of all the normalized resistivity lines to the model curve obtained for zero intra-granular porosity (compare curves in Figure 4.10b and the green curve in Figure 4.4b). Notice that the models with larger intra-granular porosity predicted slightly smaller resistivity as the intra-granular porosity increased, at the

expense of inter-granular porosity (the shorter dashed line corresponding to 5% intragranular porosity in Figure 4.10b is below the longest dashed line corresponding to 1% intragranular porosity).

We next model the intra-granular porosity using Archie's equation (Archie, 1942) as first proposed by Sen (1997), instead of SC theory (Figure 4.11). Modeling the intra-granular porosity using Archie's equation means that this type of porosity has an important contribution to the electrical conductivity of the rock, and the larger the intra-granular porosity, the lower the rock resistivity. This is similar to what was observed when intra-granular pores were modeled as needles. Resistivity measurements for plugs with 10% porosity show a large scatter.

Let us examine the results for four of these plugs with 10% porosity; two with P-wave velocities close to 6 km/s (let us call them the A1 and A2 plugs) and two with P-wave velocities close to 5.5 km/s (let us call them the B1 and B2 plugs). The normalized resistivity (measured resistivity normalized by the pore water resistivity) for the A1 and A2 plugs is 14.45 and 17.46, compared to 21.52 and 22.70 for the B1 and B2 plugs. These observations show that for the same porosity, plugs with high velocity (A1 and A2) have lower resistivity. This would validate the hypothesis that the stiff intra-granular pores are still contributing to the electrical conductivity of the rock, and that modeling them as needles or using Archie's equation may be reasonable.

If we observe thin sections for A2 and B2 plugs (Figure 4.12), we see that one of the plugs with larger velocity (A2) seems to have more pores which appear close to

circular in cross-section (high aspect ratio ellipsoids). However, these pores may be inter- or intra-granular, it is not possible to distinguish this from these thin-sections.

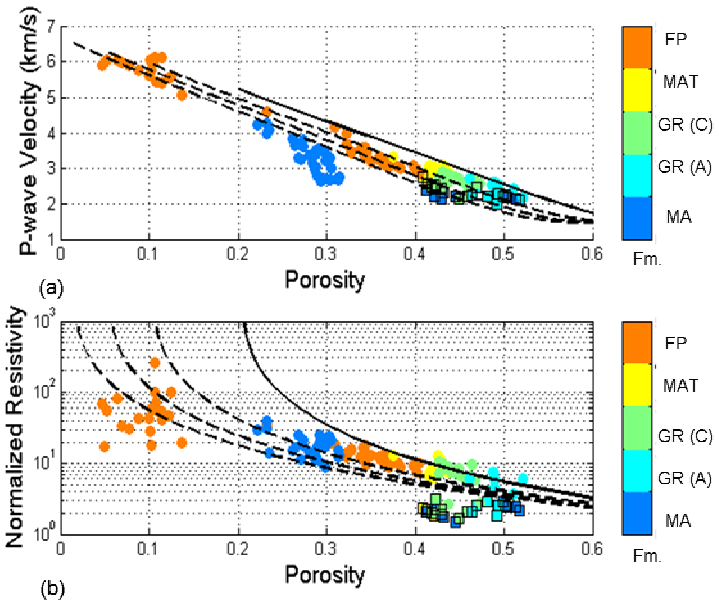

Figure 4.8: Modeling of velocity and normalized resistivity, assuming porous grains with pores of aspect ratio 0.5, using SC approximation. The pack of grains is modeled using SC assuming spherical grains, 60% needle-like pores and 40% ellipsoidal pores with aspect ratio 0.1. Squares are measurements from Carrara et al. (1999). The solid line is computed assuming an intra-granular porosity 0.2, and the dashed lines successively below it are for intra-granular porosities 0.1, 0.05 and 0.01, respectively. Porosity refers to the total porosity, including both intra- and inter-granular porosity.

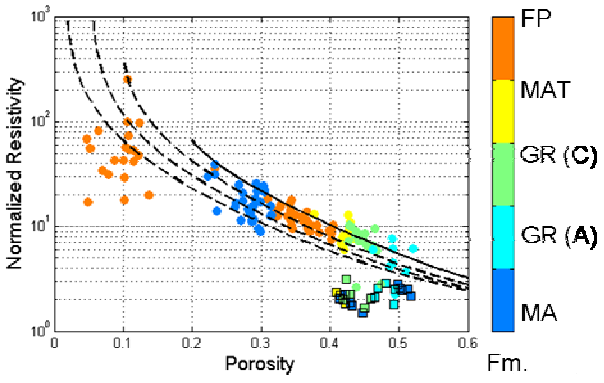

Figure 4.9: Same as Figure 4.8b, but using Archie's equation with *m*=2.6 to model the intragranular pores, instead of self-consistent model, based on Sen's (1997) approach.

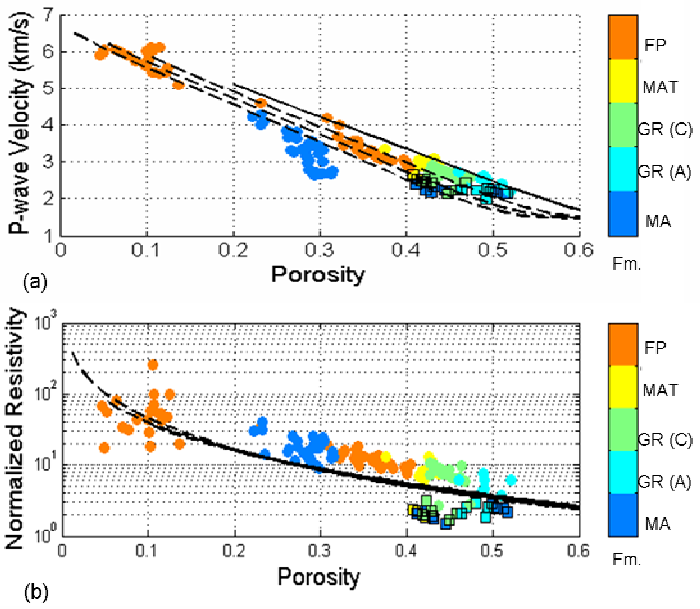

Figure 4.10: Same as Figure 4.8, but assuming intra-granular pores as needles.

Baechle et al. (2007) modeled velocity in a set of carbonate rocks with DEM using an aspect ratio 0.5 for the inter-granular pores (estimated from thin sections) and assuming intra-granular pores with 0.1 aspect ratio. Hence, Baechle et al. (2007) assume that these intra-granular pores are actually more compliant that the inter-granular pores, and are the pores which are responsible for lowering the velocity for rocks with the same total porosity. If we assume the intra-granular pores as ellipsoids with aspect ratio 0.1, and the inter-granular pores as 60% needles and 40% ellipsoids of aspect ratio 0.5 (Figure 4.13); then, as we increase intra-granular porosity, both P-wave velocity and normalized resistivity decrease, which is inconsistent with our previous observations. In our previous modeling, we included a fraction of low-aspect-ratio ellipsoidal inter-granular pores, which accounts for the lower velocity values

observed, due to the presence of compliant pores; but we assumed that the intra-granular pores are actually stiff or close to having circular cross-sections.

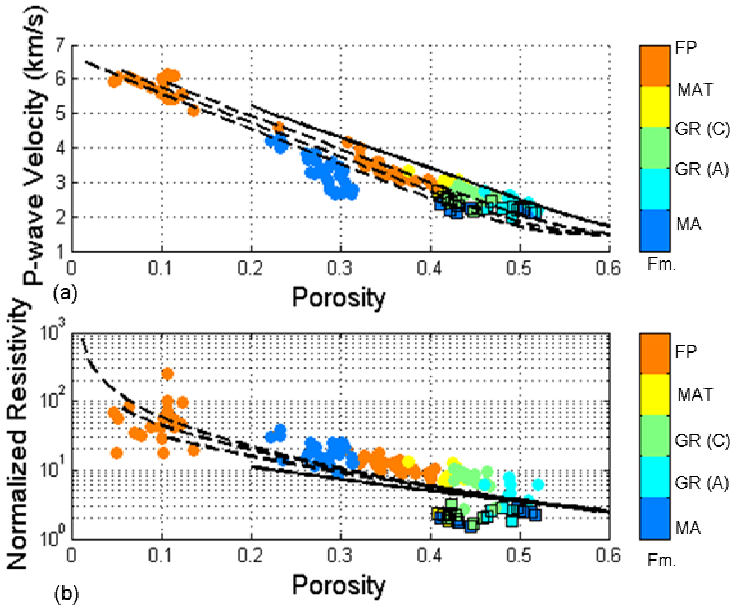

Figure 4.11: Same as Figure 4.8 but using Archie's equation (a=1, m=1.5) to model resistivity of intra-granular pores.

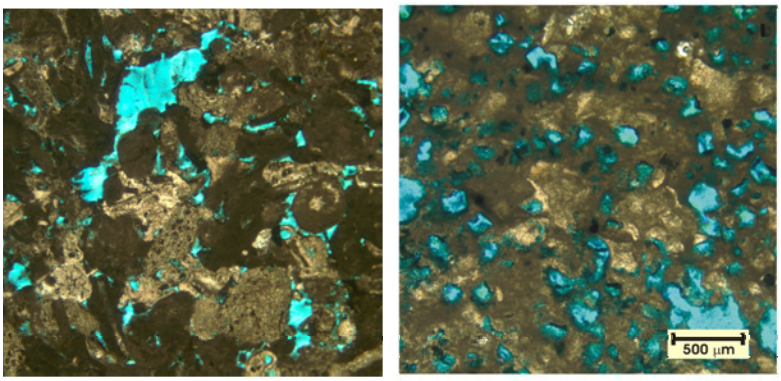

Figure 4.12: Both samples have 10% porosity. The sample on the left (B2) has P-wave velocity 5.55 km/s and normalized resistivity of 22.70; while the one on the right (A2) has P-wave velocity 6.21 km/s and normalized resistivity 17.46.

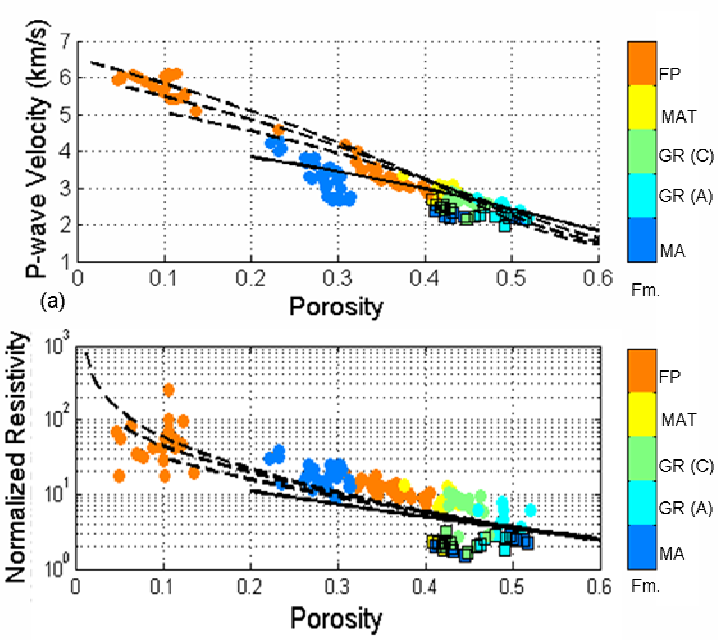

Figure 4.13: Same as Figure 4.11, but assuming porous grains with pores of aspect ratio 0.1 for the velocity. The pack of grains is modeled using SC assuming spherical grains, 60% needle-like pores and 40% ellipsoidal pores with aspect ratio 0.5.

Most of the samples under examination were composed of calcite; however, not all calcite grains have the same size. Some of the calcite was present in very fine grains, in the form of micritic cement. The resistivity measurements are not as strongly affected by this grain-size effect as the velocity measurements are (see blue data points corresponding to MA formation in Figure 4.11).

4.7 Permeability versus Porosity Relation

The permeability versus porosity relation for these samples is a very complex one, with a lot of scatter at low porosities (Figure 4.14). Resistivity is believed to be interrelated with permeability; however, it depends not only on porosity and permeability, but also on grain size, and pore geometry.

Permeability was modeled as a function of porosity using Kozeny-Carman's relation with tortuosity 1.5, a percolation porosity of 2%, and different grain sizes (500 to 10 micrometers), which were similar to those observed from the thin sections. As a result, we obtained a reasonable match for the high-porosity carbonates, but at lower porosities, there is still a lot of scatter, similar to what was observed for the resistivity measurements.

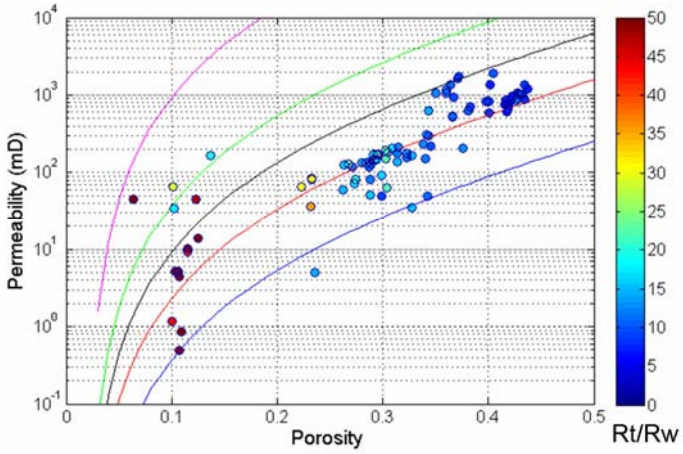

Figure 4.14: Permeability versus porosity, colorcoded by normalized resistivity. The curves correspond to Kozeny-Carman's equation for different grain sizes of 500, 100, 50, 25, and 10 μm, from the top line (magenta) to the bottom line (blue) line. The percolation porosity used in Kozeny-Carman's relation is 2%, and the tortuosity is 1.5.

4.8 Normalized Resistivity – P-wave Velocity Transform

Both P-wave velocity and resistivity depend strongly on porosity, and different relations to estimate P-wave velocity from normalized resistivity have been derived, such as those by Faust (1953) and Hacikoylu et al. (2006). If we plot P-wave velocity versus the logarithm of normalized resistivity for this dataset, and color-code the data points by porosity (Figure 4.15), we can observe a quadratic trend approximated by:

$$V_P \text{ (km/s)} = 0.99 (\log_{10}(Rt/Rw))^2 + 0.013 \log_{10}(Rt/Rw) + 2.1. \quad (4.2)$$

The velocity and resistivity values used to derive this relationship are those computed for a 100% water saturation, using Gassmann's and Archie's (Equation 4.1) expressions, respectively. As velocity increases, normalized resistivity also increases. Deviations towards lower velocities from the trend are due to different fractions of micrite present in the pore space. The micritic cement tends to affect the velocity but not the resistivity. Deviations towards lower resistivities from the trend correspond to the presence of water-saturated but stiff pores such as moldic or intra-granular pores, which causes high velocity but low resistivity values, as we discussed in the previous section.

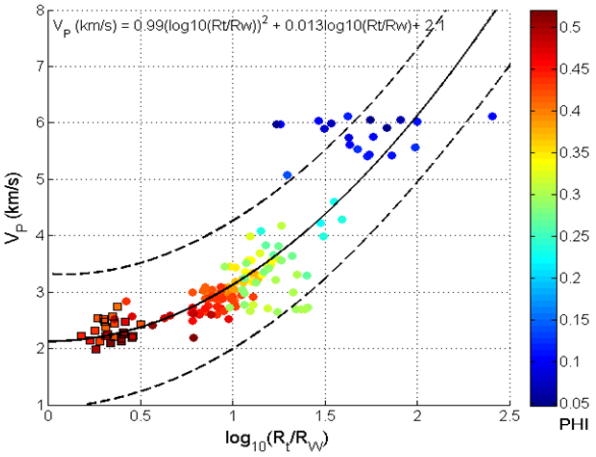

Figure 4.15: P-wave velocity versus the logarithm of normalized resistivity. Circles are measurements from this study. Open squares are measurements from Carrara et al. (1999). A quadratic fit is shown as a solid line, and +/- two standard deviation lines are shown as dashed lines. Data are color-coded by porosity.

4.9 Conclusions

We have shown that SC effective medium approximation is more appropriate than DEM for simultaneous modeling of both velocity and resistivity for carbonate rocks. To model both velocity and resistivity in a consistent manner for these carbonate rocks, stiff but well-connected pores (e.g., needle-like instead of ellipsoidal pores) are necessary. Also, the elastic response for this set of rocks can be modeled only if a fraction of compliant pores (e.g., ellipsoids with aspect ratio 0.1) is included in the modeling.

For almost all porosities, SC approximation is an appropriate modeling approach for both velocity and resistivity, and for both inter- and intra-granular porosity (modeled separately). For the low-porosity samples, SC provides satisfactory results if used to model inter-granular porosity, while intra-granular porosity is better modeled using SC effective medium for velocity, and using Archie's equation for resistivity. Semi-empirical models, such as Archie's equation and the stiff-sand model, also work to predict the velocity and resistivity of these samples.

Finally, a quadratic relationship between the logarithm of normalized resistivity and P-wave velocity is observed. Some deviations from this trend are due to calcitic micrite, and to pore stiffness effects on velocity that do not affect resistivity.

	XRD Mineralogy				
SAMPLE	**Calcite**	**Dolomite**	**Quartz**	**Porosity**	**HePorosity**
MA 1 a	-	-	-	0.30	0.30
MA 1 b	1.00	0.00	C.00	0.28	0.27
MA 1 c	-	-	-	0.30	0.30
MA 1 d	-	-	-	0.31	0.30
MA 2 a	-	-	-	0.29	0.28
MA 2 b	-	-	-	0.24	0.24
MA 2 c	1.00	0.00	C.00	0 29	0 29
MA 2 d	-	-	-	0.29	0.28
MA 3 a	-	-	-	0.29	0.29
MA 3 b	-	-	-	0.27	0.26
MA 3 c	-	-	-	0.28	0.27
MA 3 d	-	-	-	0.27	0.26
MA 4 a				0.31	0.30
MA 4 b	-	-	-	0.31	0.30
MA 4 c	-	-	-	0.32	0.31
MA 4 d	-	-	-	0.31	0.31
MA 5 a	-	-	-	0.24	0.23
MA 5 b	-	-	-	0.24	0.23
MA 5 c	1.00	0.00	C.00	0.22	0.22
MA 6 a	-	-	-	0.27	0.27
MA 6 d	1.00	0.00	C.00	0.28	0.27
MA 7 a	1.00	0.00	C.00	0.30	0.29
MA 7 c	-	-	-	0.30	0.29
MA 7 d	-	-	-	0.30	0.29
MA 8 a	1.00	0.00	C.00	0.30	0.29
MA 8 b	-	-	-	0.31	0.30
MA 8 c	-	-	-	0 33	0 31
MA 8 d	-	-	-	0.31	0.29
MA 9 a	1.00	0.00	C.00	0.29	0.29
MA 9 b	-	-	-	0.31	0.30
MA 9 d	1.00	0.00	C.00	0.29	0.29
A 105 a	-	-	-	0.51	0.51
A 105 b	-	-	-	0.49	0.49
A 105 c	-	-	-	0.49	0.49
A 105 d	1.00	0.00	C.00	0.46	0.46
A 177 a	-	-	-	0.52	0.52
A 177 b	-	-	-	0.49	0.49
A 177 c	-	-	-	0.49	0.49
A 177 d	-	-	-	0.40	0.40
C 105 a	-	-	-	0.47	0.47
C 105 b	-	-	-	0.45	0.45
C 105 c	-	-	-	0.47	0.47
C 105 d	-	-	-	0.46	0.46
C 179 a	-	-	-	0.45	0.45
C 179 b	1.00	0.00	C.00	0.46	0.46
C 179 c	-	-	-	0.44	0.44
C 179 d	-	-	-	0.44	0.44

Table 4.1: Mineralogy from X-Ray diffraction analysis performed by Cinzia Scotellaro at Stanford University, and MarcoVoltolini at the University of California at Berkeley. Porosity computed from mass, volume and mineralogy. Porosity measured with Helium porosimetry by Cinzia Scotellaro at Stanford University.

	XRD Mineralogy				
SAMPLE	**Calcite**	**Dolomite**	**Quartz**	**Porosity**	**HePorosity**
C 180 a	-	-	-	0.43	0.43
C 180 b	-	-	-	0.44	0.44
C 180 c	-	-	-	0.47	0.46
C 180 d	-	-	-	0.44	0.44
C 262 a	-	-	-	0.45	0.45
C 262 b	-	-	-	0.45	0.45
C 262 c	0.88	0.00	0.12	0.43	0.43
C 262 d	-	-	-	0.43	0.43
Nat 1 a	-	-	-	0.44	0.43
Nat 1 b	-	-	-	0.43	0.42
Nat 1 c	-	-	-	0.44	0.43
Nat 1 d	-	-	-	0.44	0.44
Nat 2 a	-	-	-	0.44	0.43
Nat 2 b	-	-	-	0.43	0.43
Nat 2 c	-	-	-	0.43	0.42
Nat 2 d	-	-	-	0.42	0.42
Nat 3 a	-	-	-	0.43	0.43
Nat 3 b	-	-	-	0.44	0.43
Nat 3 c	0.84	0.16	0.00	0.44	0.43
Nat 3 d	-	-	-	0.44	0.43
Nat 4 a	0.80	0.21	0.00	0.45	0.42
Nat 4 b	-	-	-	0.45	0.42
Nat 4 c	-	-	-	0.45	0.42
Nat 4 d	-	-	-	0.46	0.43
Nat 5 a	-	-	-	0.38	0.38
Nat 5 b	-	-	-	0.44	0.43
Nat 5 c	0.73	0.18	0.09	0.43	0.42
FP 1 a	-	-	-	0.11	0.11
FP 1 b	-	-	-	0.11	0.11
FP 1 c	-	-	-	0.12	0.12
FP 1 d	0.97	0.03	0.00	0.10	0.10
FP 2 a	-	-	-	0.07	0.07
FP 2 b	-	-	-	0.09	0.09
FP 2 c	-	-	-	0.10	0.10
FP 2 d	-	-	-	0.08	0.08
FP 4 a	-	-	-	0.35	0.34
FP 4 b	0.78	0.22	0.00	0.32	0.31
FP 4 c	-	-	-	0.33	0.32
FP 4 d	-	-	-	0.33	0.32
FP 5 a	-	-	-	0.39	0.38
FP 5 b	-	-	-	0.40	0.40
FP 5 c	-	-	-	0.40	0.40
FP 5 d	-	-	-	0.42	0.42
FP 6 a	-	-	-	0.37	0.37
FP 6 b	-	-	-	0.35	0.34
FP 6 c	-	-	-	0.38	0.38
FP 6 d	-	-	-	0.40	0.40

Table 4.2: Mineralogy from X-Ray diffraction analysis performed by Cinzia Scotellaro at Stanford University, and MarcoVoltolini at the University of California at Berkeley. Porosity computed from mass, volume and mineralogy. Porosity measured with Helium porosimetry by Cinzia Scotellaro at Stanford University.

	XRD Mineralogy				
SAMPLE	**Calcite**	**Dolomite**	**Quartz**	**Porosity**	**HePorosity**
FP 7 a	-	-	-	0.34	0.34
FP 7 b	0.90	0.10	0.00	0.34	0.34
FP 7 c	-	-	-	0.35	0.34
FP 7 d	-	-	-	0.34	0.34
FP 8 a	-	-	-	0.35	0.34
FP 8 b	-	-	-	0.34	0.33
FP 8 c	-	-	-	0.24	0.23
FP 8 d	-	-	-	0.34	0.33
FP 10 a	-	-	-	0.06	0.05
FP 10 b	-	-	-	0.05	0.05
FP 10 c	-	-	-	0.07	0.06
FP 10 d	-	-	-	0.06	0.05
FP 14 a	-	-	-	0.12	0.12
FP 15 a	-	-	-	0.14	0.14
FP 15 c	0.95	0.05	0.00	0.10	0.10
FP 15 d	-	-	-	0.10	0.10
FP 17 a	-	-	-	0.12	0.11
FP 17 b	0.84	0.16	0.00	0.12	0.11
FP 17 c	-	-	-	0.11	0.11
FP 17 d	-	-	-	0.13	0.12
FP 23 a	-	-	-	0.36	0.36
FP 23 c	-	-	-	0.41	0.40
FP 23 d	-	-	-	0.36	0.36
FP 24 a	-	-	-	0.37	0.36
FP 24 b	1.00	0.00	0.00	0.35	0.34
FP 24 c	-	-	-	0.37	0.37
FP 24 d	-	-	-	0.35	0.35
FP 25 a	-	-	-	0.37	0.37
FP 25 b	-	-	-	0.37	0.37
FP 25 c	-	-	-	0.40	0.40
FP 25 d	-	-	-	0.37	0.37

Table 4.3: Mineralogy from X-Ray diffraction analysis performed by Cinzia Scotellaro at Stanford University, and MarcoVoltolini at the University of California at Berkeley. Porosity computed from mass, volume and mineralogy. Porosity measured with Helium porosimetry by Cinzia Scotellaro at Stanford University.

SAMPLE	Perm (mD)	Sw	R (ohm m)	R/Rw	Vp dry (m/s)	Vs dry (m/s)
MA 1 a	49	0.91	196	5.86	3327	2001
MA 1 b	81	0.92	267	7.99	3510	2150
MA 1 c	93	0.94	242	7.61	3001	1871
MA 1 d	63	0.92	263	7.89	3162	1854
MA 2 a	135	0.91	211	6.25	2940	1589
MA 2 b	5	0.93	220	6.67	4010	2326
MA 2 c	52	0.96	202	6.64	3247	2023
MA 2 d	135	0.94	223	7.10	3150	1958
MA 3 a	82	0.91	198	5.92	3378	2084
MA 3 b	125	0.94	239	7.53	3529	2057
MA 3 c	71	0.94	256	8.12	3740	2269
MA 3 d	59	0.94	227	7.24	3753	2196
MA 4 a	182	0.94	289	9.03	2721	1694
MA 4 b	149	0.92	265	8.02	2273	1525
MA 4 c	213	0.92	182	5.49	2428	1461
MA 4 d	138	0.89	217	6.15	2339	1444
MA 5 a	84	0.90	357	10.32	3877	2299
MA 5 b	80	0.89	576	16.36	4258	2445
MA 5 c	66	0.91	426	12.68	4160	2427
MA 6 a	128	0.92	269	8.18	3061	1872
MA 6 d	117	0.93	203	6.32	2986	1938
MA 7 a	119	0.95	141	4.55	2751	1679
MA 7 c	169	0.97	255	8.48	2267	1408
MA 7 d	131	0.93	167	5.20	2378	1445
MA 8 a	138	0.89	201	5.71	2855	1672
MA 8 b	169	0.91	166	4.92	2312	1445
MA 8 c	177	0.89	197	5.51	2275	1442
MA 8 d	145	0.93	207	6.33	2190	1422
MA 9 a	170	0.85	292	7.53	3496	1811
MA 9 b	192	0.93	333	10.32	2274	1447
MA 9 d	148	0.93	334	10.44	2320	1429
A 105 a	-	0.87	64	1.75	2313	1352
A 105 b	-	0.89	96	2.71	2565	1680
A 105 c	-	0.88	43	1.17	2446	1526
A 105 d	-	0.88	103	2.88	2871	1807
A 177 a	-	0.88	95	2.60	1956	1222
A 177 b	-	0.90	103	2.97	2554	1482
A 177 c	-	0.90	85	2.44	2542	1535
A 177 d	-	0.91	71	2.09	2443	1492
C 105 a	-	0.85	50	1.28	2442	1516
C 105 b	-	0.87	116	3.16	2500	1496
C 105 c	-	0.84	106	2.68	2533	1517
C 105 d	-	0.86	108	2.87	2470	1613
C 179 a	-	0.88	114	3.16	2599	1610
C 179 b	-	0.88	118	3.28	2295	1545
C 179 c	-	0.89	122	3.48	2522	1501
C 179 d	-	0.88	35	1.00	2758	1638

Table 4.4: Permeability in millidarcies measured by Cinzia Scotellaro at Stanford University, water saturation reached for resistivity measurements, resistivity, normalized resistivity or formation factor computed using a saturation exponent (n) of 2, and Rw=28 ohm.m. P-wave and S-wave ultrasonic velocities measured at dry conditions by Cinzia Scotellaro at Stanford University.

SAMPLE	Perm (mD)	Sw	R (ohm m)	R/Rw	Vp dry (m/s)	Vs dry (m/s)
C 180 a	-	0.88	141	3.88	2814	1557
C 180 b	-	0.91	123	3.59	2434	1382
C 180 c	-	0.84	144	3.64	2367	1319
C 180 d	-	0.87	153	4.12	2865	1488
C 252 a	-	0.87	121	3.26	2848	1674
C 252 b	-	0.85	129	3.32	2806	1640
C 252 c	-	0.89	158	4.46	2862	1776
C 252 d	-	0.89	100	2.83	2474	1538
Mat 1 a	882	0.90	121	3.47	2771	1492
Mat 1 b	755	0.92	125	3.78	2897	1537
Mat 1 c	984	0.93	127	3.98	2817	1437
Mat 1 d	1184	0.92	111	3.33	2780	1421
Mat 2 a	1059	0.94	98	3.03	2798	1520
Mat 2 b	848	0.95	123	3.98	2774	1455
Mat 2 c	764	0.93	105	3.23	2856	1535
Mat 2 d	848	0.95	85	2.75	2973	1578
Mat 3 a	897	0.95	144	4.64	2837	1476
Mat 3 b	1056	0.95	145	4.63	2889	1449
Mat 3 c	1342	0.96	133	4.36	2834	1495
Mat 3 d	1038	0.95	123	3.97	2796	1514
Mat 4 a	853	0.96	103	3.40	2801	1483
Mat 4 b	757	0.96	129	4.21	2804	1505
Mat 4 c	615	0.96	113	3.69	2813	1626
Mat 4 d	1044	0.98	118	4.05	3106	1591
Mat 5 a	207	0.94	144	4.52	3222	1656
Mat 5 b	1054	0.91	128	3.72	2907	1485
Mat 5 c	970	0.92	112	3.37	2939	1516
FP 1 a	0	0.89	936	26.62	5399	2953
FP 1 b	1	0.89	760	21.62	5416	2938
FP 1 c	10	0.87	784	21.14	5398	2923
FP 1 d	1	0.85	756	19.45	5814	2982
FP 2 a	-	0.80	639	14.45	6002	3178
FP 2 b	-	0.90	628	17.98	5749	3077
FP 2 c	5	0.87	732	19.65	5793	3099
FP 2 d	-	0.87	536	14.43	5917	3156
FP 4 a	150	0.95	163	5.30	3546	2184
FP 4 b	205	0.90	243	7.10	4259	2428
FP 4 c	156	0.95	203	6.52	4069	2273
FP 4 d	179	0.98	202	6.92	3671	2253
FP 5 a	716	0.93	132	4.08	2927	1681
FP 5 b	825	0.93	120	3.74	3020	1734
FP 5 c	598	0.94	121	3.87	2901	1699
FP 5 d	644	0.92	115	3.47	2800	1612
FP 6 a	542	0.93	150	4.63	3165	1827
FP 6 b	297	0.93	175	5.46	3407	1971
FP 6 c	620	0.91	147	4.38	2955	1668
FP 6 d	840	0.94	135	4.23	2871	1657

Table 4.5: Permeability in millidarcies measured by Cinzia Scotellaro at Stanford University, water saturation reached for resistivity measurements, resistivity, normalized resistivity or formation factor computed using a saturation exponent (n) of 2, and Rw=28 ohm.m. P-wave and S-wave ultrasonic velocities measured at dry conditions by Cinzia Scotellaro at Stanford University.

SAMPLE	Perm (mD)	Sw	R (ohm m)	R/Rw	Vp dry (m/s)	Vs dry (m/s)
FP 7 a	231	0.93	231	7.17	3557	1977
FP 7 b	298	0.93	236	7.23	3575	2087
FP 7 c	220	0.92	127	3.81	3415	1983
FP 7 d	305	0.91	234	6.93	3565	1925
FP 8 a	49	0.94	161	5.05	3305	1882
FP 8 b	35	0.93	171	5.28	3430	1922
FP 8 c	37	0.91	434	12.92	4636	2613
FP 8 d	164	0.89	293	8.29	3401	1879
FP 10 a	-	0.86	893	23.87	6048	3123
FP 10 b	-	0.94	1043	32.57	5841	3115
FP 10 c	48	0.87	1488	40.65	6071	3184
FP 10 d	-	0.81	370	8.74	5932	3128
FP 14 a	46	0.84	893	22.70	5552	3112
FP 15 a	168	0.85	339	8.71	5078	2552
FP 15 c	65	0.77	635	13.48	6099	3292
FP 15 d	34	0.84	317	8.02	6038	3174
FP 17 a	5	0.76	4646	95.81	6218	3190
FP 17 b	9	0.77	824	17.46	6212	3293
FP 17 c	4	0.80	1846	42.22	6108	3181
FP 17 d	14	0.78	1837	39.95	5593	2973
FP 23 a	1054	0.92	174	5.30	3135	1960
FP 23 c	1905	0.87	151	4.12	2716	1691
FP 23 d	1164	0.90	156	4.48	3277	1974
FP 24 a	1344	0.92	186	5.58	3070	1919
FP 24 b	617	0.94	177	5.54	3235	1944
FP 24 c	1634	0.89	161	4.51	2927	1904
FP 24 d	1057	0.90	168	4.82	3097	1781
FP 25 a	931	0.89	175	5.01	2962	1908
FP 25 b	517	0.94	163	5.14	3172	1887
FP 25 c	1378	0.92	128	3.86	2867	1718
FP 25 d	1783	0.89	172	4.91	3127	1874

Table 4.6: Permeability in millidarcies measured by Cinzia Scotellaro at Stanford University, water saturation reached for resistivity measurements, resistivity, normalized resistivity or formation factor computed using a saturation exponent (n) of 2, and Rw=28 ohm.m. P-wave and S-wave ultrasonic velocities measured at dry conditions by Cinzia Scotellaro at Stanford University.

Chapter 5
CSEM Theoretical Background and Modeling

5.1 Abstract

Measuring resistivity using an electromagnetic field technology can be very useful to estimate saturation, which is hard to estimate from seismic data. In this Chapter, we review controlled source electromagnetic methods, and perform 3D finite element modeling, and compare this technique to seismic data. CSEM methods allow us to have an estimate of resistivity, and identify relatively thin resistors, although as we show from our modeling, their depth and lateral extent have an important impact on our ability to detect these reservoirs. Seismic resolution is not nearly as sensitive to the lateral extent and depth to the reservoir as CSEM data resolution is, but CSEM data does have the potential to distinguish between high and low gas saturated sandstones. As we show from seismic modeling, identifying low versus commercial gas saturated sandstones is not easy, since adding a small amount of gas can change the seismic response to be very close to that of a high gas saturated sandstones.

5.2 Introduction

Controlled source electromagnetic (CSEM) methods have become in the last five years a common tool to identify the depth and lateral location of resistive reservoirs (Chopra et al., 2007). Generally, water-saturated shale and sandstone have similar resistivity (1-2 ohm m), while hydrocarbon saturated sandstones have high resistivity (10 to several hundred ohm m). Therefore, these methods are sensitive to hydrocarbon saturation. Low porosity rocks may also show high resistivity, for example, evaporites, most igneous rocks, and also some carbonates. Almost all CSEM surveys are marine, but this method can also be used in land (Chopra et al., 2007). We will focus in understanding only marine CSEM technology, which is generally done in the frequency domain.

In general, if we compare the resistivity measurements from CSEM with those obtained from well logging, they can be very different. One of the main reasons is that we measure a total resistance or a weighted arithmetic average of resistivity (weighted by the thickness of the layer) when we use CSEM methods, and not each individual layer resistivity (Strack, 1992). Also, using conventional logging tools, we measure horizontal resistivity, similar to combining the layers as resistors in parallel, while CSEM technology gives us the vertical resistivity, equivalent to combining the layers as resistors in series.

In this chapter, we will introduce the theory behind CSEM methods, and we will use some simple models to compare its capabilities to characterize gas sandstones to

those of seismic reflection data. In particular, we will focus on studying its resolution and its ability to distinguish commercial and non-commercial gas saturation.

5.3 Theoretical Background

The source used for CSEM data acquisition is a horizontal electric dipole (HED) towed in a neutrally buoyant streamer (around 50 m above the seafloor) above an array of receivers deployed on the seafloor (Figure 5.1). The source sends a time-continuous periodic low-frequency (~0.01 – 10 Hz) electromagnetic signal (Chopra et al., 2007). Each individual frequency is transmitted one at a time (Anderson et al., 2008) (Figure 5.2).

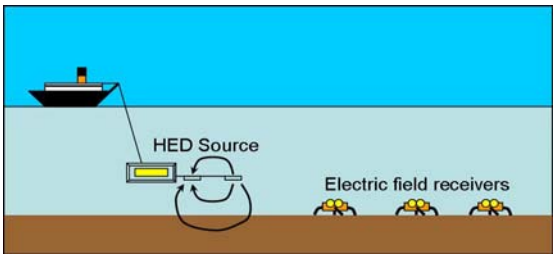

Figure 5.1: Schematic showing common configuration during CSEM surveys. HED source towed in a streamer above array of receivers.

A current is injected across the bipole electrodes of the source producing a primary electromagnetic field. This primary field induces currents in the subsurface and creates a secondary electromagnetic field. The total field includes both the primary and the secondary fields. The primary field is present during the recording, so it records the total field. The receivers record both amplitude and phase of the electric field parallel and perpendicular (inline or radial and crossline or azimuthal) to the

source orientation. The inline or radial electric field is the most commonly used in CSEM analysis.

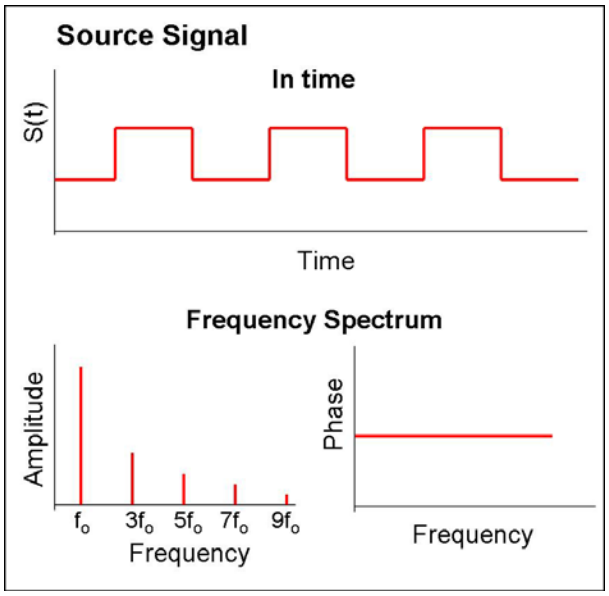

Figure 5.2: Schematic showing amplitude and phase of the source signal function for CSEM in time, and its frequency spectrum, including amplitude and phase.

Generally, a high-resistivity target is only detectable at offsets greater than about twice its depth (Anderson et al., 2008). At short offsets, the direct energy between source and receiver dominates over that diffusing through the subsurface. As the offset increases, we have a stronger signal from the energy that propagates through the subsurface. At larger offsets, the airwave effect (energy refracting along the sea-water interface) also becomes smaller. The airwave amplitude is larger as the water depth decreases (Johansen et al, 2007). This fact is what has limited CSEM technology to deep water (>~ 300 m).

CSEM data are commonly processed in the frequency domain (Chopra et al., 2007). The most common interpretation approaches for CSEM include plots of the normalized amplitudes of the electric field (magnitude, both inline and crossline) versus offset (known as MVO) at individual frequencies, and of normalized phase of the electric field versus offset (PVO) at individual frequencies. The amplitude and phase are normalized with respect to a reference receiver from an area that represents the background resistivity response (without the reservoir). The electric field magnitude is also sometimes given as the electric field at the receivers divided by the dipole source strength (antenna length times zero-to-peak transmission current).

The fundamental equations to describe the EM phenomenon are the Maxwell equations, which for linear media are:

$$\nabla \cdot \mathbf{E} = \frac{1}{\varepsilon} Q_f , \tag{5.1}$$

$$\nabla \cdot \mathbf{B} = 0 , \tag{5.2}$$

$$\nabla \times \mathbf{E} = -\frac{\partial \mathbf{B}}{\partial t} , \tag{5.3}$$

$$\nabla \times \mathbf{B} = \mu_0 \mathbf{j} + \mu_0 \varepsilon \frac{\partial \mathbf{E}}{\partial t} . \tag{5.4}$$

$\mathbf{E}$ is the electric field, $\mathbf{B}$ is the magnetic flux density, ε is the electric permittivity, Q_f is the charge density, t is time, and $\mathbf{j}$ is the current density (Andréis and MacGregor, 2008). Assuming no charge buildup, we have Q_f =0, and then Equation (5.1) becomes: $\nabla \cdot \mathbf{E} = 0$. Applying the curl to Equations (5.3) and (5.4), we obtain:

$$\nabla^2\mathbf{E} = \mu_0\varepsilon\frac{\partial^2\mathbf{E}}{\partial t^2} + \mu_0\frac{\partial\mathbf{j}}{\partial t} \quad , \tag{5.5}$$

The current density, **j**, includes that caused by the source dipole, $\mathbf{j}_s$, such that (Chave and Cox, 1982):

$$\mathbf{j} = \sigma\mathbf{E} + \mathbf{j}_s \tag{5.6}$$

Replacing (5.6) into (5.5), we have:

$$\nabla^2\mathbf{E} = \mu_0\varepsilon\frac{\partial^2\mathbf{E}}{\partial t^2} + \mu_0\sigma\frac{\partial\mathbf{E}}{\partial t} + \mu_0\frac{\partial\mathbf{j}_s}{\partial t}. \tag{5.7}$$

If a single Fourier component proportional to $e^{-i\omega t}$ is considered (t is time, and ω is angular frequency) (Chave and Cox, 1982), Equation (5.7) becomes:

$$\nabla^2\mathbf{E} = -(\mu_0\varepsilon\omega^2 + i\mu_0\sigma\omega)\mathbf{E} - i\omega\mu_0\mathbf{j}_s. \tag{5.8}$$

After some algebra, we have (Andréis and MacGregor, 2008):

$$\nabla^2\mathbf{E} + i\omega\mu_0(-i\varepsilon\omega + \sigma)\mathbf{E} = -i\omega\mu_0\mathbf{j}_s. \tag{5.9}$$

If $\varepsilon\omega << \sigma$, which it is true for low frequency, and in a high conductivity medium, Equation (5.9) simplifies to (Andréis and MacGregor, 2008):

$$\nabla^2\mathbf{E} + i\omega\mu_0\sigma\mathbf{E} = -i\omega\mu_0\mathbf{j}_s. \tag{5.10}$$

Solutions for this equation in 1D can be decomposed into two parts corresponding to two different modes of the electromagnetic field – transverse magnetic (TM) and transverse electric (TE) modes. Any electromagnetic field in a homogeneous material can be separated into these two modes with respect to an arbitrary direction in space (e.g., the vertical or depth). Each mode will satisfy Maxwell's equations independently (Chave and Cox, 1982).

The solution of equation (5.10) is an integral equation for each mode of each component of the resulting electric field and magnetic flux density (Andréis and MacGregor, 2008). Below, we show the radial electric field of an HED source at height *z'* above the seafloor calculated at a receiver lying at height *z* above the seafloor (*z'*>*z*):

$$E_r = E_r^{TM} + E_r^{TE},$$

$$E_r^{TM} = \frac{P\cos\theta}{4\pi\sigma_0}\int_0^\infty \beta_0\left(kJ_0(kr) - \frac{J_1(kr)}{r}\right)\frac{1}{1-R_{air}^{TM}R_L^{TM}}(-e^{-\beta_0(z'-z)} + R_L^{TM}e^{-\beta_0(z'+z)} + R_{air}^{TM}e^{\beta_0(z'+z)} - R_{air}^{TM}R_L^{TM}e^{\beta_0(z'-z)})dk,$$

$$E_r^{TE} = \frac{P\cos\theta}{4\pi\sigma_0}\int_0^\infty \frac{i\omega\mu_0\sigma_0 J_1(kr)}{r\beta_0}\frac{1}{1-R_{air}^{TE}R_L^{TE}}(e^{-\beta_0(z'-z)} + R_L^{TE}e^{-\beta_0(z'+z)} + R_{air}^{TE}e^{\beta_0(z'+z)} + R_{air}^{TE}R_L^{TE}e^{\beta_0(z'-z)})dk, \quad (5.11)$$

where *r* is the offset, θ is the azimuth (angle between dipole axis and a line joining source and receiver), *P* is the source dipole moment, σ_0 is the conductivity of seawater, *k* is the horizontal wavenumber, β_0 is the complex wavenumber in the sea, J_0 and J_1 are first- and second-order Bessel functions respectively. R_{air}^{TM} and R_{air}^{TE} are the reflection coefficients at the air-water interface for the TM and TE modes, respectively. Assuming air to be infinitely resistive, then R_{air}^{TM} =-1, and

$$R_{air}^{TE} = \frac{\beta_0 - k}{\beta_0 + k}, \quad (5.12)$$

so TE modes are the ones that primarily contribute to the airwave effect. R_L^{TM} and R_L^{TE} are the reflection coefficients that actually contain information about the earth. They are computed applying the boundary conditions for the field components recursively at each material boundary in the structure starting from the deepest layer.

See Andréis and MacGregor (2008) for the complete solutions. For the 1D case, the transverse electric (TE) mode consists of horizontal current loops (circling the vertical axis). Coupling between adjacent layers in this case is purely inductive, so there is no current flow across boundaries. The transverse magnetic (TM) consists of current loops in the plane of the vertical axis. Coupling between adjacent layers is both inductive and galvanic. TE modes disappear for the limit of zero frequency, while TM modes vanish for DC current (Chave and Cox, 1982; Andréis and MacGregor, 2008).

In general when we have a wave equation as (Griffiths, 1989):

$$\nabla^2 \mathbf{E} = \mu_0 \varepsilon \frac{\partial^2 \mathbf{E}}{\partial t^2} + \mu_0 \sigma \frac{\partial \mathbf{E}}{\partial t} \; ; \tag{5.13}$$

similar to Equation (5.5) but including in **E** not only the induced but the total electric field, one solution in 1D is a plane wave, given by:

$$\mathbf{E} = \mathbf{E_0} \cdot e^{i(kz - \omega t)} \tag{5.14}$$

where $\mathbf{E_0}$ is the initial electric field, *z* is the depth, and *k* is the complex wave number. Replacing (5.14) into (5.13), we have that: $k^2 = \mu_0 \varepsilon \omega^2 + i \mu_0 \sigma \omega$, so that $k = k_+ + i k_-$. When $\varepsilon \omega << \sigma$, we have that (Griffiths, 1989):

$$k_+ \cong k_- \cong \sqrt{\frac{\omega \sigma \mu_0}{2}} \, . \tag{5.15}$$

The decline in current density versus depth which dictates the resolution of these methods is known as the skin effect. The skin depth is a measure of the distance over which the current falls to 1/e of its original value, and it is given by (Griffiths, 1989):

$$\delta = \frac{1}{k_-}, \tag{5.16}$$

The skin depth is then from (5.15) and (5.16):

$$\delta = \sqrt{\frac{2}{\omega \mu_0 \sigma}}, \tag{5.17}$$

Replacing ω by $2\pi f$ (f is the frequency), the value of μ_0, and the conductivity by $1/\rho$ (ρ is the resistivity):

$$\delta = \sqrt{\frac{2\rho}{2\pi(4\pi \times 10^{-7}\ \mathrm{N \cdot A^{-2}})\, f}} \tag{5.18}$$

Evaluating this, we get: $\delta \approx 503 \text{meters} \sqrt{\frac{\rho}{f}}$.

From (5.14) through (5.16):

$$\mathbf{E} = \mathbf{E_0} \cdot e^{\frac{-z}{\delta}} e^{i(\frac{z}{\delta} - \omega t)}; \tag{5.19}$$

hence, the electric field will decay exponentially in a conductive medium with depth. When $\varepsilon\omega << \sigma$, we are on a diffusion regime, and the notion of "wavelength" loses its geometrical significance, and the wave only penetrates about a sixth of a wavelength ($\delta \cong \lambda / 2\pi$), attenuating before it completes a single cycle. The decay rate of the electric field increases with frequency as we observe from Equation (5.19). Therefore, the smallest the frequency, the skin depth is larger, hence the decay of the

field is smaller with depth if the frequency is low. The resolution of these methods will definitely suffer as we increase the depth of the target, as we can see from Equation (5.19). The resolution of these techniques is roughly as a first estimate 10% of the depth of the target (Strack, 1992).

5.4 CSEM versus Seismic Modeling as a function of Gas Saturation and Reservoir Thickness

To have a better understanding of CSEM data, we model a gas-sandstone reservoir embedded in fully-water saturated sandstone. The overburden is assumed to be shale. We performed a 3D-finite-element modeling, using Comsol Multi-Physics software. We define a sphere of 5 km radius as the computational domain. Five regions are defined in this sphere, corresponding to air, then seawater, shaly overburden, fully-water saturated sandstone, and sandstone reservoir. We defined the reservoir as a block of area 4 squared km (4km on the x-axis and 1 km on the y-axis), and 100 m thickness. We model the formation factor in the shale and sandstones using the relationships that we estimated at Nuggets-1 gas field, which is studied in more detail in Chapters 6 and 7. The formation factor assigned to shale is derived using Archie (1942) equation as:

$$F = \frac{1}{\phi^{2.6}}, \tag{5.20}$$

assuming porosity, ϕ=0.35 (similar to what is observed in the overburden for Nuggets-1 well log data). While, the formation factor assigned to sandstone is derived

from Archie' equation as well, but using Humble or Winsauer's expression (Schön, 1996):

$$F = \frac{0.62}{\phi^{2.15}} \quad , \tag{5.21}$$

using porosity, ϕ=0.32 as that from Nuggets-1 gas-sandstone reservoir (see Chapter 6).

Conductivities as observed in the model in Figure 5.3 were calculated as the inverse of the formation factor multiplied by water resistivity in this area. We assume 35,000 ppm salinity, therefore a water resistivity of around 0.1 ohm m. Water saturation in Figure 5.3a is assumed to be 0.1, while in Figure 5.3b is modeled as 0.9. We also show in Figure 5.3 the amplitude of the radial electric field in decibels at a frequency of 1 Hz for two different water saturations 0.1 and 0.9. Transmitter is modeled as a 10kA amplitude AC line current segment, 150 m above the seafloor (where the highest radial electric field magnitude occurs as observed in Figure 5.3). An outward radiating boundary condition is used on the sphere surface. These conditions follow the sea bed logging example as given in the RF and Microwave models in Comsol Multi-Physics software.

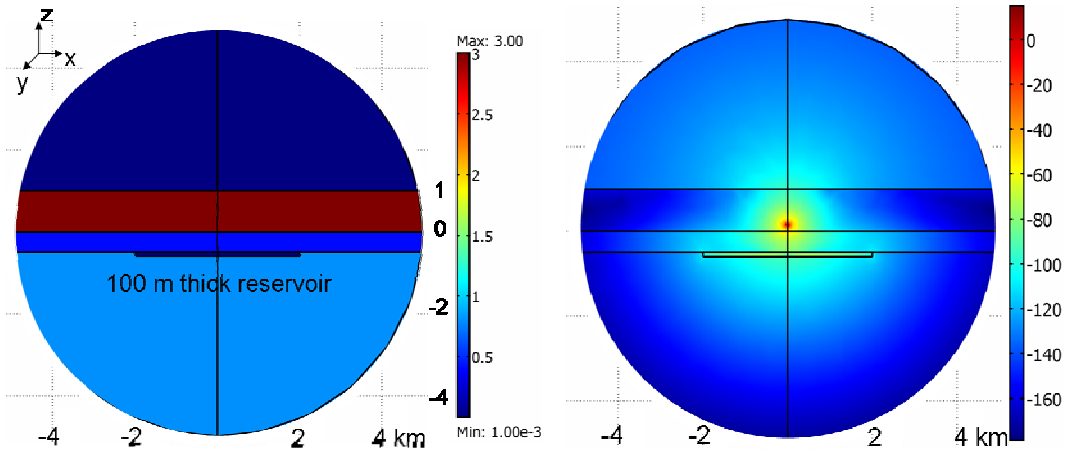

(a)

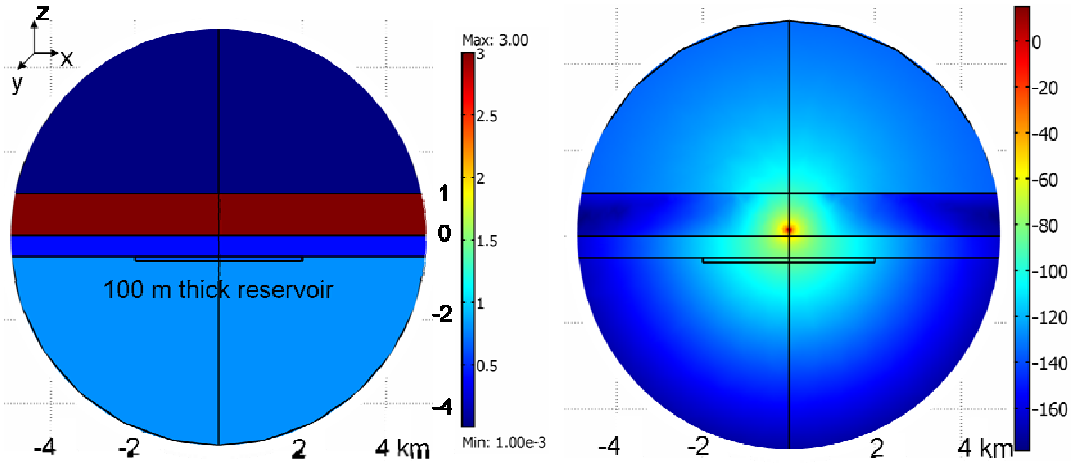

(b)

Figure 5.3: Reservoir model, xz view, colorcoded by conductivity on the left and by the magnitude of the radial electric field (dB) on the right. Top figures are for 10% water saturation, and bottom figures are for 90% water saturation, and both are for 1Hz frequency. The seawater layer is that with the highest conductivity (~3 S/m). Model space is a sphere with 5 km radius.

In the case of CSEM modeling, 1D versus 3D modeling can make a very big difference, due to the diffusion nature of the EM phenomenon at the frequencies of interest. For seismic modeling, 3D versus 1D modeling is important in the case of structural complex areas, but in the case of a simple model like the one we are working with, it does not make a big difference. We repeat the same modeling using

1D seismic modeling based on the convolutional model, but accounting for the effect of the Fresnel zone using horizontal averaging. Results are shown in Figure 5.4. The two seismic reflectors we observe are the top and bottom of the reservoir for two different water saturations, 0.1 and 0.9. The color scale for the amplitude was narrowed from -0.1 to 0.1 to be able to see any difference in the reflectors, but their amplitudes are actually very close in both cases.

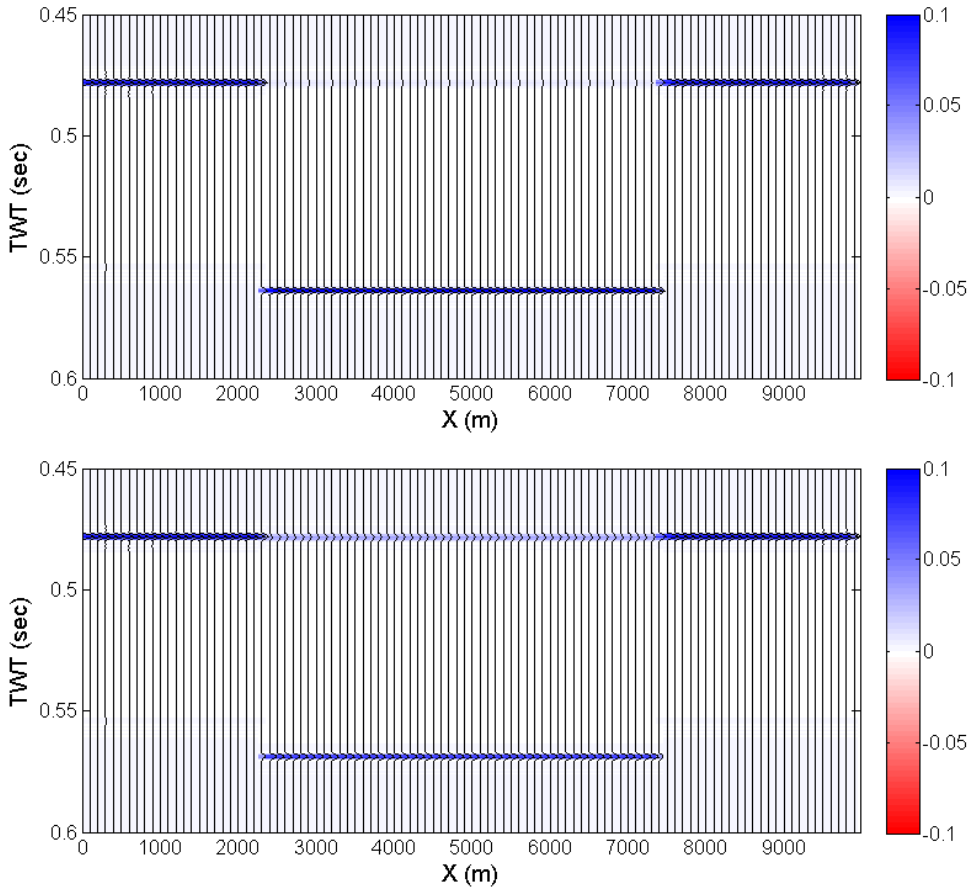

Figure 5.4: Stacked synthetic seismic sections for 50 Hz frequency colorcoded by seismic amplitude, reducing the color scale from -0.1 to 0.1 in order to observe the amplitude at the top of the reservoir. Top seismic section is for 10% water saturation, while bottom section is for 90% water saturation.

The difference in the magnitude of the radial electric field can be more easily observed in magnitude versus offset or MVO plots (Figure 5.5). In the same way, the difference in the seismic reflection amplitudes can be better distinguished in amplitude versus offset plots derived for the same model for the top of the reservoir (Figure 5.6).

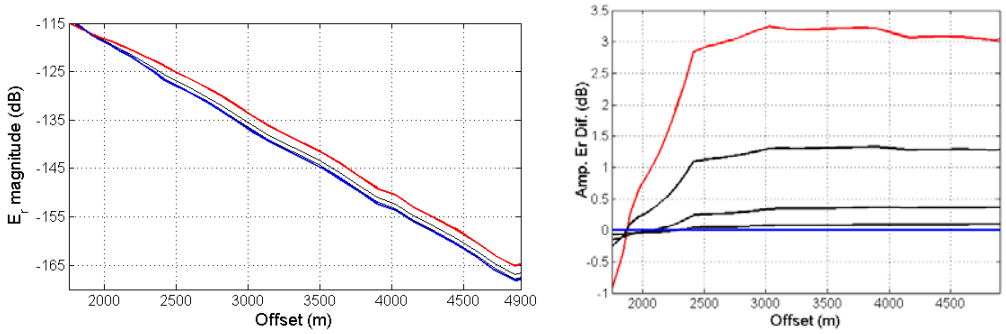

Figure 5.5: Radial electric field magnitude versus offset (MVO) curves on the left, and on the right the difference in radial electric field magnitude with respect to the 100% water saturated case. Blue curve is for 100% water saturation, red is for 10% water saturation, and three black curves in between are for 90, 70 and 40% water saturation.

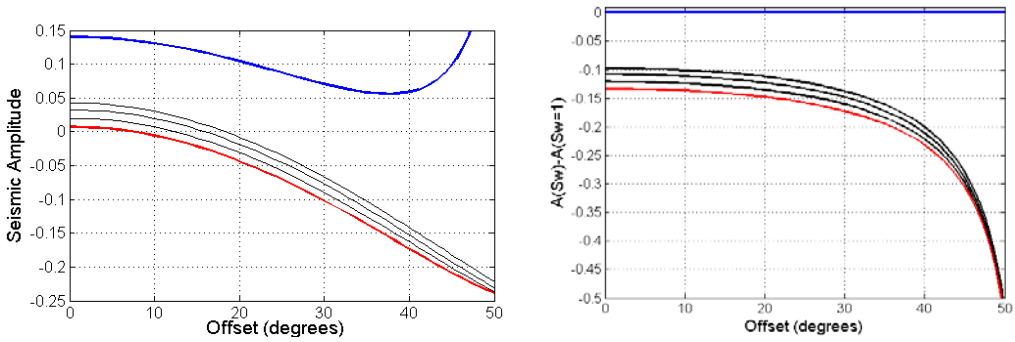

Figure 5.6: Seismic amplitude versus offset (AVO) curves on the left, and on the right the difference in seismic amplitude with respect to 100% water saturated case. Blue curve is for 100% water saturation, red is for 10% water saturation, and three black curves in between are for 90, 70 and 40% water saturation.

We observe that seismic amplitudes for 0.9 and 0.1 gas saturation are very similar, while the seismic amplitude for a fully water saturated sand is very different

from these two cases. On the other hand, the radial electric field amplitude versus offset is almost the same for 10 and 0% gas saturation, but it is very different in the case of 100% water saturation. Therefore, this explains the interest of the hydrocarbon industry in EM data, basically that CSEM data have more potential to identify a 90% gas saturated sand from a 10% gas saturated sand when compared to seismic data.

Acoustic impedance was computed using the rocks physics resistivity – acoustic impedance transforms derived in Chapters 6 and 7 for Nuggets-1 data, and shown in Figure 5.7, $\mathrm{AI\,(km/s\,g/cc)} = 2.3 \cdot \log_{10}(F) + 1.6$, for shale (model used in Chapter 7), and $\mathrm{AI\,(km/s\,g/cc)} = 3.9 \cdot \log_{10}(F) + 2.4$, for fully water-saturated sandstone (derived from models used to create acoustic impedance – resistivity template in Chapter 6). The shear-wave velocity data used in the modeling was obtained using the soft-sand model entering the parameters used to derive the transforms. The models used for the sandstone transform are the soft-sand model assuming 10% clay content, coordination number 13, critical porosity 0.4, effective pressure 20MPa, and Archie's equation with a=0.62 and m=2.15 (same parameters as in Chapter 6). For shales, we use soft-sand model for 60% clay content, coordination number 6, critical porosity 0.4 and effective pressure 20MPa, and Archie's equation with a=1, and m=2.6 (same parameters as in Chapter 7).

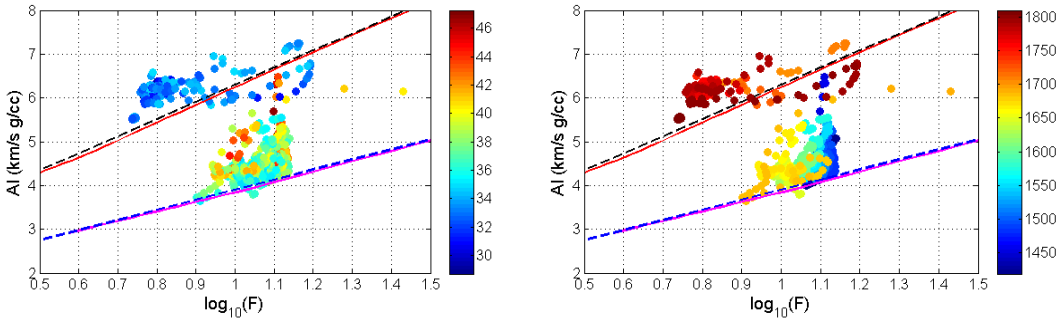

Figure 5.7: Soft sand-Archie impedance-resistivity models in red for sandstones and in magenta for shales. Data are from well in Nuggetts-1 field, colorcoded by gamma ray on left and depth (m) on right. Dashed lines are linear fits to the soft-sand-Archie models given by: $\mathrm{AI\,(km/s\,g/cc)} = 2.3 \cdot \log_{10}(F) + 1.6$, for shale, and $\mathrm{AI\,(km/s\,g/cc)} = 3.9 \cdot \log_{10}(F) + 2.4$, for sandstone.

Another important parameter is the thickness of the gas sandstone, since as described before, CSEM data responds to the total resistance. We changed the thickness of the sandstone from 100 m to 50 m and 25 m. The MVO curves for these three cases, and the base case with no reservoir are all shown in Figure 5.8. We observe that even for 25 m thickness, there is a separation from the base case, so the gas sand could be identified.

Further sensitivity analysis must include changing some of the horizontal dimensions of the reservoir, or the depth to the reservoir, which will both have very important effects as well, since they will affect the total resistance, which as we discussed before is the main property that the CSEM method measures. An important observation is that CSEM data could help identify the presence of the gas sand even if it was only 25 m thick, but it would not be possible to distinguish between a 25 and a 50 m thick sand. Hence, seismic data can help us better describe the geometry and thickness of the sandstone than the lower resolution EM data can.

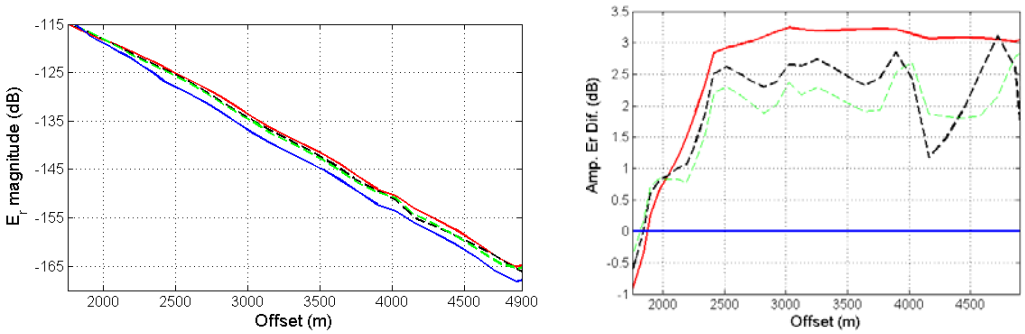

Figure 5.8: Radial electric field magnitude versus offset (MVO) curves on the left, and on the right the difference in radial electric field magnitude with respect to the 100% water saturated case. Blue curve is for 100% water saturation. The rest of the curves are for 10% water saturation, including red for 100 m thick gas sand, black for 50 m thick, and green for 25 m thick gas sand.

When we change the depth of the reservoir to 1 km, we notice that it is almost impossible to distinguish the reservoir from the background (compare blue and dashed red curved in Figure 5.9). This is expected since now one of the lateral dimensions of the reservoir is the same as its depth, and as Constable and Weiss (2006) show in their modeling, when the lateral dimensions of the reservoir become too small, CSEM data cannot identify it. We modify the dimensions to 4 by 2 km area, and 25 m thickness. In that case, at 1 km depth, as shown by the solid red line, we will have a better chance to identify the reservoir.

Lateral seismic resolution is described by the Fresnel zone, which radius (r) is given as a function of seismic velocity (v), normal incidence two-way traveltime ($t_0 = 2z/v$, where z is depth) and frequency (f) by (Yilmaz, 2001):

$$r = \frac{v}{2}\sqrt{\frac{t_0}{f}} \tag{5.22}$$

Evaluating this equation for $t_0 = 1$ s, v = 2000 m/s, f = 50 Hz, the radius is 141 m. Lateral seismic resolution decreases as depth increases (Yilmaz, 2001); however, it is not as dramatic as in the case of CSEM data, where the vertical currents generated by the source can only detect reservoirs that have a large lateral extent (large compared to their burial depth) (Constable and Weiss, 2006), although their thickness can be small, as we observed from our previous modeling.

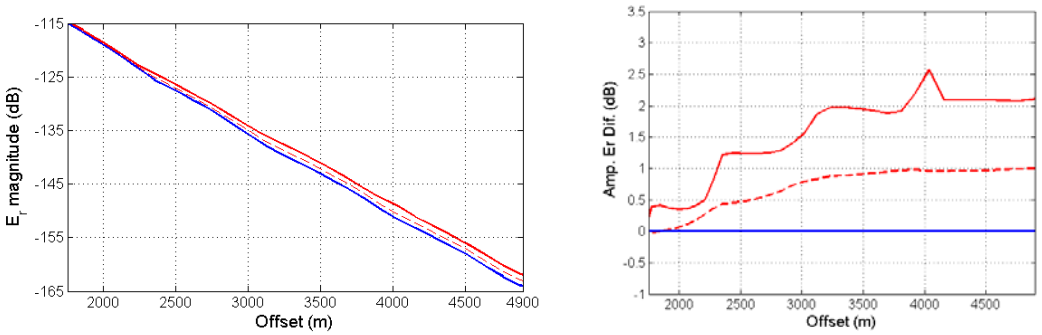

Figure 5.9: Radial electric field magnitude versus offset (MVO) curves changing the depth to the sandstone to 1000 m on the left, and on the right the difference in radial electric field magnitude with respect to the 100% water saturated case. Blue curve is for 100% water saturation. Red curves are for a 25 m thick gas sand, 10% water saturation. Solid red line is for 4x2 km² reservoir area, and dashed red is for 4x1 km² area.

Also, the orientation of the reservoir will have an important effect on what we can detect using CSEM data. If now we rotate the reservoir to be 2x4 km² and 1x4 km², hence, the longest dimension is perpendicular to the receiver line, we find that it is harder to detect it (Figure 5.10). Therefore, the smaller the reservoir is on the inline direction, the harder is to detect it.

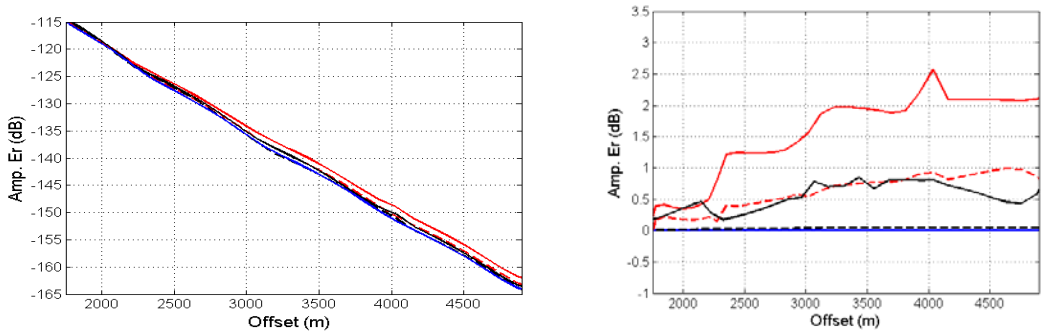

Figure 5.10: Radial electric field magnitude versus offset (MVO) curves on the left, and on the right the difference in radial electric field magnitude with respect to the 100% water saturated case. Blue curve is for 100% water saturation. Red and black curves are for a 25 m thick gas sand, 10% water saturation. Solid red and black lines are for 4x2 and 2x4 km² reservoir area, respectively. Dashed red and black lines are for 4x1 and 1x4 km² area.

5.5 Conclusions

From our modeling, we observe that CSEM technology can allow to identify commercial from non-commercial gas saturation in sandstones, particularly in the case where it is harder using seismic data. However, seismic data can help to better describe the geometry and thickness of a reservoir. CSEM data are more sensitive to the lateral extent and depth of burial of the reservoir compared to seismic data.

Another parameter that is extremely important for CSEM methods is the skin depth, which is a function of resistivity and frequency, as we learned in our theory review. We used a 1 Hz frequency in our modeling and an overburden resistivity of 2.5 ohm m, therefore, the skin depth is 795 m. That is another reason why as we bury our reservoir deeper to 1km, it becomes harder to identify, since the electric field magnitude has already decayed by 1/e by the time it reaches this depth.

Modeling CSEM data can help to identify in which cases using this technology will be useful. From the modeling, we found that if the reservoir is not laterally

extensive, in particular in the inline direction, it is harder to detect it. The reservoir thickness is important, but definitely its lateral dimensions in relation to its depth have a more important effect on our ability to detect the reservoir. As we observed from the analysis, seismic method will still be the most reliable method to delineate a reservoir, due to the lower resolution of CSEM data; however, we also show how CSEM can be very valuable to identify commercial versus non-commercial gas saturation.

Chapter 6
Case Study using Rock Physics Impedance–Resistivity Templates: Nuggets-1, North Sea

6.1 Abstract

Combining electromagnetic and seismic field data can improve estimates of reservoir properties and conditions. In this chapter, we show a case study in the North Sea, where we describe and apply the methodology we are proposing to estimate porosity and saturation from acoustic impedance and resistivity field-scale measurements.

We first use rock-physics diagnostics to predict which elastic and resistivity model is appropriate in a given area or reservoir. Using this model, we compute acoustic impedance and resistivity for a given porosity or saturation to generate the rock-physics impedance – resistivity templates at the well-log scale. Once these templates have been created at the well scale, Backus and arithmetic averages can be used to upscale the acoustic impedance and the resistivity, respectively. In this way, we can

generate an upscaled template, which can be used with field data. This allows us to estimate saturation and porosity from field data. Other seismic attributes can be used to create these templates, such as elastic impedance or seismic velocity.

6.2 Introduction

Chapter 2 introduced the concept of templates at the well-log scale and the concept of upscaling to field seismic and EM data. In this chapter, we apply these concepts to a field data set, and we show how to upscale acoustic impedance–resistivity templates, which can then be used to estimate porosity and saturation from field data.

As we discussed in Chapter 2, Ødegaard and Avseth (2003) introduced the term rock physics template (RPT). An RPT is a chart of locally constrained rock physics models for prediction of lithology and hydrocarbons (Avseth et al., 2005). In general, these charts are crossplots of acoustic impedance versus Vp/Vs ratio, or of other seismic attributes. The charts or templates, which we have created of P-wave impedance and resistivity, are also made of locally constrained models. As we discussed above, they can be upscaled, but previous knowledge of lithology and pore fluid properties are required to create them. We can obtain this information if we have some well control.

The data set that we use is from the Nuggets-1 gas field. This field is located in the North Sea, offshore from the UK in 115 m of water. The sand reservoir belongs to the Eocene Frigg formation and is about 25 m thick (Harris and MacGregor, 2006). Figure 6.1 shows gamma ray, neutron porosity, resistivity, density and sonic well logs from a well located in this field. At about 1690 m depth, we can observe the reservoir

gas sand, where we will show the application of our combined interpretation technique.

6.3 Rock Physics Diagnostics

First, we use the well-log velocity and porosity data to diagnose this reservoir. This diagnosis includes three steps: (1) bring the entire interval to the "common fluid denominator" by theoretically making it all wet (fluid substitution from gas to formation water); (2) plot the resulting acoustic impedance-porosity data for sand and shale; and (3) superimpose theoretical acoustic impedance-porosity curves upon this plot to find which model describes the trends best. Here, we find that the constant-cement–sand model (Avseth et al., 2000) is most appropriate for this specific example (Figure 6.2). This model is consistent with this formation's age (Eocene, the earliest of the three divisions of the Tertiary period); therefore, we expected that it could be a cemented sand.

The resistivity is modeled using a version of Archie's formula (Archie, 1942) known as the Humble or Winsauer equation (Winsauer et al., 1952), which assumes the Archie's constants $a = 0.62$ and $m = 2.15$ (Figure 6.3). The Winsauer equation was derived for approximately thirty brine-saturated sandstone samples, with ages ranging between Devonian and Pliocene, from different locations in North America. The area under study also corresponds to brine-saturated sandstones. The water salinity is 35,000 ppm, which gives R_w about 0.1 ohm·m, using the Schlumberger Gen-6 chart.

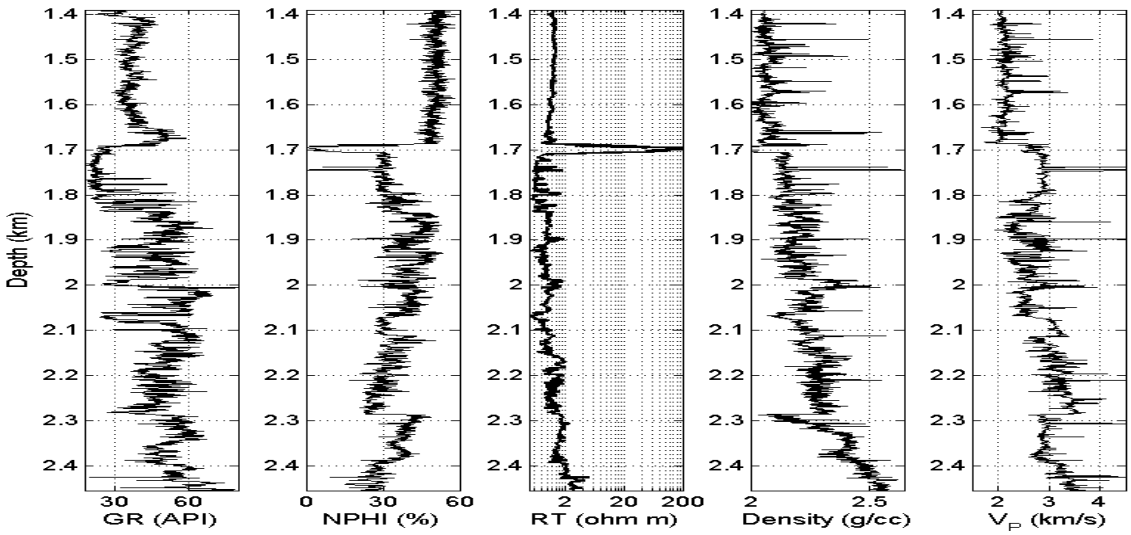

Figure 6.1: Well logs at Nuggett-1, from left to right: gamma ray (GR), neutron porosity (NPHI), deep resistivity (RT), density and sonic velocity (V_P).

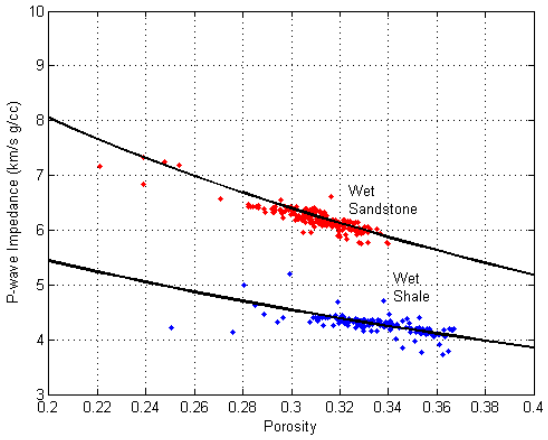

Figure 6.2: Rock physics diagnostics. Acoustic impedance versus porosity for sand and shale in the Nuggets well. The impedance is for 100% water-saturated rock obtained from the original log data by theoretically substituting formation water for gas in the reservoir. The upper curve is the constant-cement model for 100% quartz, whereas the lower curve is for 100% clay.

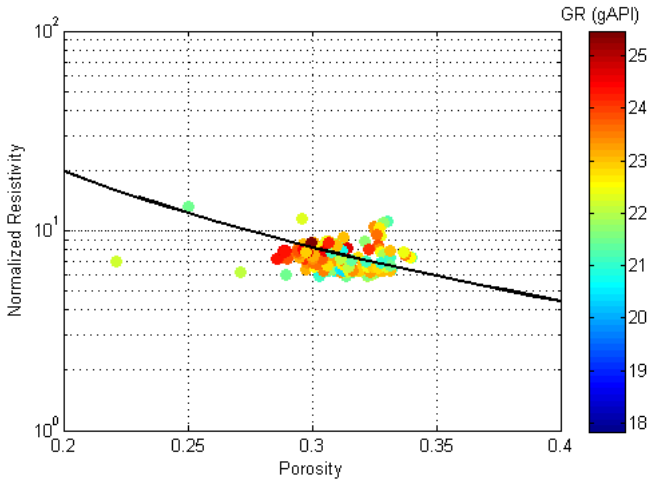

Figure 6.3: Rock physics diagnostics. Normalized resistivity (Rt/Rw) versus porosity for sand in the Nuggets well color-coded by gamma ray. The data points are for 100% water-saturated rock obtained from the original log data by theoretically substituting gas in the reservoir with the formation water, assuming a saturation exponent of 2. The curve is the Humble or Winsauer equation (Schön, 1996), which assumes the Archie constants $a = 0.62$ and $m = 2.15$.

6.4 Rock Physics Acoustic Impedance–Resistivity Templates

Once we have performed rock-physics diagnostics using the well-log data, we can combine these models to create an acoustic impedance–resistivity template at the well-log scale. As was explained in Chapter 2, both models are recreated in a porosity range from 0.15 to 0.4, and saturation is changed from zero to one at each porosity station to generate the vertical lines in the template. Then saturation is kept constant, while porosity is changed from 0.15 to 0.4, which gives rise to the horizontal lines shown in the template. In both cases, the models interpreted during the rock physics diagnostics are used to generate the template.

The resulting I_p-versus-R template at the well-log scale (see Figure 6.4, left) gives the sand's porosity at about 0.3 and gas saturation up to 0.9. This template should not be used directly with field seismic and CSEM data, whose scales of

measurement are vastly different from those in the well and also different from each other (Figure 6.5). This template must be altered to honor the statistics of the data, which varies with the scale of measurement.

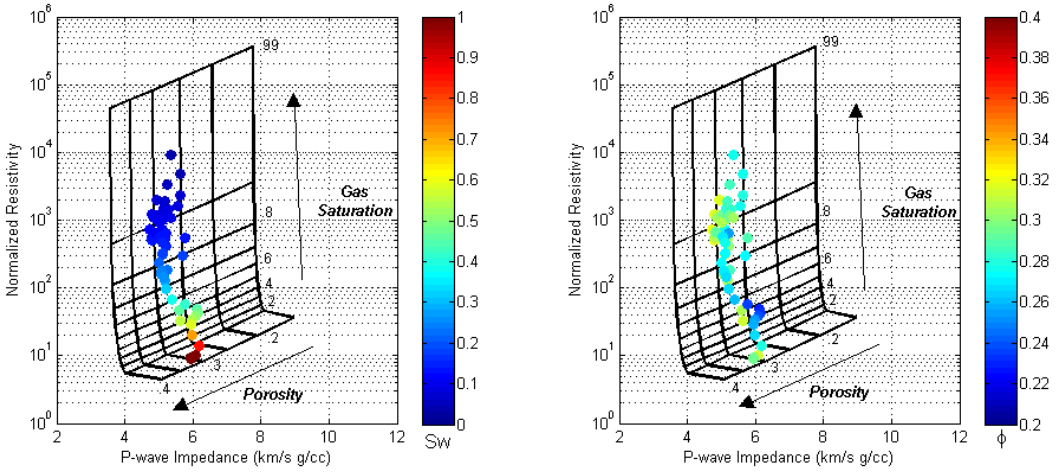

Figure 6.4: Acoustic impedance-resistivity template for the Nuggets reservoir with log data superimposed. Color bars are water saturation (left) and porosity (right).

To conduct such upscaling, let us remember that seismic and CSEM profiling simultaneously provide us with two values for a single location in the subsurface. What reservoir properties may generate these two responses? One approach to answering this question is forward modeling. We assume that the thickness of the gas and wet sand layers as well as the properties of the shale surrounding this sand are the same everywhere as at the well. Next, we create a pseudo-earth (or pseudo-well) model, as shown in Figure 6.6, where the acoustic impedance in the shale is about 4.5 km/s g/cc, similar to the original well. Then we vary the porosity in the entire sand from 0.15 to 0.40 with a 0.05 step, and for each porosity, we vary the water saturation

in the gas sand from zero to one with a 0.01 step. This procedure produces a table of porosity and saturation at the scale of the pseudo-well.

From this table, we calculate (a) the acoustic impedance using the constant-cement–sand model and (b) the resistivity for each realization using the Winsauer equation (as described earlier in the text). One such realization is shown in Figure 6.6.

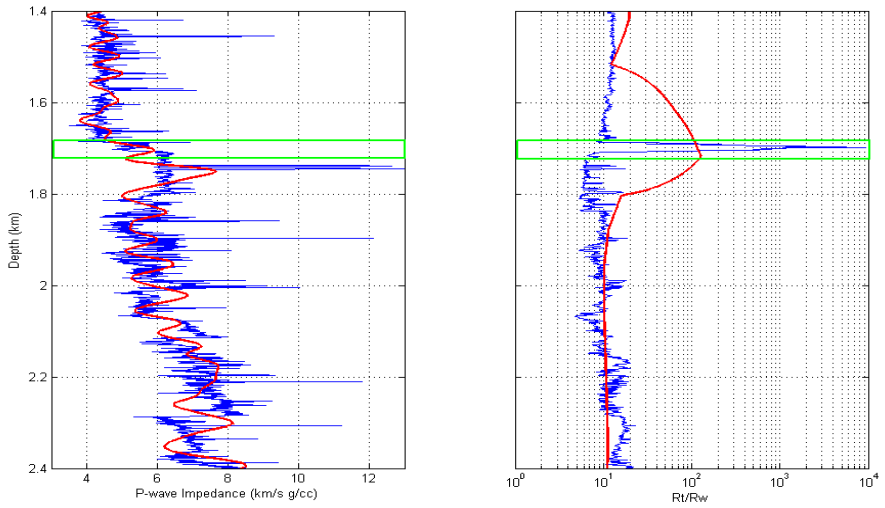

Figure 6.5: Nuggets gas field well log (blue) and seismic/CSEM (red) data at the well. The full seismic stack was provided by TGS-NOPEC, from which we obtained the seismic acoustic impedance using the Hampson-Russell inversion package. The CSEM resistivity profile was provided by OHM. The reservoir zone is highlighted in green.

For upscaling, we use the Backus average with a 12.5 m running window (about a quarter wavelength) to transform the log-scale acoustic impedance to the seismic-scale acoustic impedance and the arithmetic average with a 150 m running window (about 10% of depth to reservoir) to transform the log-scale resistivity to the CSEM-scale resistivity. The latter window (150 m) was selected to honor the difference between the resistivity at the reservoir as recorded by logging and CSEM. The upscaled

acoustic impedance and resistivity profiles are shown in Figure 6.5. We select those upscaled values in the middle of the reservoir for each realization and create an R_t / R_w-versus-I_p mesh that yields a template usable at the field scale (Figure 6.7).

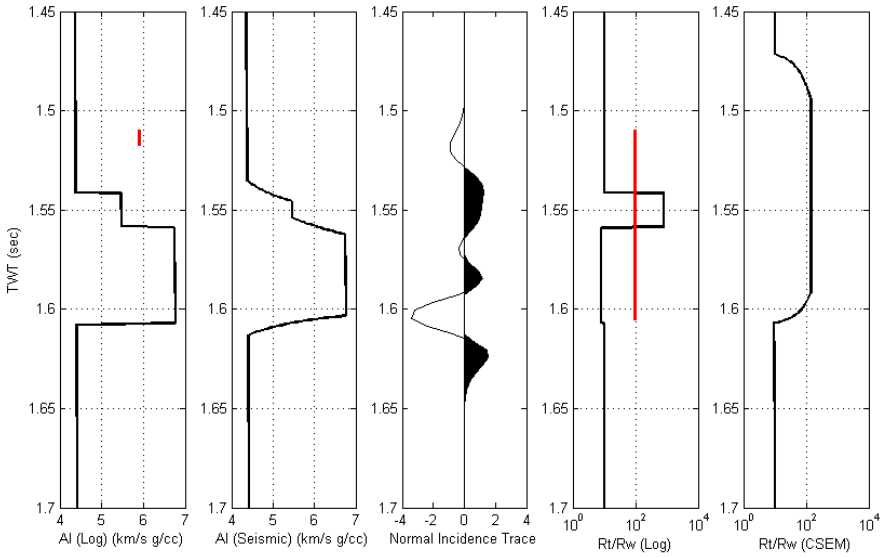

Figure 6.6: One realization of a pseudo-well. From left to right: log-scale acoustic impedance; seismic-scale acoustic impedance; a synthetic normal-incidence trace; log-scale resistivity; and CSEM-scale resistivity versus the two-way travel time. Red vertical bars show the upscaling windows for the acoustic impedance (first frame) and resistivity (fourth frame).

To interpret the Nuggets field data for porosity and saturation, we take the seismically-derived acoustic impedance and CSEM resistivity selected from the depth interval around the reservoir. These values are placed upon the field-scale template in Figure 6.7. The contour lines in this template indicate that the gas saturation is around 0.85 and porosity is around 0.25, consistent with the actual values in Nuggets.

For this particular case study, neither dipole log nor pre-stack data were available; however, we did generate a synthetic elastic impedance (also called far-offset impedance) log using the constant cement model and computed the range of the far-

offset impedance, which then served to build the template of elastic impedance versus acoustic impedance. This template was built in exactly the same fashion as the acoustic impedance–resistivity template, by varying only the porosity and saturation in the sand (Figure 6.8). The far-offset impedance in this case was calculated according to Connolly (1999), for an incidence angle of 30 degrees. We observe that this template does help discriminate gas- from water-saturated sand (Figure 6.8, left), although quantifying saturation is not possible, and intervals with low gas saturation can be confused with highly gas-saturated sand. Still, this template is useful for verifying that gas sands are being correctly identified. Also, from Figure 6.8 (right), we see that this template helps discriminate the low-porosity from the high-porosity intervals.

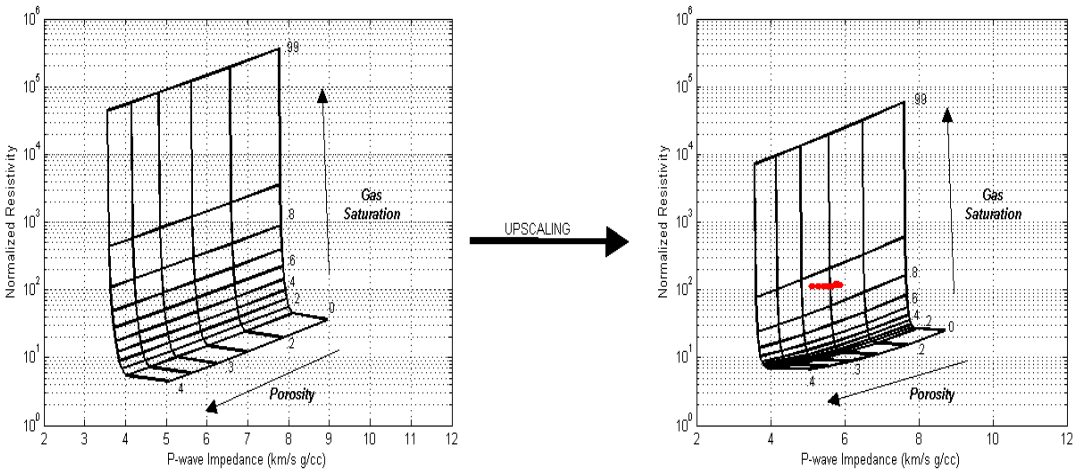

Figure 6.7: Left: a log-scale acoustic impedance-resistivity template, same as in Figure 6.4. Right: seismic/CSEM-scale template. The symbols are from the seismic acoustic impedance and CSEM resistivity profiles shown in Figure 6.5, selected at the reservoir.

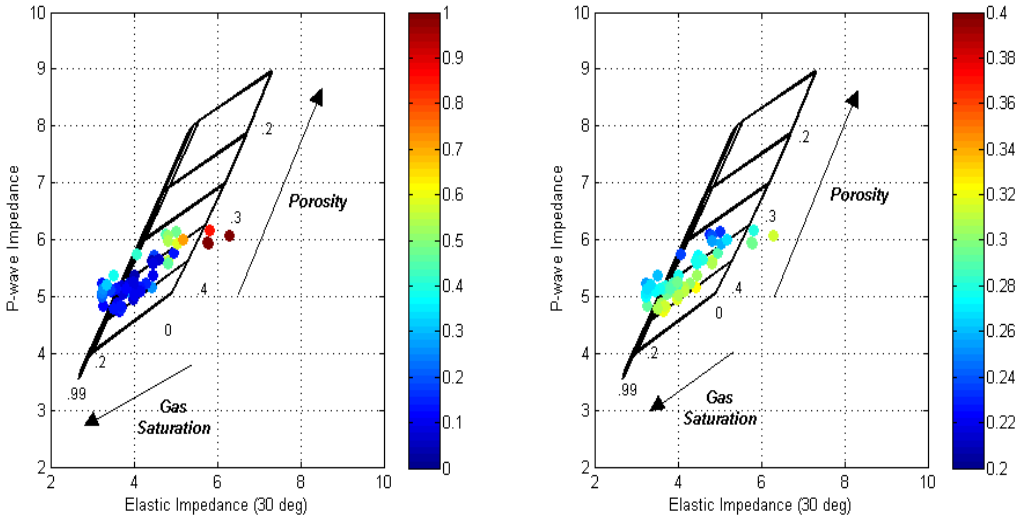

Figure 6.8: Acoustic impedance versus far-offset (30 degrees) impedance template for the Nuggets reservoir with log data superimposed. Color code is water saturation (left) and porosity (right).

Another seismic attribute that could help discriminate gas saturation is P-to-S elastic impedance according to Gonzalez et al. (2003). We plot this P-to-S elastic impedance for a 50 degree incidence angle versus that for a 10 degree incidence angle (Figure 6.9), as initially suggested by Gonzalez et al. (2003), and we observe that this template can robustly discriminate gas-sandstones from water-saturated sandstones but fails to discriminate saturation variations.

If we build templates for normalized resistivity versus far-offset impedance at 30 degrees offset, as shown in Figure 6.10, we observe that the far-offset impedance helps predict porosity for the intervals with gas saturation lower than 0.5, but as gas saturation becomes higher, the template using resistivity versus the acoustic impedance is definitely more sensitive to porosity and therefore is the best approach to predict porosity and saturation.

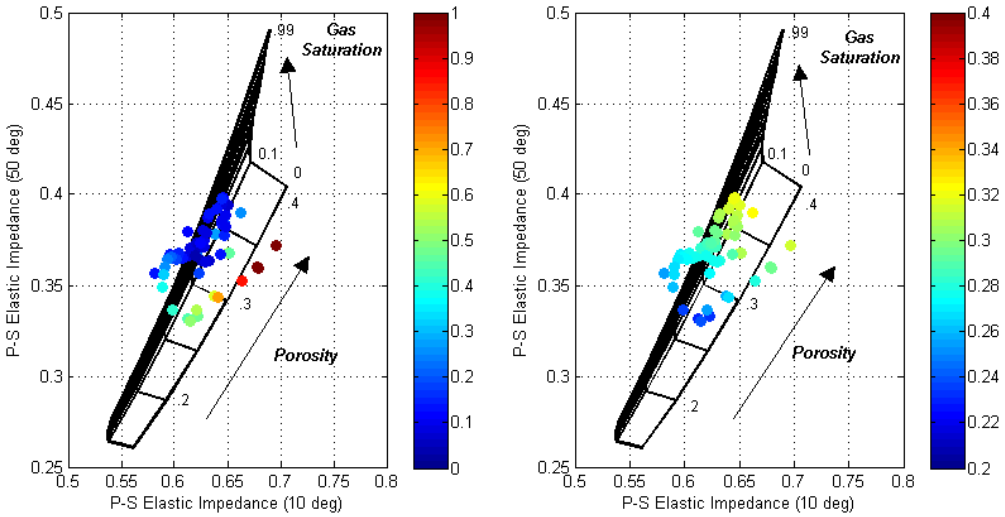

Figure 6.9: P-S elastic impedance (50 degrees) – P-S elastic impedance (10 degrees) template for the Nuggets reservoir with log data superimposed. Color code is water saturation (left) and porosity (right).

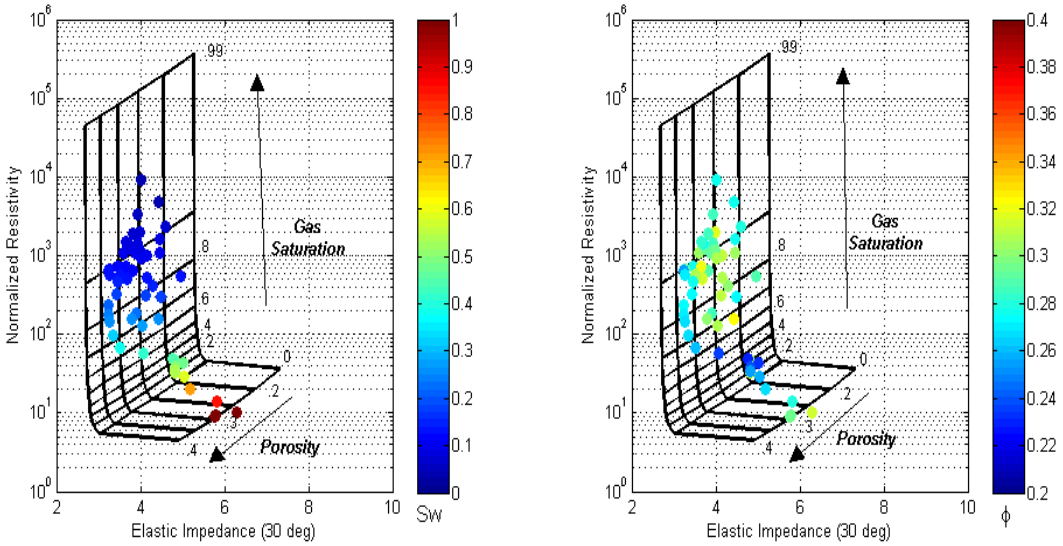

Figure 6.10: Far-offset impedance-resistivity template for the Nuggets reservoir with log data superimposed. Color code is water saturation (left) and porosity (right).

If we upscale the far-offset impedance template (Figure 6.11), we can still obtain similar estimates of porosity and gas saturation (around 0.25 and 0.85, respectively) as those found using the normalized resistivity – acoustic impedance templates. Far-offset impedance can help discriminate gas-saturated from water-saturated sand, but it is definitely not as sensitive to porosity as is acoustic impedance, particularly as gas saturation increases. At high gas saturations, the gas effect seems to dominate the response and cause a lot of scatter along the mean value of the sand porosity (around 0.25).

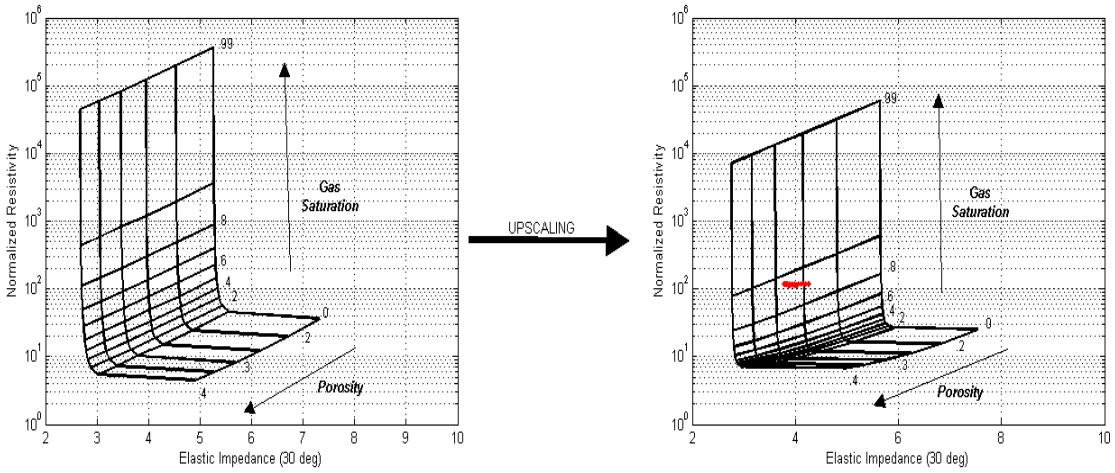

Figure 6.11: Left: a log-scale far-offset impedance-resistivity template, same as in Figure 6.10. Right: seismic/CSEM-scale template. The symbols are from the seismic far-ofsset impedance and CSEM resistivity profiles, selected at the reservoir.

Another option is to use P- and S-wave velocities combined with normalized resistivity to produce similar templates to estimate porosity and saturation (Figures 6.12 and 6.13). Upscaling the velocities with the Backus average as well, we realize that using seismic velocities together with normalized resistivity could also be a

reasonable choice (see Figures 6.14 and 6.15). Still, using the seismically-derived acoustic impedance is preferable in practice, because it usually has better spatial resolution than the seismic velocity.

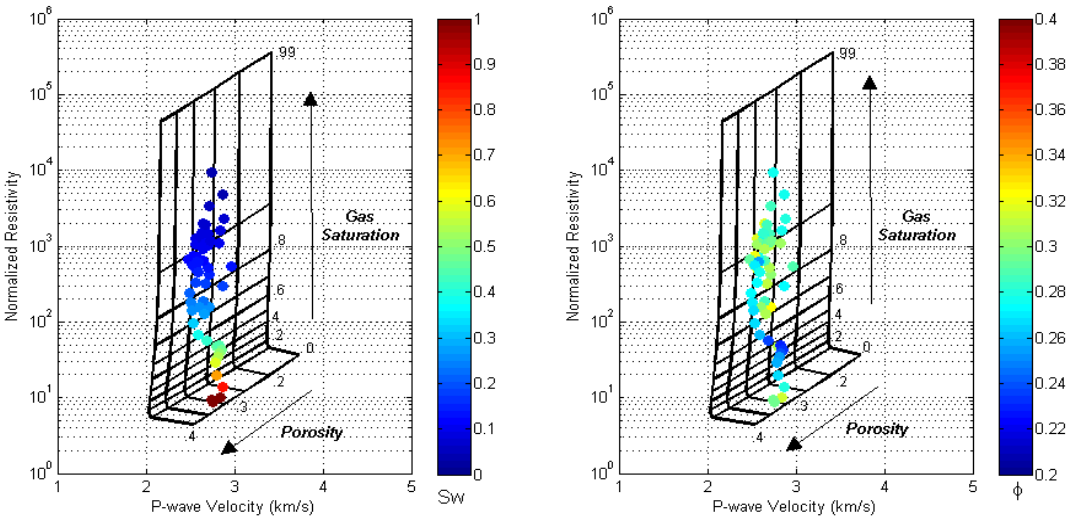

Figure 6.12: P-wave velocity-resistivity template for the Nuggets reservoir with log data superimposed. Color code is water saturation (left) and porosity (right).

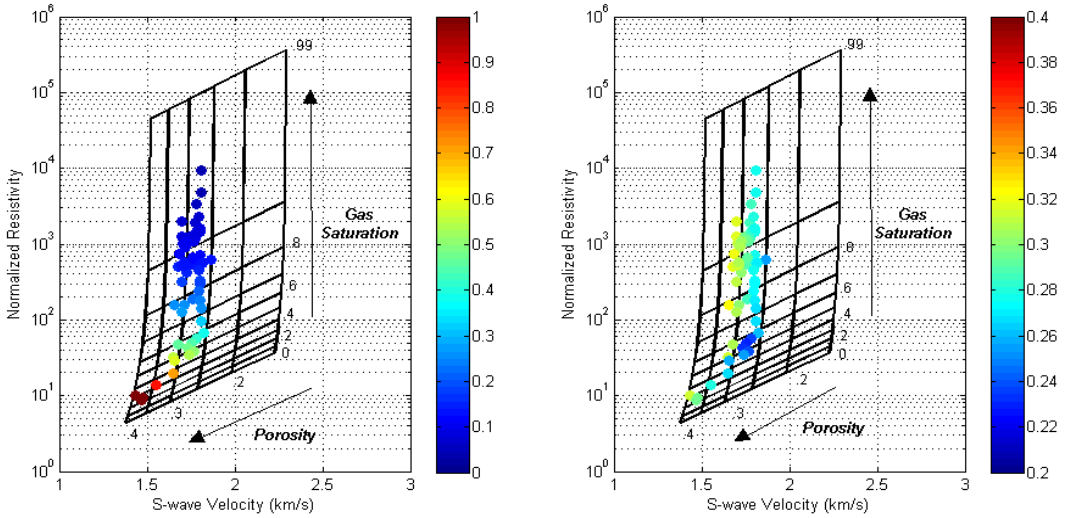

Figure 6.13: S-wave velocity-resistivity template for the Nuggets reservoir with log data superimposed. Color code is water saturation (left) and porosity (right).

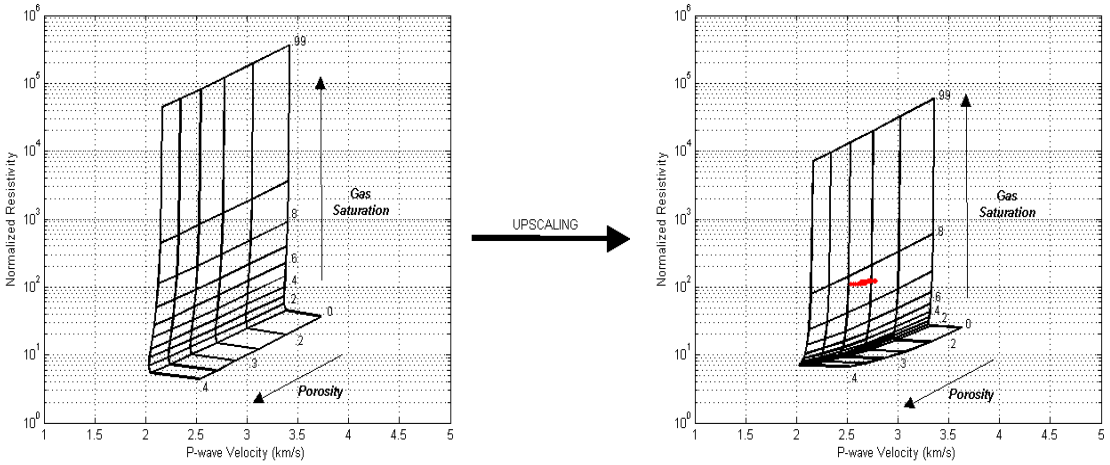

Figure 6.14: Left: a log-scale P-wave velocity-resistivity template, same as in Figure 6.12. Right: seismic/CSEM-scale template. The symbols are from the P-wave velocity and CSEM resistivity profiles, selected at the reservoir.

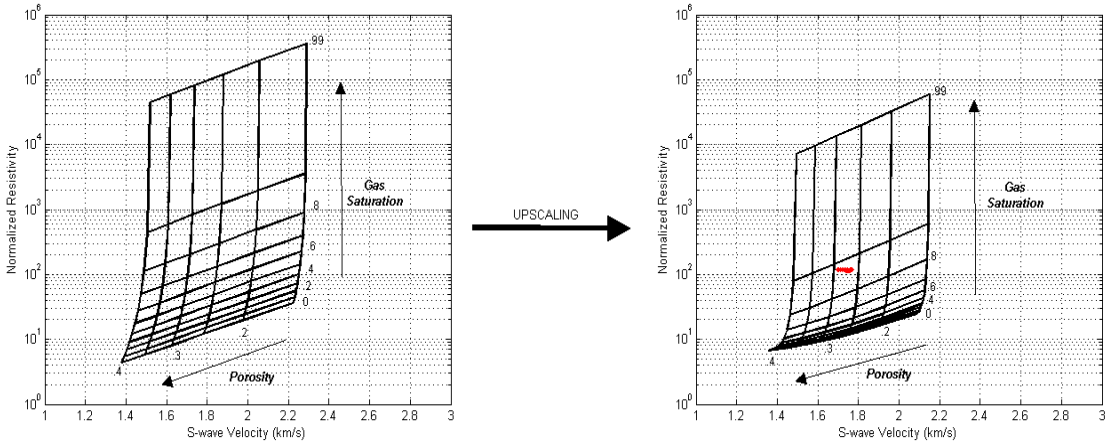

Figure 6.15: Left: a log-scale S-wave velocity-resistivity template, same as in Figure 6.13. Right: seismic/CSEM-scale template. The symbols are from the S-wave velocity and CSEM resistivity profiles, selected at the reservoir.

6.5 Porosity and Saturation predictions from Acoustic Impedance and Resistivity sections

The sections of resistivity inverted from CSEM data and acoustic impedance inverted from stacked seismic data (Figure 6.16) can be employed to estimate porosity and saturation over the whole reservoir using the upscaled acoustic impedance versus resistivity template given in Figure 6.7. This inversion process requires comparing the acoustic impedance and resistivity values from the sections at each spatial position with those for each cell in the template, and then assigning the given porosity and saturation values to that location (Figure 6.17).

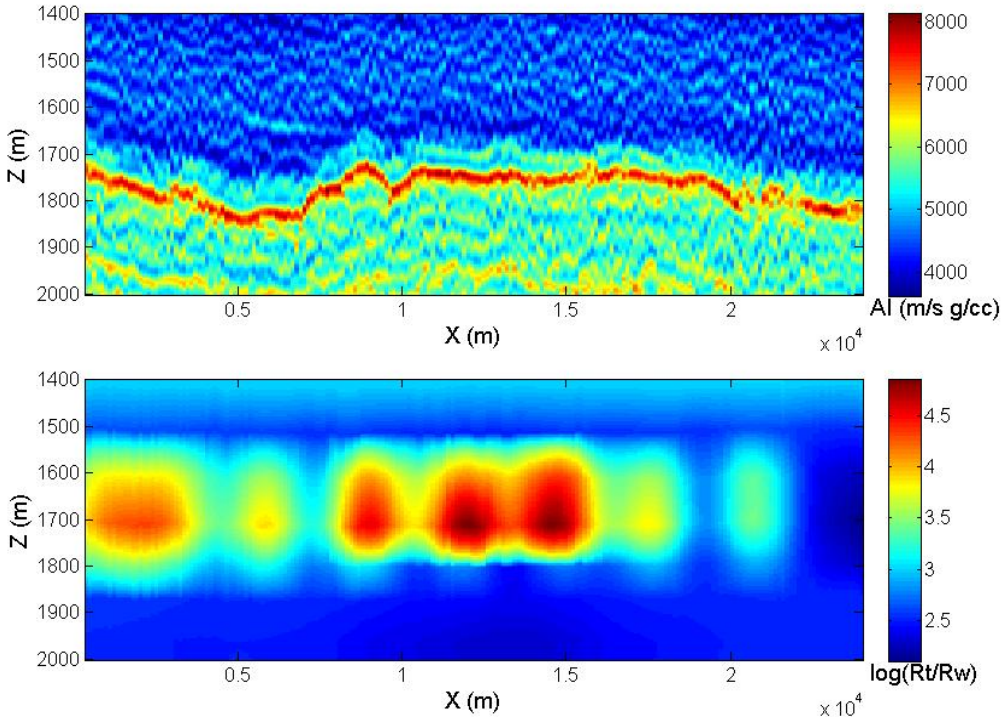

Figure 6.16: Acoustic impedance (m/s g/cc) and natural logarithm of normalized resistivity sections, well used to derive templates is located in the middle of the section.

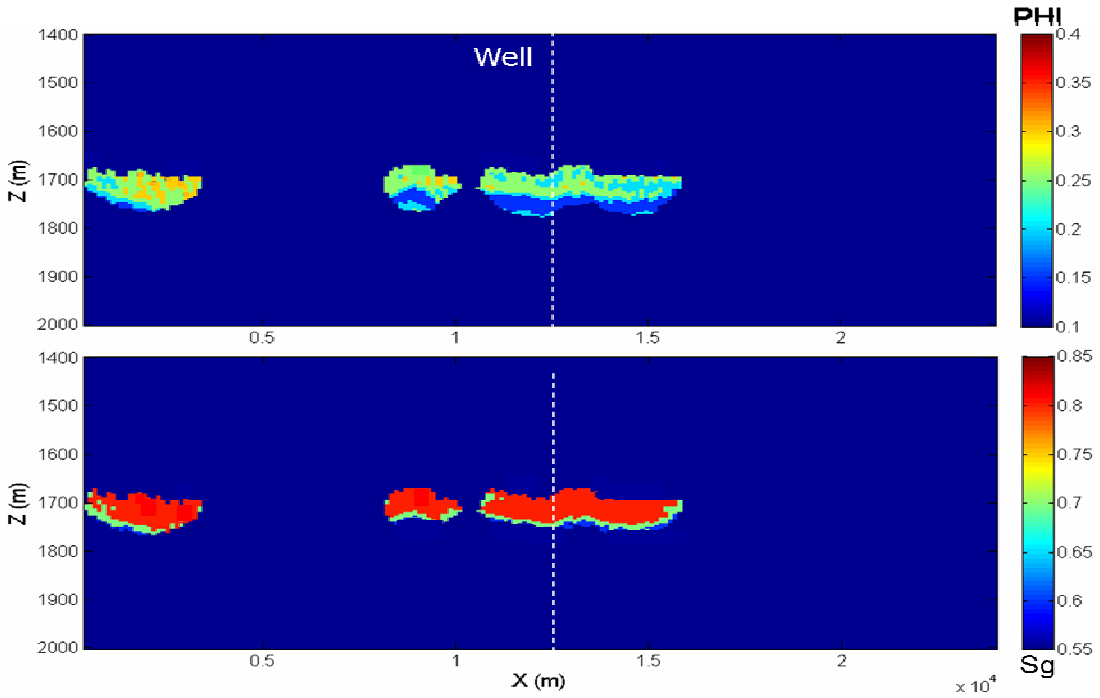

Figure 6.17: Porosity (PHI) and gas saturation (Sg) derived using upscaled acoustic impedance-resistivity templates in Figure 6.7. Porosities are only given correctly in reservoir interval (i.e., limited to where resistivity is larger than 5 ohm m). Gas saturations shown in dark blue are all those values smaller than 0.55.

It is important to remember that the porosity and saturation estimates will be correct only at the reservoir level for which the resistivity and acoustic impedance models were derived. Outside of the reservoir, these models are not valid; therefore, the estimates of porosity and saturation will not be correct. This is the reason why we obtain high saturation values in regions outside the reservoir, because we are not using appropriate models for these intervals, where clay content is larger than in the reservoir (see gamma ray log in Figure 6.1).

Also, another important limitation to estimate porosity and saturation is the low resolution of the CSEM data, combined with the low sensitivity of the acoustic

impedance to gas saturation for this particular reservoir, which causes that the reservoir appears thicker than it actually is in the saturation section. We could use the low-porosity interval at around 1750 m to delineate the base of the reservoir (Figure 6.17).

The reservoir could be also delineated using a section of porosity times gas saturation, which is equivalent to hydrocarbon volume. We can observe from this section, shown in Figure 6.18, the top, bottom and lateral extent of the reservoir more clearly.

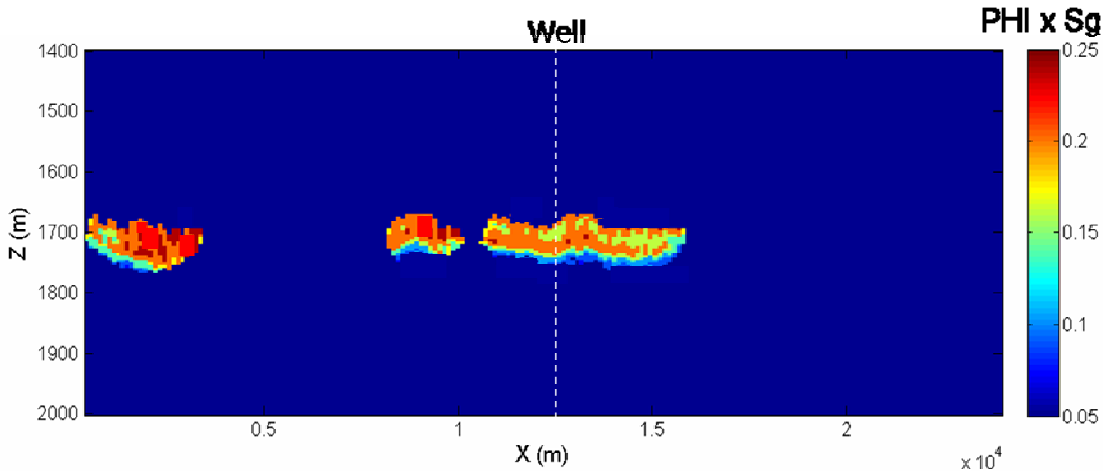

Figure 6.18: Product of porosity (PHI) and gas saturation (Sg) sections shown in Figure 6.17.

6.6 Conclusions

Rock physics impedance - resistivity templates are useful interpretation tools, which can allow us to estimate porosity and saturation from well logs and from field data. Appropriate theoretical models must be chosen to construct these templates, honoring the regional geological trends. We can use the Backus average to upscale the

elastic properties, and the arithmetic average to upscale resistivity to the field scale.

To construct the templates, we can use not only the acoustic impedance, but also other seismic attributes, such as the elastic impedance or seismic velocity. This can help to reduce uncertainty by integrating different attributes in the interpretation. A seismic data alone can help us identify gas sand versus water sand, but an electromagnetic dataset is definitely a more powerful tool for distinguishing commercial from non-commercial gas accumulations.

Chapter 7
Seismic Inversion using Low-Frequency Impedance Trend from CSEM Resistivity

7.1 Abstract

Seismic inversion is highly dependent on the initial P-wave impedance model. We generally use filtered well log data combined with moveout velocities to constraint this model, but generally at shallow depths no well log data are available. Also, conventional seismic reflection data has an information gap in the ~2-10 Hz frequency band, and, therefore, does not contain information about the background impedance trend. On the other hand, controlled-source electromagnetic (CSEM) data have low resolution and contain information in this gap about the earth's resistivity structure. Rock-physics relations between resistivity and porosity, and acoustic impedance and porosity can be used to extract information from the CSEM data to provide constraints on the low-frequency and the shallow seismic impedance section. Porosity is the main link that allows us to develop and use these cross-property relations. We used Archie's

equation and the soft-sand model to estimate the low-frequency seismic impedance trend from CSEM data. We combined this trend with well log data information to estimate an initial model for seismic inversion. Results show that appropriate cross-property relations can capture the background low-frequency impedance trend, particularly at shallow depths where no well information is available, and can provide useful constraints on prior models for inversion. Validation tests showed that the residuals of acoustic impedance are lower, and the fit is better with the background model constrained by the impedance trend obtained from the CSEM data.

7.2 Introduction

Seismic impedance inversion can be very useful for reservoir characterization. Inversion schemes are highly dependent on the prior impedance model used as an input. This initial model is generally created from well log data, combined with moveout velocities. However logs in general are not recorded over all of the overburden. Conventional band-limited seismic reflection data do not contain information about the impedance in the low-frequency (~ 2-10Hz) band (Claerbout, 1985; Jannane et al., 1989). Hence, it is important to constrain the low-frequency and shallow seismic impedance trend in the prior model used for the inversion, as highlighted my many authors (e.g. Dragoset and Gabitzsch, 2007).

Mukerji et al., (2008, 2009) suggested that since controlled-source electromagnetic (CSEM) data contain information about the earth resistivity in the low-frequency band where the seismic data does not, it could be possible to use CSEM derived resistivity to constrain the background impedance trend. In addition, CSEM data also contain

information in the shallow section, where no well log data are available to constraint the seismic inversion.

We apply a simple approach where cross-property rock physics relations between elastic and electrical properties can be used to extract information from the CSEM data to provide constraints on seismic impedance.

7.3 Cross-property relations

Faust (1953) developed an empirical relation between velocity and resistivity, still commonly used. Other important theoretical work on cross-property relations includes Brito Dos Santos et al. (1988), Berryman and Milton (1988), Gibiansky and Torquato (1996), and Kachanov et al. (2001). More recently, Carcione et al. (2007) have compiled and derived cross-property relations and bounds relating electrical conductivity to elastic moduli and velocities of rocks. The cross-property relations are based on existing empirical and theoretical relations between electrical conductivity and porosity and between elastic moduli and porosity. The basic approach is as follows. If the relation between porosity, ϕ, and conductivity, σ, is described by $\sigma = h(\phi)$, and the relation between elastic velocity v and porosity is given by $v = g(\phi)$, then the cross-property relation can be obtained by eliminating ϕ to give $\sigma = h(g^{-1}(v))$.

When two relations for elastic and electric properties are combined to obtain a cross-property relation, the resulting equation will be a good description of the cross-relation only if the original equations for elastic and electrical properties themselves

are good descriptors. While many cross-property relations have been derived using this approach, these cross-relations should be tested with controlled data. In the next section, we will apply some of these existing cross-property relations, and will calibrate a new relation using log data and rock physics models.

7.4 Application to Field Data

The data set that we use is from the Nuggets-1 gas field. This field is located in the North Sea, offshore from the UK in 115 m of water. The sand reservoir belongs to the Eocene Frigg formation and is about 25 m thick at a depth of 1690 m (Harris and MacGregor, 2006). We first estimate P-wave velocity from resistivity using some previous cross-property relations, such as Faust (1953), and Hacikoylu et al. (2006). However, we find that both relations overestimate P-wave velocity, particularly in the shallow section (Figure 7.1).

In order to have a new P-wave impedance – resistivity transform, we use the soft-sand model (Dvorkin and Nur, 1996) to estimate impedance, and Archie's equation (Archie, 1942) to estimate resistivity. Water salinity in this area is around 35,000 ppm, which corresponds to a water resistivity around 0.1 ohm m at the reservoir depth. The depths of interest where the log data starts is around 1500m, giving an effective pressure of around 20 MPa assuming normal pressure gradients in this area. If we assume a shaly column (60% shale and 40% sand), a coordination number of 6 and a critical porosity of 40%, we can estimate P-wave impedance using the soft-sand model. We compute resistivity using Archie's equation with tortuosity factor $a = 1$ and cementation or porosity exponent $m = 2.6$. If we evaluate these models for porosities

between 0.1 and 0.6, which are the porosities we are most likely to encounter, and we plot acoustic impedance versus formation factor (for 100% water saturation), we obtain the blue curve in Figure 7.2. This plot is basically linear in the porosity range we are considering; therefore we can find a linear fit (R^2=0.9985):

$$\mathrm{AI\,(km/s\,g/cc)} = 2.3 \cdot \log_{10}(F) + 1.6 \,. \qquad (7.1)$$

This equation is not a fit to the well log data, but to the soft-sand and Archie models (black curve in Figure 7.2). We chose the parameters specified above for the models because we were trying to use typical theoretical parameters that we would have selected for shaly intervals.

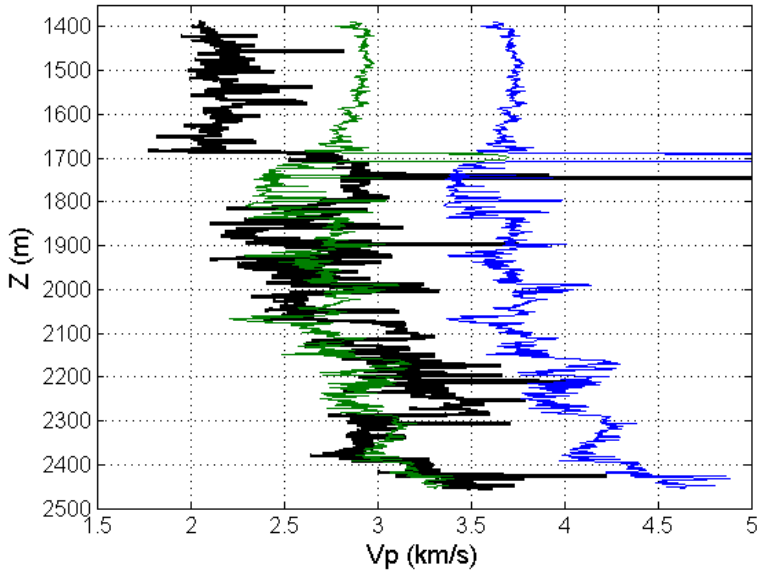

Figure 7.1: P-wave velocity log (km/s) in shown in black. The blue and green curves are estimates from Faust (1953) and Hacikoylu et al. (2006) respectively.

Now, we use this transform to generate an initial acoustic impedance section from the resistivity section inverted from CSEM data, and replace it by the log data where

available (Figure 7.3). We used a fixed water resistivity (0.1 ohm m, value encountered at the depth of interest) for the entire interval where we use the transform, although there are important variations with depth (Figure 7.4). We are only creating an initial model for the seismic inversion; therefore, it does not have to be as precise.

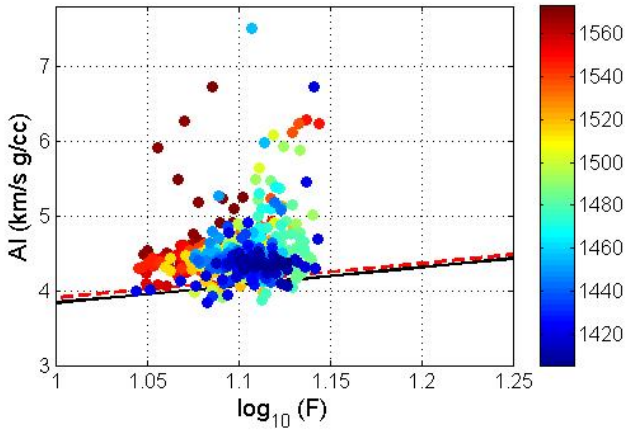

Figure 7.2: Acoustic impedance versus decimal logarithm of formation factor (Rt/Rw). First 500 data points of the well data are plotted, and colorcoded by depth (m). The black line is the soft-sand model versus Archie's equation for porosities between 10 and 60%, and the red line is a linear fit to the blue line given by Equation 7.1.

The resistivity inversion provided to us was done by a commercial vendor using a 2.5 D inversion algorithm. We performed model-based seismic inversion in the Hampson and Russell commercial software. A soft constraint allowing 50% variation in acoustic impedance was applied. We used a multi-trace inversion, for every 5 traces (Figure 7.5). The difference between the seismic amplitude data and the resulting inverted seismic amplitudes are shown in Figure 7.6.

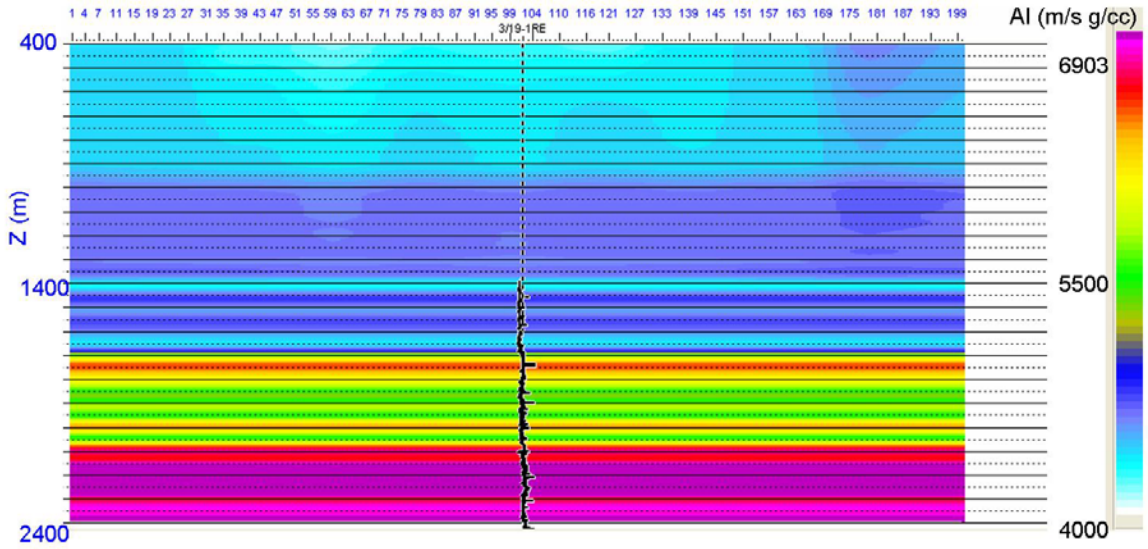

Figure 7.3: Initial model of acoustic impedance (m/s g/cc) section in depth, generated using the CSEM and well data. Well is at center of the section.

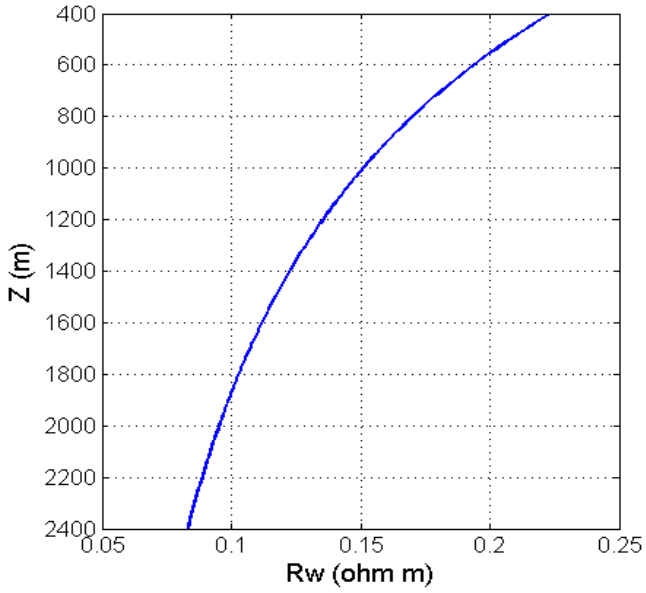

Figure 7.4: Formation water resistivity (Rw) in ohm m, computed using Schlumberger Gen-6 chart, assuming a water salinity of 35,000 ppm, and a normal pressure gradient 30°C per km.

To analyze these results, we perform seismic inversion using the same parameters, but building the model using only the well log acoustic impedance as initial input (Figures 7.7 and 7.8). If we now compare the residuals in seismic amplitude for both inversions (Figures 7.6 and 7.9), they are very similar. Same observation can be made from the difference between the estimates at the well location and the well data, and by comparing the estimates at the well (Figure 7.10). Using as starting model only the well, or the well plus the CSEM data to generate an initial model gives similar results, with similar seismic amplitude and acoustic impedance residuals.

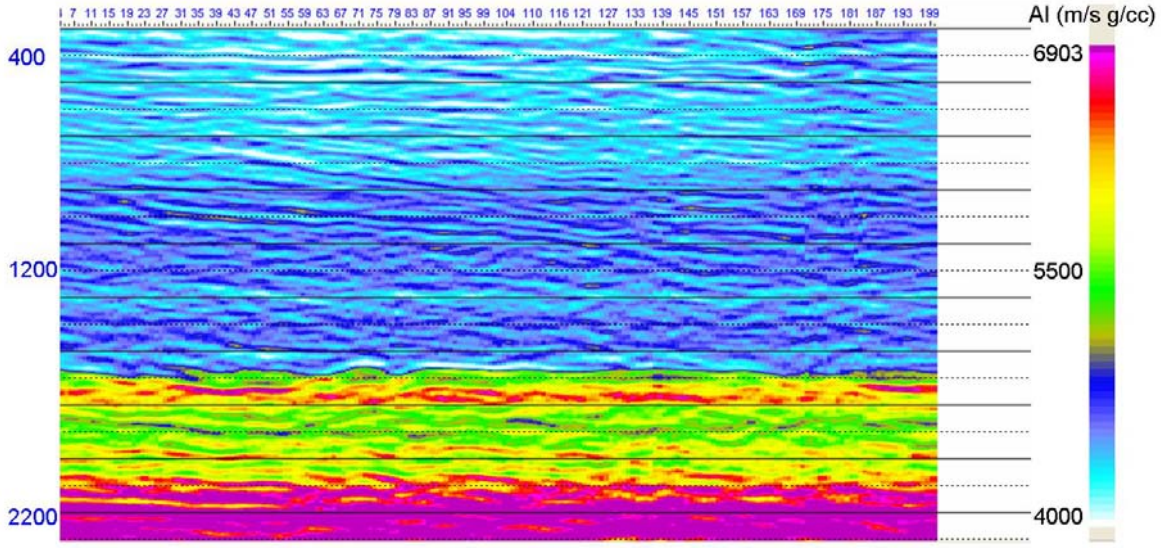

Figure 7.5: Acoustic impedance (m/s g/cc) section in two-way travel time (ms) resulting from seismic inversion starting with model in Figure 7.3. Well is at center of the section.

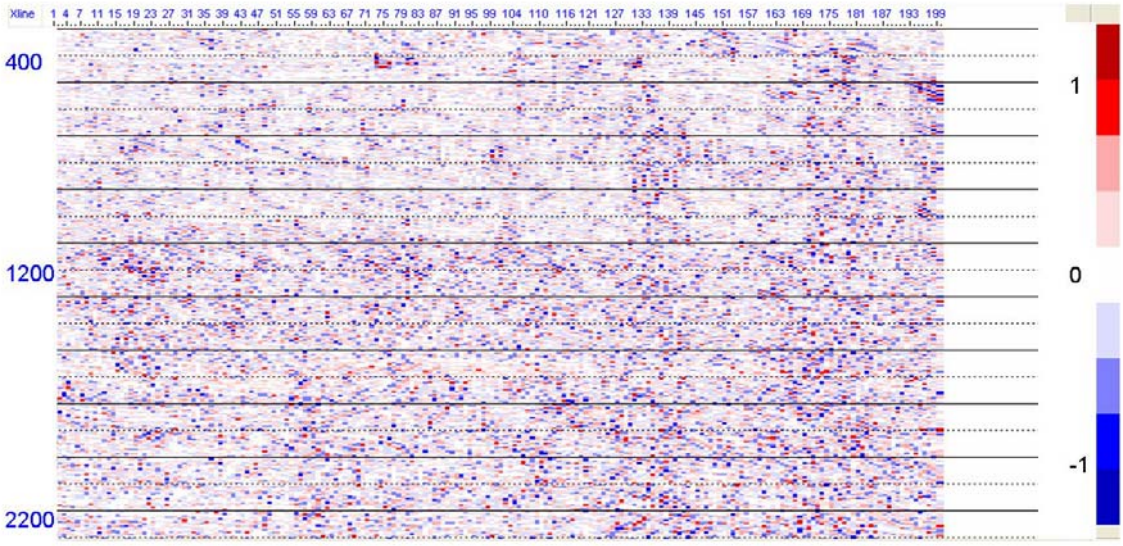

Figure 7.6: Difference between the stacked seismic amplitude data and the modeled seismic amplitude starting with inversion result in Figure 7.5, given in two-way traveltime (ms).

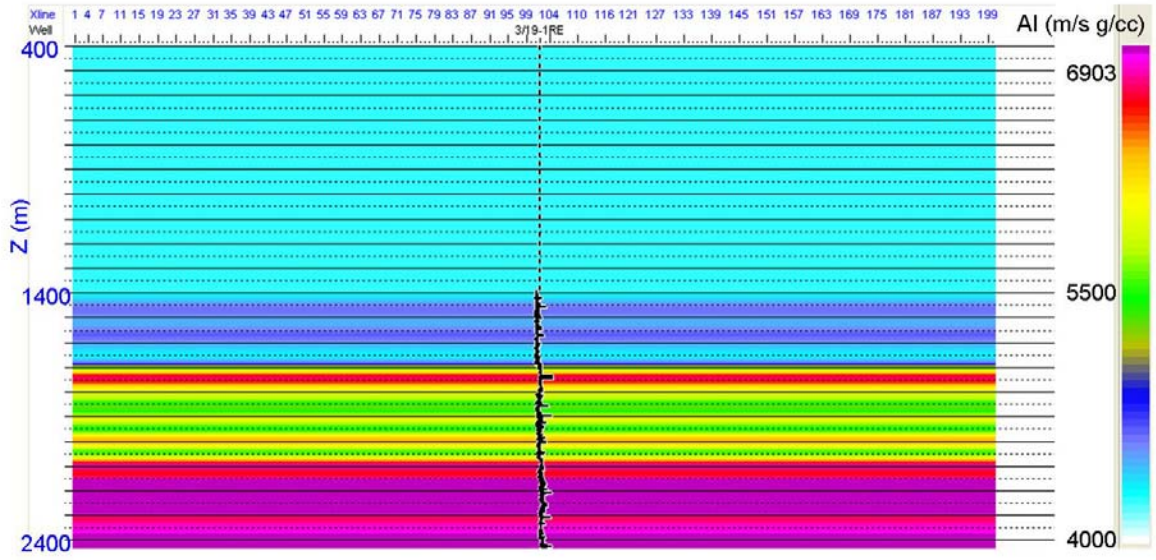

Figure 7.7: Initial model of acoustic impedance (m/s g/cc) section in depth, generated only from well information. Well is at center of the section.

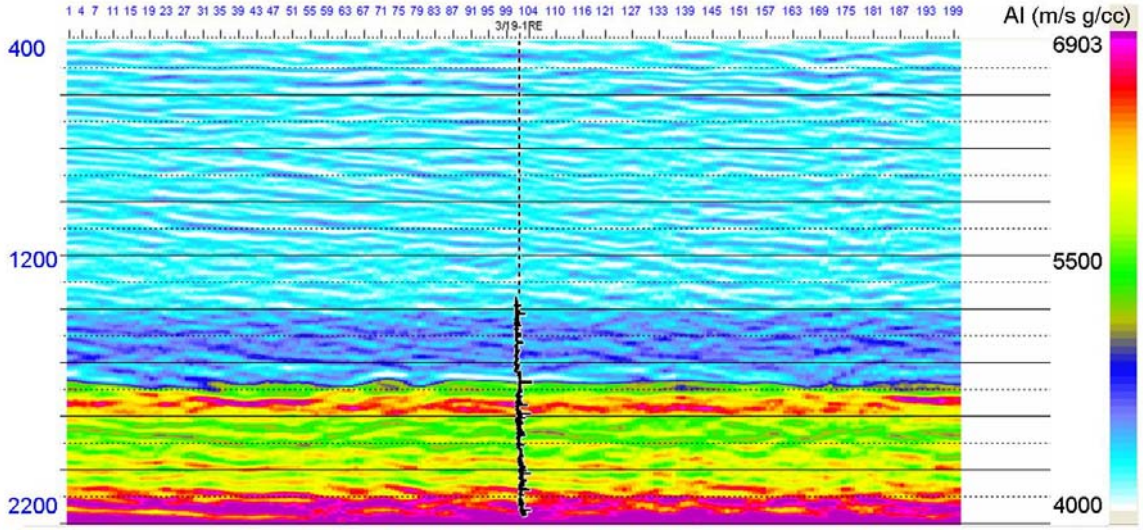

Figure 7.8: Acoustic impedance (m/s g/cc) section in two-way travel time (ms) resulting from seismic inversion starting with model in Figure 7.7. Well is at center of the section.

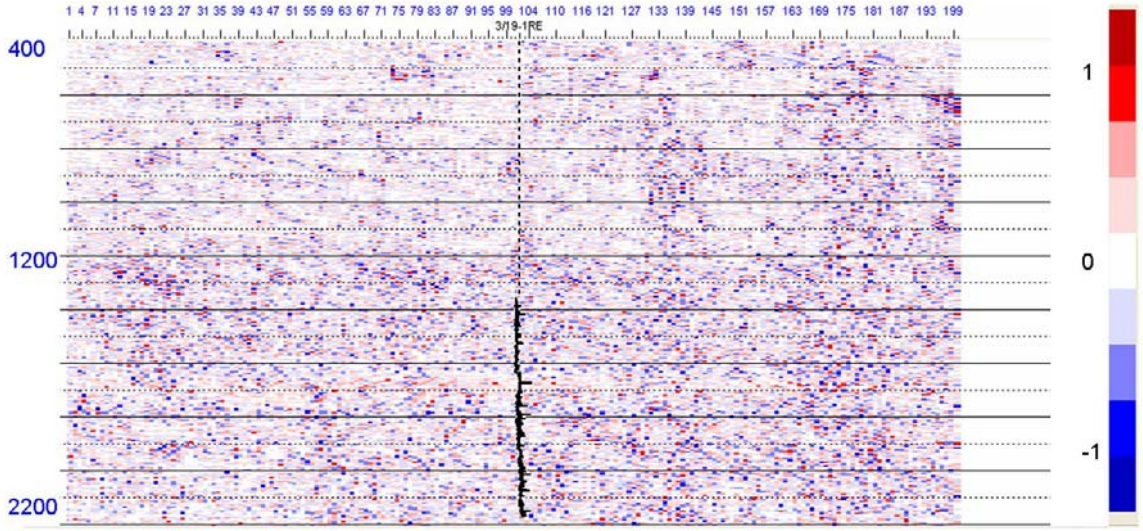

Figure 7.9: Difference between the stacked seismic amplitude data and the modeled seismic amplitude starting with inversion result in Figure 7.8, given in two-way traveltime (ms).

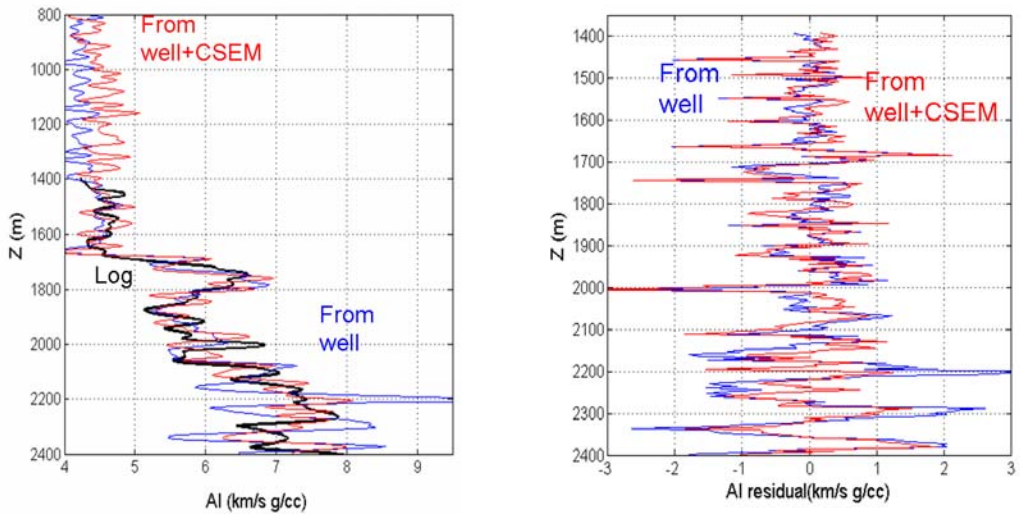

Figure 7.10: On the left, acoustic impedance in km/s g/cc at well location. On the right, difference between acoustic impedance from well data and inversion in km/s g/cc. The actual well data are in black, inversion result starting only with well is in blue, and inversion result starting with CSEM and well is in red.

We see more layered structure in the overburden for the inversion using the CSEM+well as a prior model (Figure 7.5), compared to the inversion using only the well as a prior model (Figure 7.8). However, we do not know if we have improved the results of the inversion by including the CSEM data since we do not know the actual acoustic impedance in the overburden. Therefore, a validation exercise was carried out to test if adding the acoustic impedance estimates from CSEM data improves the seismic inversion result. The validation was done by leaving out a portion of the log data, and then comparing the inversions from the two prior models. The log data above and in most of our reservoir, hence any depths shallower than 1700 m, is left out. Acoustic impedance sections are created using only the partial log data from 1700 m and deeper (Figure 7.11), and combining this limited log data with our model estimated from the CSEM data (Figure 7.14). We performed seismic inversions using

similar parameters as before (Figures 7.12 and 7.15), and compared the seismic amplitude residuals over the entire section. We also compared the well log data and the resulting acoustic impedance from the inversions at the well location. The overall residuals of the seismic data fit were about the same for both prior models (Figures 7.13 and 7.16). However, when we compare the results at the well (Figures 7.17 and 7.18), in particular in the section we had excluded as input, we observe that we fit better the well data when we start with the model that includes the trend derived from the CSEM data. Computing the root mean and median squared residuals of acoustic impedance in this section where we ignore the log data, we obtain 0.600 and 0.278 km/s g/cc when we include well+CSEM, compared to 0.861 and 0.803 km/s g/cc when we only incorporate the well data. Hence, there is a significant improvement when CSEM data are included. In the sections where well data were used as inputs, the root mean and median squared residuals are similar in both cases: 0.781 and 0.508 km/s g/cc for well+CSEM, and 0.715 and 0.445 km/s g/cc for only well. Also, if we observe the results of the inversion, the one that started with the well+CSEM prior model shows smoother variations in the overburden between 4000 and 5000 m/s g/cc, while the one that includes only the well data shows larger and less smooth acoustic impedance values that alternate between 4500 and 5500 m/s g/cc, which would be too high for the some of the very shallow intervals.

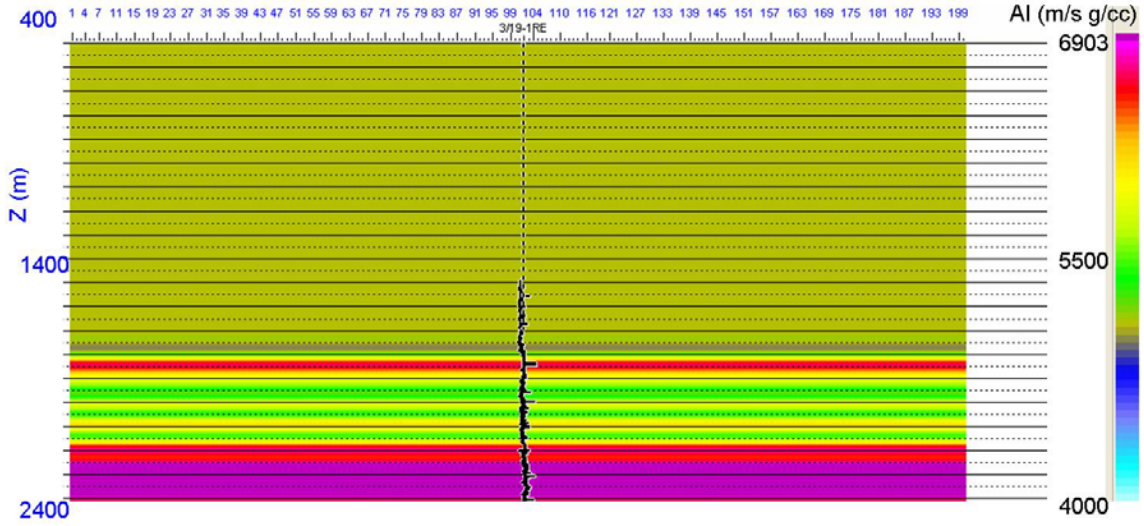

Figure 7.11: Initial model of acoustic impedance (m/s g/cc) section in depth, generated only from the well information for depth larger than 1700 m. Well is at center of the section.

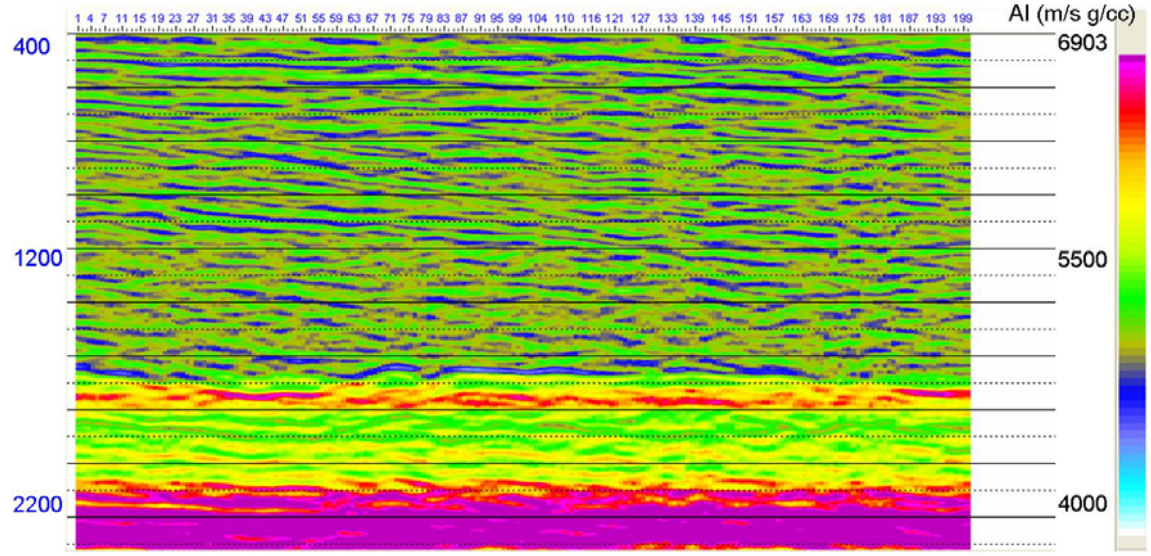

Figure 7.12: Acoustic impedance (m/s g/cc) section in two-way travel time (ms) resulting from seismic inversion starting with model in Figure 7.11.

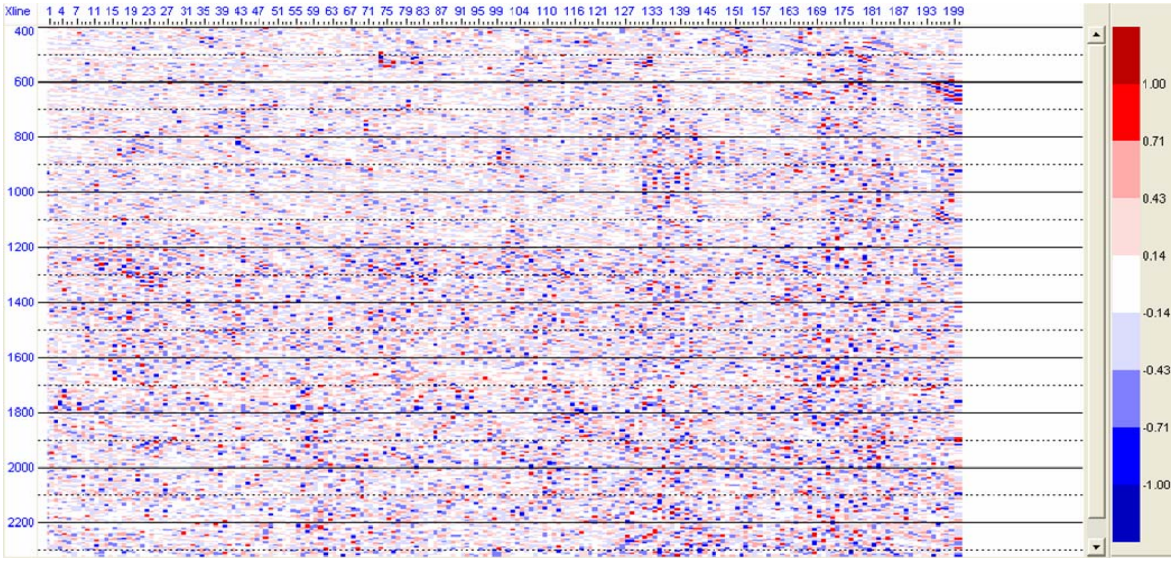

Figure 7.13: Difference between the stacked seismic amplitude data and the modeled seismic amplitude starting with inversion result in Figure 7.12, given in two-way traveltime (ms).

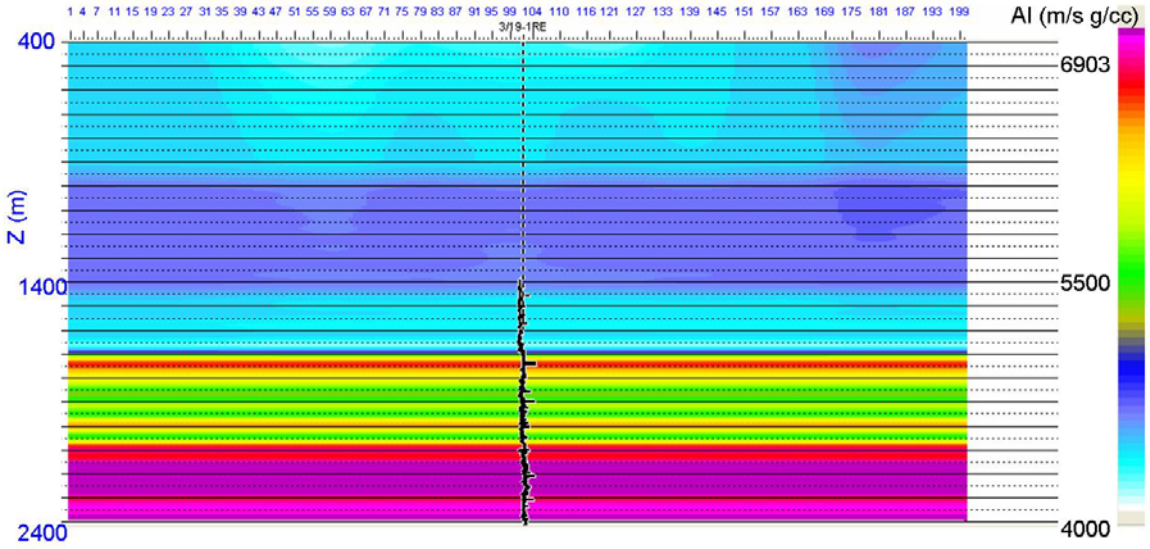

Figure 7.14: Initial model of acoustic impedance (m/s g/cc) section in depth, generated from the CSEM data and the well information for depth larger than 1700 m. Well is at center of the section.

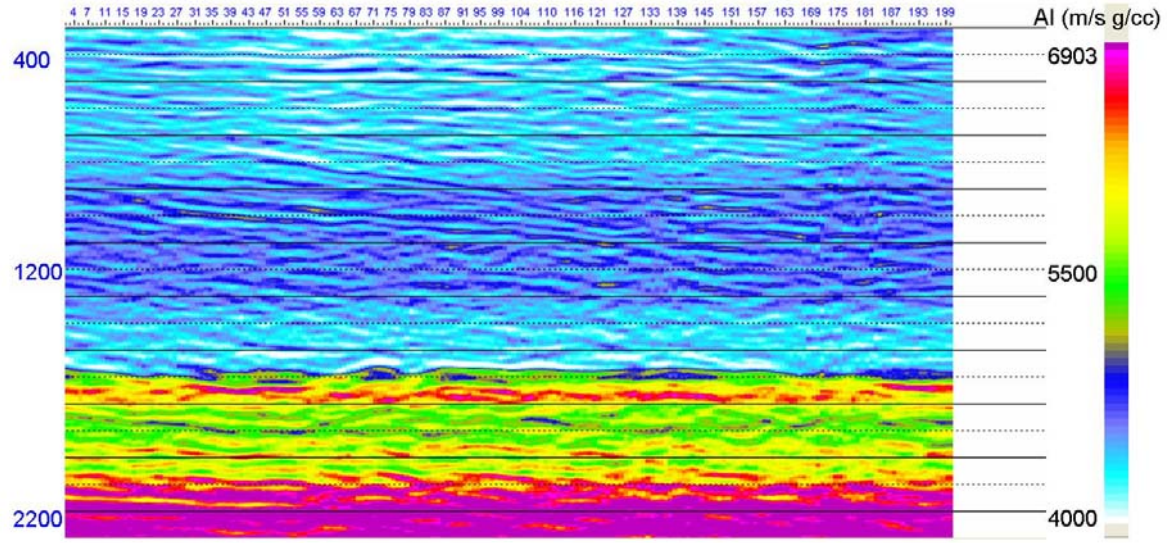

Figure 7.15: Acoustic impedance (m/s g/cc) section in two-way travel time (ms) resulting from seismic inversion starting with model in Figure 7.14.

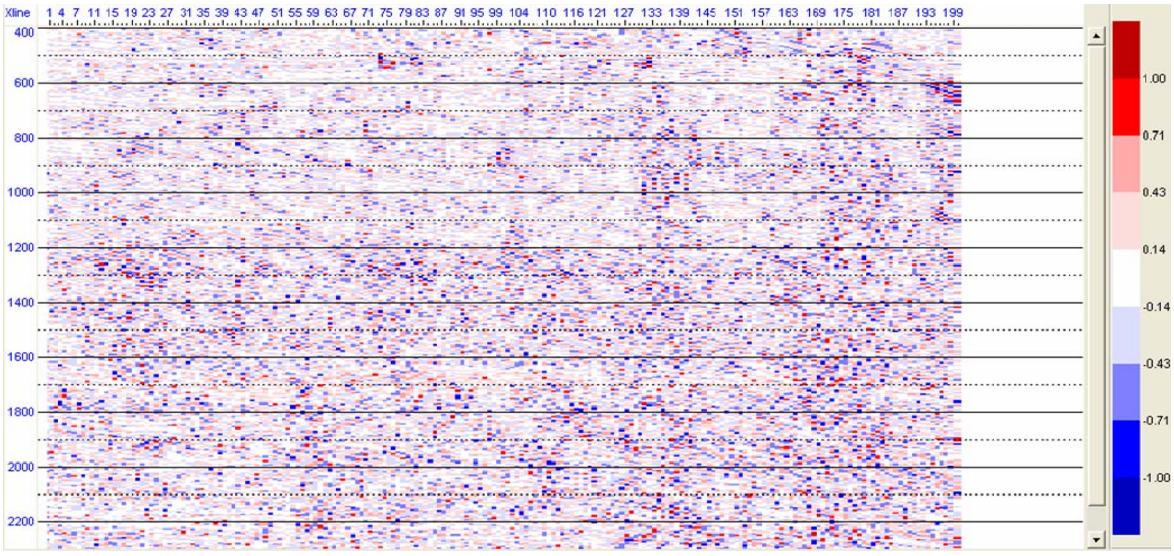

Figure 7.16: Difference between the stacked seismic amplitude data and the modeled seismic amplitude starting with inversion result in Figure 7.15, given in two-way traveltime (ms).

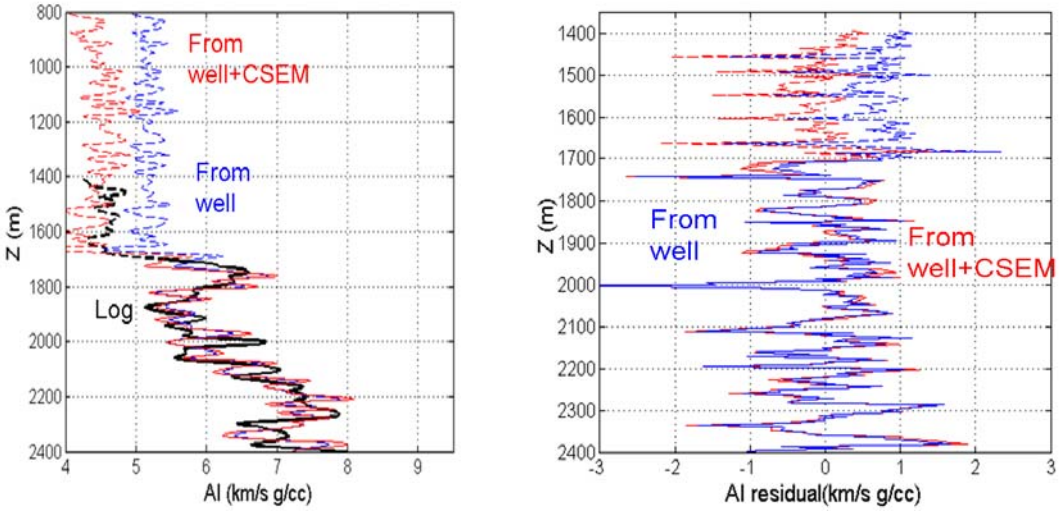

Figure 7.17: On the left, acoustic impedance in km/s g/cc at well location. On the right, difference between acoustic impedance well data and inversion in km/s g/cc. Well data are in black, inversion result starting only with well is in blue, and inversion result starting with CSEM and well is in red.

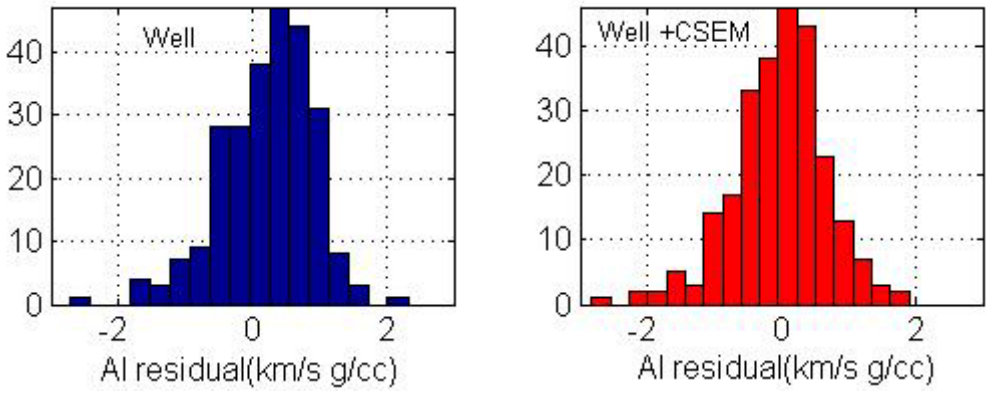

Figure 7.18: Histograms of the acoustic impedance residuals after inversion at the well location: (1) blue is the result from using only the well as an input, and its median and mean are 0.298 and 0.211 km/s g/cc, and (2) red is the result from using CSEM and well data as inputs, and its median and mean are 0.0080 and -0.047 km/s g/cc.

7.5 Sensitivity Analysis to input parameters in transform models

Different parameter values could be used as inputs to generate the resistivity – acoustic impedance transform. Tests are performed changing the cementation exponent in Archie's relation, and the coordination number and clay content in the soft-sand model.

First, keeping the elastic model parameters fixed and changing only the cementation exponent in Archie's equation from 2.6 to 2.3 and 2.0 (Figure 7.19), we obtain the following two transforms, respectively:

$$\mathrm{AI}(\mathrm{km/s\,g/cc}) = 2.6\log_{10}(F) + 1.6\,, \text{ and} \tag{7.2}$$

$$\mathrm{AI}(\mathrm{km/s\,g/cc}) = 3.0\log_{10}(F) + 1.6\,. \tag{7.3}$$

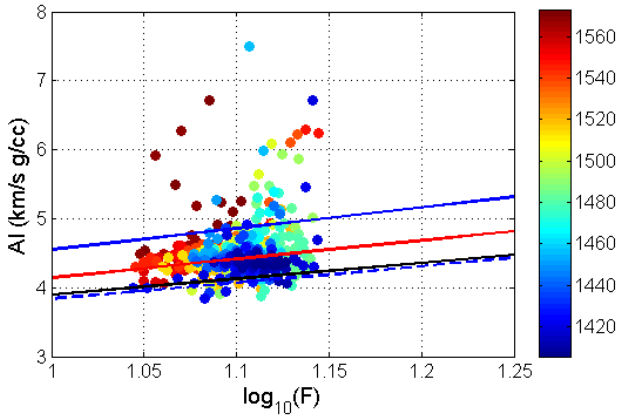

Figure 7.19: Acoustic impedance versus decimal logarithm of formation factor (Rt/Rw). First 500 data points of the well data are plotted, and colorcoded by depth (m). The black line is Equation 7.1, which is a linear fit to the dashed blue line (m=2.6). The solid blue curve is for m=2, and the red curve is for m=2.3.

Second, we observe that increasing the clay content to 0.8 is equivalent to changing the coordination number to 4 (Figure 7.20), and we obtain similar transforms in both cases, which for m=2.6, 2.3 and 2.0 are:

$$\mathrm{AI}(\mathrm{km/s\,g/cc}) = 2.1\log_{10}(F) + 1.7, \tag{7.4}$$

$$\mathrm{AI}(\mathrm{km/s\,g/cc}) = 2.3\log_{10}(F) + 1.7, \text{ and} \tag{7.5}$$

$$\mathrm{AI}(\mathrm{km/s\,g/cc}) = 2.7\log_{10}(F) + 1.7. \tag{7.6}$$

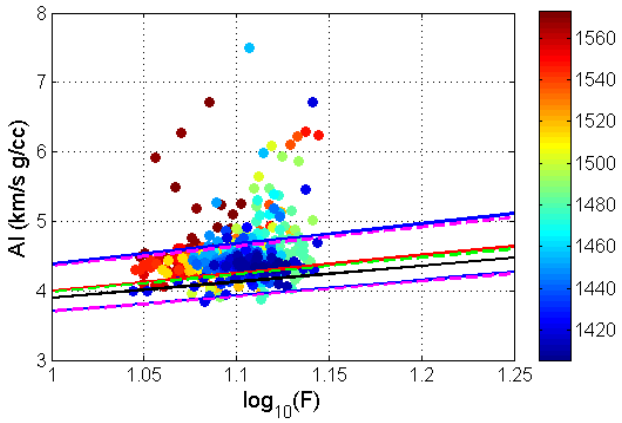

Figure 7.20: Same as Figure 7.19. The black line is Equation 7.1. Using clay content 0.8 and coordination number of 6 in the soft-sand model, we obtain the lower blue line for m=2.6, the red curve for m=2.3, and the upper blue line for m=2. Using clay content of 0.6, but coordination number of 4, we obtain the lower dashed magenta line for m=2.6, the green dashed curve for m=2.3, and the upper dashed magenta line for m=2.

Finally, we find that decreasing clay content to 0.4 is equivalent to changing the coordination number to 9 (Figure 7.21), and the transforms in this case for the three different m values (m=2.6, 2.3 and 2.0) are:

$$\mathrm{AI}(\mathrm{km/s\,g/cc}) = 2.4\log_{10}(F) + 1.6, \tag{7.7}$$

$$\mathrm{AI}(\mathrm{km/s\,g/cc}) = 2.7\log_{10}(F) + 1.6, \text{ and} \tag{7.8}$$

$$\mathrm{AI}\,(\mathrm{km/s\,g/cc}) = 3.1\log_{10}(F) + 1.6\,. \qquad (7.9)$$

The intercept in the relationship between acoustic impedance and formation factor does not change that much as we change the cementation exponent, or the clay content and coordination number. The slope in this equation, however, does vary more strongly.

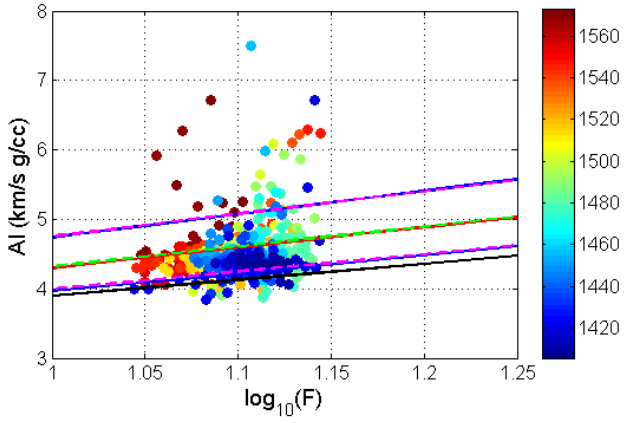

Figure 7.21: Same as Figure 7.19. The black line is Equation 7.1. Using clay content 0.4 and coordination number of 6 in the soft-sand model, we obtain the lower blue line for m=2.6, the red curve for m=2.3, and the upper blue line for m=2. Using clay content of 0.6, but coordination number of 9, we obtain the lower dashed magenta line for m=2.6, the green dashed curve for m=2.3, and the upper dashed magenta line for m=2.

We can now use some of these transforms in the validation test, instead of the one we had used before. Below, we show the initial models derived from CSEM-resistivity and well log data at the well for three different transforms given by Equations 7.4 and 7.9, which act like corridor bounds and also for Equation 7.2 which gives similar values as the log data (Figure 7.22).

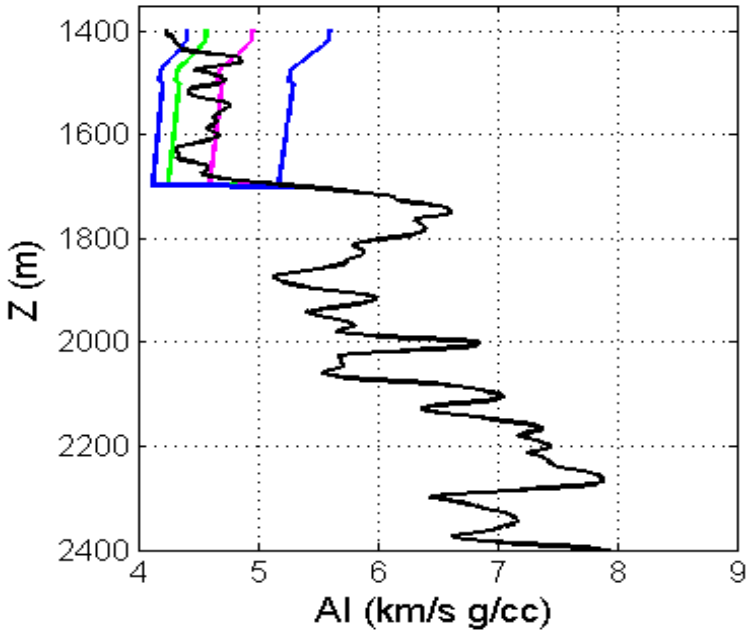

Figure 7.22: Acoustic impedance in km/s g/cc from well log data in black. Corridor bounds in blue are given by Equation 7.4 (lower bound) and 7.9 (upper bound) applied to CSEM data. Magenta curve corresponds to values obtained from Equation 7.2 applied to CSEM data for depths smaller than 1700 meters. Green curve is that derived from Equation 7.1 applied to CSEM data. For depths larger than 1700 m, all initial model curves correspond to the well log data.

When we apply Equation 7.2 to generate the initial acoustic impedance model from CSEM data, we also obtain lower acoustic impedance residuals, and a better fit to the well data than when we only use the well data (Figures 7.23 and 7.24). The same observation can be made when using the transform in Equation 7.4, as we can conclude from Figures 7.25 and 7.26. Therefore, using a resistivity – impedance transform, to generate an initial model from EM and well data, works better than using the well log data alone as the initial model.

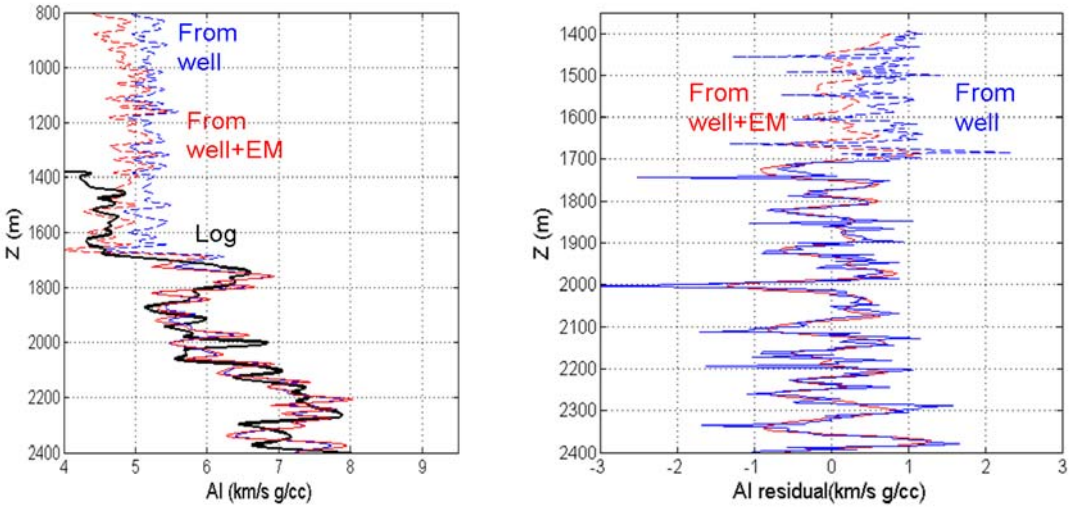

Figure 7.23: On the left, acoustic impedance in km/s g/cc at well location. On the right, difference between acoustic impedance well data and inversion in km/s g/cc. Well data are in black, inversion result starting only with well is in blue, and inversion result starting with CSEM and well is in red. Transform used is Equation 7.2.

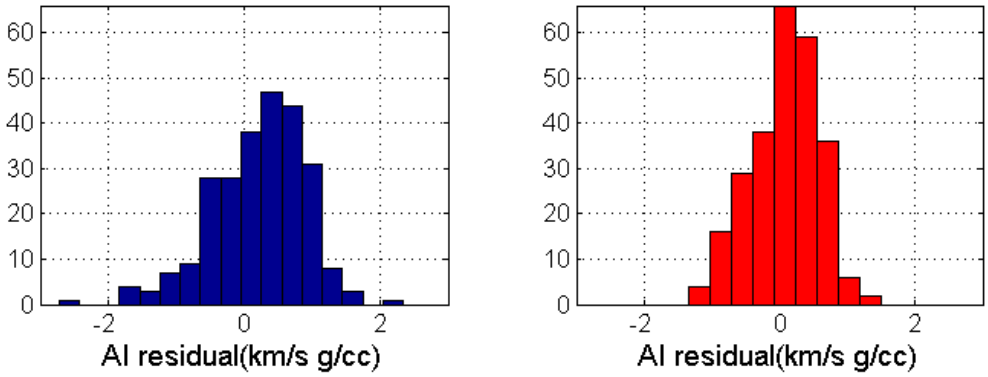

Figure 7.24: Histograms of the acoustic impedance residuals after inversion at the well location: (1) blue is the result from using only the well as an input, and its median and mean are 0.298 and 0.211 km/s g/cc, and (2) red is the result from using CSEM and well data as inputs, and its median and mean are 0.1475 and 0.1025 km/s g/cc. Transform used is Equation 7.2.

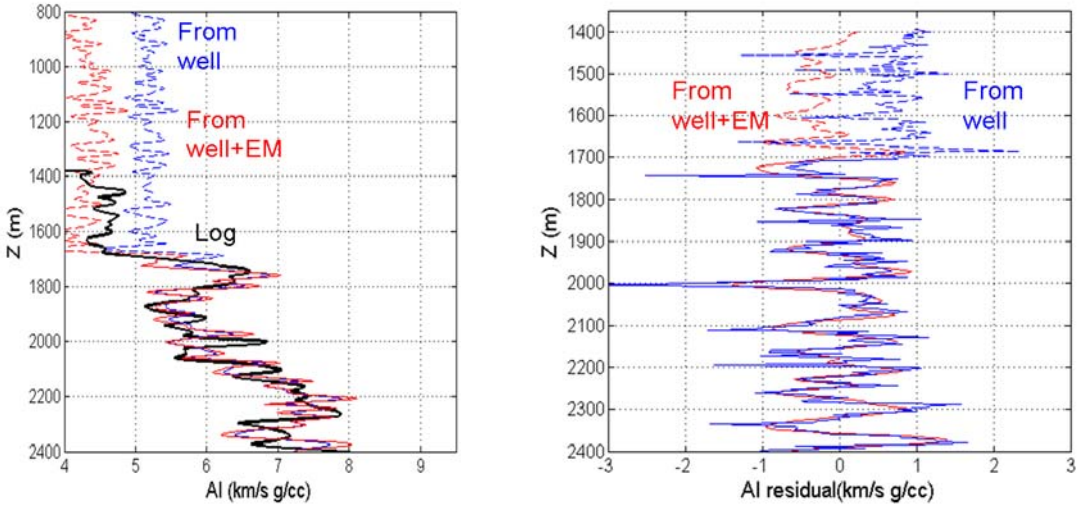

Figure 7.25: On the left, acoustic impedance in km/s g/cc at well location. On the right, difference between acoustic impedance well data and inversion in km/s g/cc. Well data are in black, inversion result starting only with well is in blue, and inversion result starting with CSEM and well is in red. Transform used is Equation 7.4.

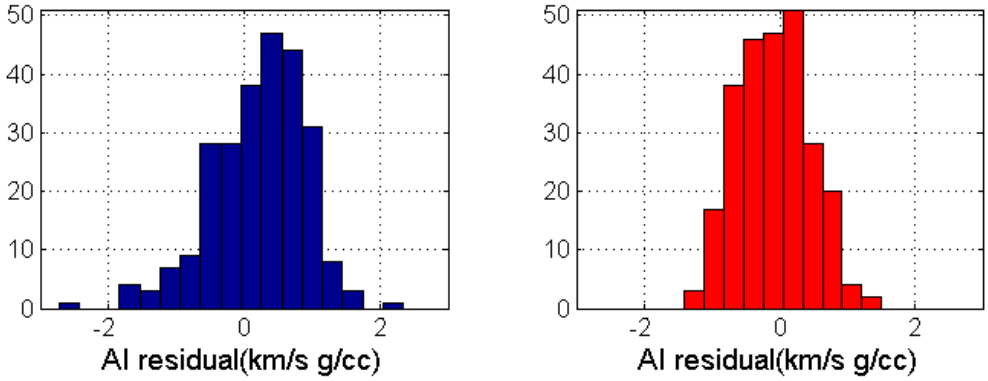

Figure 7.26: Histograms of the acoustic impedance residuals after inversion at the well location: (1) blue is the result from using only the well as an input, and its median and mean are 0.298 and 0.211 km/s g/cc, and (2) red is the result from using CSEM and well data as inputs, and its median and mean are -0.0921 and -0.0549 km/s g/cc. Transform used is Equation 7.4.

The root median and mean squared residual of acoustic impedance in the section where we ignore the log data are 0.270 and 0.868 km/s g/cc when we include well+CSEM and use Equation 7.2. On the other hand, they are 0.325 and 0.812 km/s g/cc if we apply Equation 7.4. We can compare these values with 0.803 and 0.861

km/s g/cc, which are the median and mean when we only use the well data. Hence, the acoustic impedance inversion results improve when CSEM data are incorporated to generate the initial acoustic impedance model.

When we use Equation 7.9, the inversion result from well+EM overpredicts acoustic impedance when compared to the log data (Figure 7.27). We observe that using this transform, the result is only slightly better to that when the EM data are ignored (Figures 7.27 and 7.28). The root median squared residual obtained using only the well in the entire section is 0.535 km/s g/cc, compared to 0.503 km/s g/cc when we use well+EM. Therefore, we should calibrate the transform that we will use with well log data, or we should use a transform that is appropriate for the lithology expected (e.g., shale or shaly sandstone).

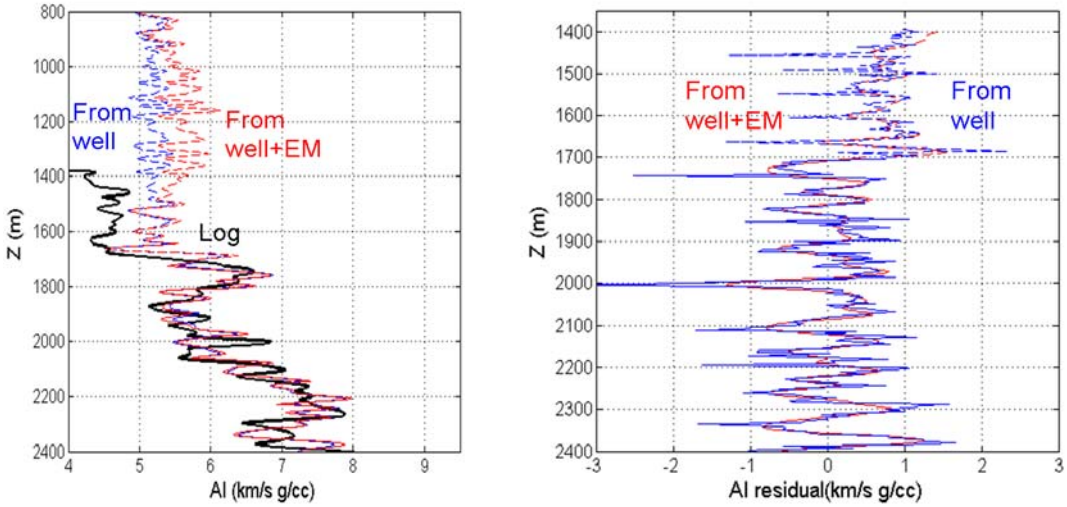

Figure 7.27: On the left, acoustic impedance in km/s g/cc at well location. On the right, difference between acoustic impedance well data and inversion in km/s g/cc. Well data are in black, inversion result starting only with well is in blue, and inversion result starting with CSEM and well is in red. Transform used is Equation 7.9.

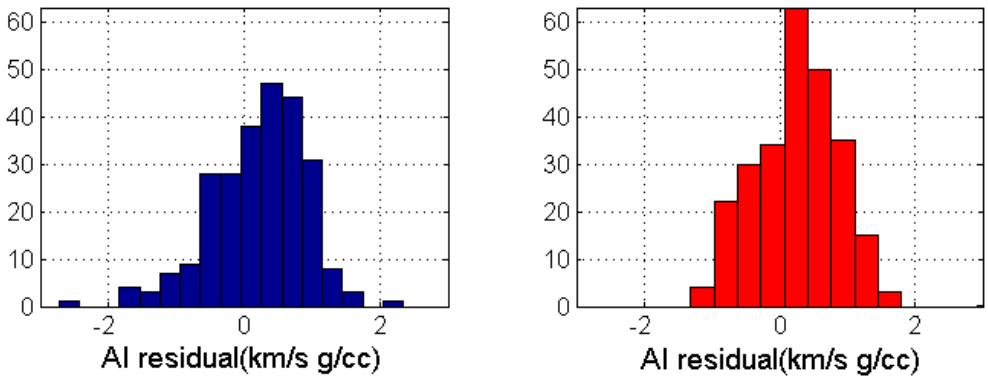

Figure 7.28: Histograms of the acoustic impedance residuals after inversion at the well location: (1) blue is the result from using only the well as an input, and its median and mean are 0.298 and 0.211 km/s g/cc, and (2) red is the result from using CSEM and well data as inputs, and its median and mean are 0.294 and 0.293 km/s g/cc. Transform used is Equation 7.9.

We observe that the choice of cementation or porosity exponent (m) in Archie's equation is important (e.g., between 2.3 to 2.6 in this case). Different studies have related m to grain and pore shape (Jackson et al., 1978; Ransom, 1984). According to Knight and Endres (2005), m depends on the geometry of the system or the connectedness of the pore space. The lower the connectivity in the pore space, the larger m tends to be. We selected a high m (larger than 2), because we expected that pore connectivity in the overburden interval was probably low, and we observed that in fact these large m values fit better the well data from the overburden (Figure 7.19). However, we also observe that even if had selected m=2, the inversion result would still improve, although not as significantly (Figure 7.28).

7.6 Conclusions

CSEM data can be a useful tool to constrain the shallow and low frequency acoustic impedance trend to use as initial model for seismic inversion. Appropriate elastic and resistivity models must be chosen in order to have a good prediction of

acoustic impedance given resistivity. These expressions can be calibrated using well data as shown, in particular taking into account the overburden.

Conventional cross-property relations as Faust (1953) and Hacikoylu et al. (2006) can over predict the acoustic impedance in friable sediments at shallow depths. If no well log data are available in the shallow section, using the CSEM-derived resistivity data and an adequate cross-property relation (for example, one based on the soft-sand model and Archie's equation) can be a good approach to predict the initial low frequency shallow acoustic impedance model. Validation tests showed that using the background trend from the CSEM data as a constraint in impedance inversion can give a better fit to the acoustic impedance.

Chapter 8
Gas Hydrate-bearing Sandstones: Elastic and Resistivity Modeling

8.1 Abstract

Hydrates have strong elastic and resistivity responses. Using acoustic impedance and resistivity, we can improve our description of hydrate-bearing sandstones, including their porosity and saturation. We show two well examples, one from Mallik, which corresponds to hydrates below permafrost, and the other from the Nankai Trough, which contains hydrates below the sea floor.

EM data are generally acquired in deep water where hydrates are common. The hydrates are resistors and can mask other resistors buried below them in an EM data section. This is an impediment to conventional hydrocarbon exploration but an advantage in exploration for gas hydrates.

We show that our ability to predict porosity and saturation of the hydrate-bearing layer from seismic data alone is highly dependent on the thickness of the layer and the properties of the overburden. It is not an impossible task if we have well control data

that we can use to learn the appropriate models and properties to use for the overburden. Porosity and saturation estimates from the seismic data can then be used to constrain the resistivity of the hydrates in an initial subsurface resistivity model for an EM inversion.

8.2 Introduction

Natural gas hydrates are crystalline solids forming a hydrogen-bonded water lattice with entrapped guest molecules, mostly of methane (Helgerud et al., 1999). They occur at a limited range of high pressures and low temperatures, in marine sediments below the sea floor and in permafrost regions (Prensky, 1995). Their density and P-wave and S-wave velocities are very close to those of ice (0.910 g/cc, 3.60 km/s and 1.90 km/s for hydrates, compared to 0.917 g/cc, 3.89 km/s and 1.97 km/s for ice, respectively, Helgerud, 2001).

Gas hydrate-bearing sediments tend to have high acoustic impedance, as compared to the background sediment. Often, free gas accumulates just below the hydrates, giving rise to a strong seismic reflection at the base of the hydrates. This reflection is generally known as a bottom-simulating reflector (BSR), because it is typically parallel to the sea floor.

Hydrates are also electrically resistive, and constitute a challenge when any remote electromagnetic data are acquired, since their response makes it difficult to distinguish a hydrocarbon reservoir lying deeper. A BSR in a seismic section or volume is a sign of the presence of hydrates, and is a warning that these shallow resistors will have a very important effect on any remote resistivity (CSEM or transient EM)

measurements. The question is whether the seismic response can help predict and model these shallow resistors, so that we can distinguish them from possible deeper resistors that could correspond to hydrocarbon reservoirs.

We attempt to address this question by making a gas-hydrate modeling catalogue. In this catalogue, given porosity and saturation, we model all possible P-wave impedances to determine whether the prediction of these reservoir properties from seismic data is possible. We then use these porosity and saturation values to compute the possible resistivity response, which, in turn, can be used as an initial model in the shallow section for an EM data inversion.

8.3 Elastic Modeling

Dvorkin and Uden (2004) and Cordon et al. (2006) showed that the soft-sand model (Dvorkin et al., 1999), which includes the hydrates as part of the load-bearing frame, is an accurate predictor of the elastic properties of gas-hydrate-bearing sands. Hydrates are assumed to be part of the dry frame, reducing the original porosity of the rock (ϕ) by the volumetric concentration of hydrate in the rock (C_h) to $\bar{\phi} = \phi - C_h$. The volumetric concentration of hydrate in the pore space or gas hydrate saturation is given by $S_h = C_h/\phi$. The fraction of hydrate in the rock when considered as an extra component of the solid phase is then:

$$\overline{f_h} = \frac{C_h}{1-\bar{\phi}}. \tag{8.1}$$

The fraction of the i^{th} mineral constituent in the solid phase, after assuming the

hydrate is also an extra component of the solid phase, is

$$\overline{f_i} = \frac{f_i(1-\phi)}{1-\bar{\phi}}, \tag{8.2}$$

where f_i is the original volumetric fraction of the i^{th} mineral constituent of the rock.

The elastic constants of the solid phase are then computed using the Hill (1952) average formula:

$$K = \frac{1}{2}\left[\left(\sum_{i=1}^{m} \bar{f}_i K_i + \bar{f}_h K_h\right) + \left(\sum_{i=1}^{m} \bar{f}_i / K_i + \bar{f}_h / K_h\right)^{-1}\right],$$
$$G = \frac{1}{2}\left[\left(\sum_{i=1}^{m} \bar{f}_i G_i + \bar{f}_h G_h\right) + \left(\sum_{i=1}^{m} \bar{f}_i / G_i + \bar{f}_h / G_h\right)^{-1}\right], \tag{8.3}$$

where m is the number of mineral constituents, K_i and G_i are the bulk and shear moduli of the i^{th} mineral constituent, respectively, and K_h and G_h are the bulk and shear moduli of the gas hydrate, respectively (see Table 8.1 for the values for quartz, clay, hydrate, methane gas and water). The density of the solid phase is calculated as follows:

$$\rho = \sum_{i=1}^{m} \bar{f}_i \rho_i + \bar{f}_h \rho_h \,, \tag{8.4}$$

where ρ_i is the bulk density of the i^{th} mineral constituent and ρ_h is the bulk density of the hydrate.

After redefining the properties of the frame to include the gas hydrate as one more mineral component, Cordon et al. (2006) employed the Dvorkin et al. (1999) model for high-porosity, ocean-bottom sediments, also called “soft sand model.” This model

assumes that, at the critical porosity ϕ_C, the effective bulk K_{HM} and shear G_{HM} moduli of the dry rock frame are given by the Hertz-Mindlin contact theory (Mindlin, 1949):

$$K_{HM} = n\frac{1-\phi_C}{12\pi}S_N, \quad G_{HM} = n\frac{1-\phi_C}{20\pi}\left(S_N + \frac{3}{2}S_T\right) \tag{8.5}$$

In Equation 8.5, n is the average number of contacts per grain in the sphere pack (six to nine from Dvorkin and Nur, 1996). S_N is the normal and S_T is the tangential contact stiffness between two spherical elastic grains of radius R:

$$S_N = \frac{4aG}{1-\nu}, \quad S_T = \frac{8aG}{2-\nu}, \tag{8.6}$$

where ν is the Poisson's ratio of the solid phase.

If P is the differential pressure, the radius of the contact circle between the two grains, a, is given by:

$$a = R\left[\frac{3\pi(1-\nu)}{2n(1-\phi_C)G}P\right]^{1/3}. \tag{8.7}$$

The expression for tangential stiffness S_T in equation (8.6) is valid only if there is perfect adhesion between the grains. To account for possible slippage at the grain interface, an ad hoc reduction factor λ was introduced, and S_T is replaced by S_T/λ in equation (8.5).

The bulk and shear moduli of the dry frame for porosity below critical is computed using the modified lower Hashin-Shtrikman (H-S) bound:

$$K_{Dry} = \left[\frac{\frac{\phi}{\phi_c}}{K_{HM} + \frac{4}{3}G_{HM}} + \frac{1 - \frac{\phi}{\phi_c}}{K + \frac{4}{3}G_{HM}} \right]^{-1} - \frac{4}{3}G_{HM},$$

$$G_{Dry} = \left[\frac{\frac{\phi}{\phi_c}}{G_{HM} + Z} + \frac{1 - \frac{\phi}{\phi_c}}{G + Z} \right]^{-1} - Z, \tag{8.8}$$

$$Z = \frac{G_{HM}}{6}\left(\frac{9K_{HM} + 8G_{HM}}{K_{HM} + 2G_{HM}} \right).$$

If the rock is saturated with a fluid of bulk modulus K_f, the shear modulus G_{Sat} is equal to that of the dry frame, and the bulk modulus K_{sat} is obtained using Gassmann's (1951) expression:

$$K_{Sat} = K \frac{\phi K_{Dry} - (1+\phi)K_f K_{Dry}/K + K_f}{(1-\phi)K_f + \phi K - K_f K_{Dry}/K}. \tag{8.9}$$

The bulk density of the rock saturated with a fluid of density ρ_f is:

$$\rho_b = (1-\bar{\phi})\rho + \bar{\phi}\rho_f. \tag{8.10}$$

The elastic-wave velocities are computed as follows:

$$V_P = \sqrt{\frac{K_{Sat} + \frac{4}{3}G_{Sat}}{\rho_b}}, \; V_S = \sqrt{\frac{G_{Sat}}{\rho_b}}. \tag{8.11}$$

Elastic moduli and density of components of hydrate-bearing sandstones			
Component	Bulk Modulus (GPa)	Shear Modulus (GPa)	Density (g/cc)
Quartz	36.60	45.00	2.650
Clay	21.00	7.00	2.580
Methane Hydrate	7.40	3.30	0.910
Brine	2.37	0.00	1.027
Methane Gas, G=0.55	0.02	0.00	0.080

Table 8.1: Elastic moduli and density of components of hydrate-bearing sandstones.

8.4 Resistivity Modeling

Gas hydrates are almost perfect electrical insulators when compared to saline pore waters (Riedel et al., 2006). Log-measured resistivity of massive gas hydrates is around 175 ohm m (Matthews, 1986). Hence, we may use Archie's (1942) equation or other similar empirical formulas relating porosity, resistivity and saturation to compute the amount of pore water present in the rock.

For clean sandstones, Archie's (1942) empirical equation is the most commonly used to model the formation resistivity (R_t) as a function of the connate water resistivity (R_W), water saturation (S_W) and porosity (ϕ):

$$\frac{R_t}{R_W} = \frac{a}{\phi^m {S_W}^n}, \tag{8.12}$$

where *a*, *m* and *n* are empirical constants chosen depending on the lithology; alternatively, they can be determined for a particular dataset using the Pickett (1972) cross-plot technique (see Table 8.2).

Typical values for parameters in Archie's equation		
Lithology/Site	*a*	*m*
consolidated sandstones	0.81	2.00
unconsolidated sandstones	0.62	2.15
Average sands	1.45	1.54
shaly sands	1.65	1.33
clean granular rock	1.00	2.05-ϕ
Mallik 2L-38, Mackenzie Delta, Lee and Collett (2001), n=1.94	1.02	1.95
Cascadia Margin, offshore Vancouver Island, Riedel et al. (2006), n=1.5-2.2	1.0-2.5	1.5-3.0
Blake Ridge, offshore South Carolina, Collett and Ladd (2000), n=1.94	1.05	2.56
NW Eileen, offshore Alaska, Matthews (1986)	1.00	2.58

Table 8.2: Typical values of parameters *a* and *m* in Archie's equation for different lithologies (Hacikoylu et al., 2006), and from different previous studies in areas containing gas hydrate.

Pickett's (1972) method consists of plotting porosity versus deep resistivity in log-log space, and finding a linear fit such that: $ln(R_t/R_W)=-m\ ln(\phi)+[ln(a)-n\ ln(S_W)]$. Using a sample for which $S_W=1$, we can find the values of *a* and *m* from the slope and intercept of a linear fit. The empirical constant *n* is generally assumed to be a value close to 2, but it actually depends on the grain size, sorting and gas-hydrate saturation itself (Spangenberg, 2001). Pearson et al. (1983), using laboratory data, determined *n* values for samples containing brine and ice; these values are 2.17 for sandstone, 1.83

for limestone, 1.72 for unconsolidated material, and 1.94 as a mean value. Lee and Collett (2001), and Collett and Ladd (2000) use this mean value of n = 1.94 to compute gas-hydrate saturation.

Assuming there are only water and gas hydrate filling the pore space, gas-hydrate saturation is computed from the water saturation estimate as $1\text{-}S_W$. Gas can dissociate from the hydrate due to a drop in pressure during drilling. Previous studies in the Blake Ridge area, using sonic well logs and surface reflection seismic data (e.g., Lu and McMechan (2004) and Guerin et al. (1999)) have suggested that hydrates and free gas may coexist in reservoir conditions. If there were free gas in the hydrate-bearing interval corresponding to gas saturation, S_G, the hydrate saturation would be $1\text{-}S_W\text{-}S_G$.

Salinities of pore water in gas-hydrate zones are highly variable, and they seem to decrease as gas-hydrate concentration increases. During the formation of gas hydrates, salt ions are excluded. When the gas hydrates dissociate while drilling, fresh water is released; therefore, water salinity from gas-hydrate–bearing intervals is lower than the water salinity from brine-saturated intervals (Prensky, 1995). The salinity of brine from cores drilled in intervals with high gas-hydrate saturation at Mackenzie Delta, Canada is between 4,000 and 10,000 ppm NaCl equivalent concentration, while the salinity of brine measured from cores with low gas-hydrate concentration from the same location is between 26,000 and 60,000 ppm NaCl equivalent concentration (Winters et al., 2000).

As a result, we found that the resistivity of pore brines below permafrost areas at Mackenzie Delta, Canada may have large variations at borehole locations, ranging

from 0.15 to 2 ohm m. These water resistivity values are obtained by assuming a hydrate reservoir temperature of 15 Celsius degrees as in Cordon et al. (2006), and using the water resistivity values from the Schlumberger Gen-6 chart for the extreme water salinity values, 60,000 and 4,000 ppm NaCl equivalent concentration.

8.5 Application to well log data

The first application shown here is on a data set recorded over gas-hydrate–bearing sediments deposited below permafrost at the Arctic Mallik reservoir, at the Mackenzie Delta, Canada. The two wells are called: Mallik 2L-38 and Mallik 5L-38. Using the gamma-ray log and mud logs available, estimates of lithologic volumetric concentrations are computed. Then, density and these lithology estimates are used to estimate porosity. Water saturation (S_W) was estimated using Archie's (1942) equation, and gas-hydrate saturation was assumed to be $1\text{-}S_W$. Hydrate saturation values obtained were around 90%. The empirical parameters used in Archie's (1942) equation are: $a = 1$, $m = 2$ and $n = 2$ (very similar to those from Lee and Collett (2001) given in Table 8.1). We determine a formation water resistivity $R_W = 0.25$ ohm·m, using the Pickett (1972) cross-plot technique. This value means that water salinity is 35,000 ppm. These hydrate saturation values of around 90% agree with previous studies, which derived saturation from elastic velocity and attenuation, electric resistivity, and water salinity data (Chand and Minshull, 2004; Collett and Lee, 2000).

Figure 8.1 shows the normalized resistivity versus acoustic impedance well-log data for the two Mallik wells, color-coded by gas-hydrate saturation and by porosity. These data are plotted over a template showing the possible solutions for a clean

sandstone, using Archie's equation (1942) to model resistivity and the Cordon et al. (2006) formulation to model the acoustic impedance, also color-coded by the porosity and saturation used in these models. We observe a very good match of this dataset with these models; therefore, given acoustic impedance and resistivity, we could predict porosity and saturation for a gas-hydrate–bearing clean sandstone. We made this prediction for one of the Mallik wells, 2L-38, and we found, as expected, a good estimate of the gas hydrate concentration using only acoustic impedance and resistivity as inputs (see Figure 8.2). The estimate of porosity using density and mineralogical content as inputs is in black. The estimate of gas hydrate saturation using only resistivity as input is in black. The estimates obtained inverting for porosity and saturation using both acoustic impedance and resistivity as inputs, and using Cordon et al. (2006) and Archie (1942) equations, are shown in red. The peaks where there is not good agreement of the inversion results with the estimates from density and resistivity are where coal layers are present.

Sediments from the Nankai Trough are an example of more poorly sorted gas-hydrate–bearing sandstones. Grain sorting is apparently related to the gas-hydrate saturation. The intervals with high gas-hydrate saturation are better sorted than those with low or zero gas-hydrate saturation. This may be due to the fact that in better sorted sediments, which have relatively high permeability, there was more pore space and transport freedom for gas hydrate to form, whereas with increased clay content, porosity and permeability are lower, and less pore space and transport freedom are available for hydrates to deposit.

Mallik 2L-38 well

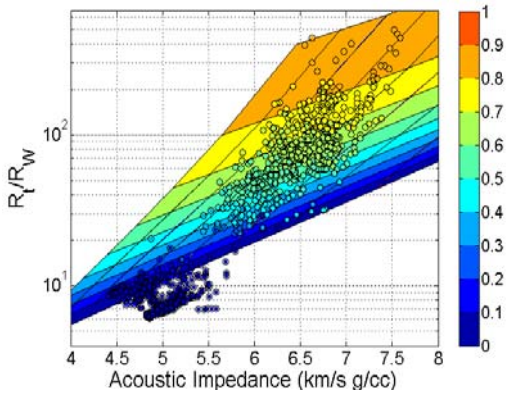

(a)

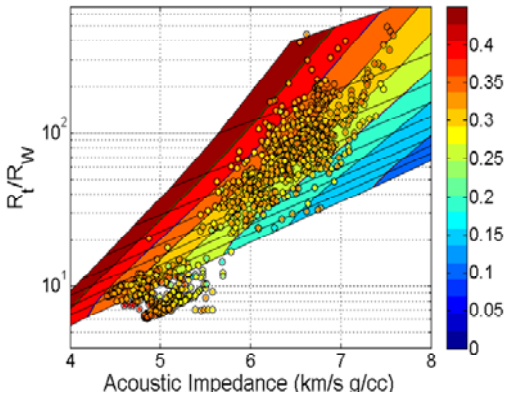

(b)

Mallik 5L-38 well

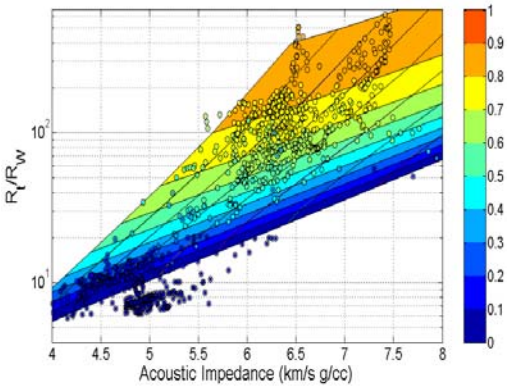

(c)

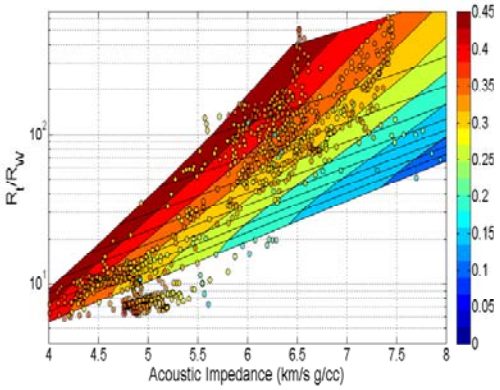

(d)

Figure 8.1: Normalized resistivity versus acoustic impedance color-coded by (a) and (c) gas hydrate saturation, and (b) and (d) porosity for Mallik (a) and (b) 2L-38, and (c) and (d) 5L-38 wells. Template of modeled resistivity and acoustic impedance using Archie (1942) and Cordon et al. (2006) are in the background.

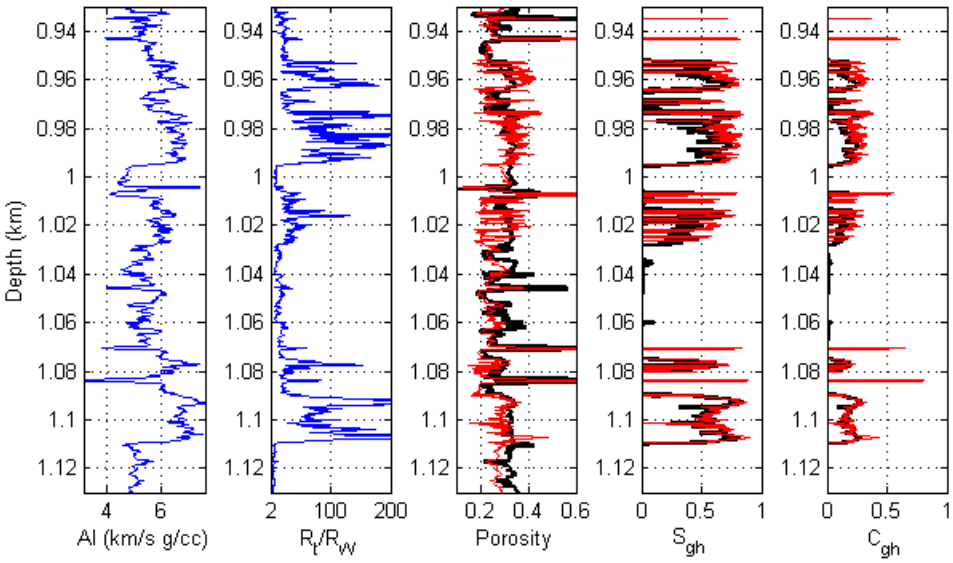

Figure 8.2: Mallik 2L-38 well. The logs shown from left to right are: (1) acoustic impedance (AI); (2) normalized deep resistivity (Rt/Rw); (3) porosity; (4) gas-hydrate saturation; and (5) gas-hydrate concentration (porosity multiplied by gas hydrate saturation). The estimate of porosity using density and mineralogical content as inputs is in black. The estimate of gas-hydrate saturation using only resistivity as input is in black. The estimates obtained inverting for porosity and saturation using only acoustic impedance and resistivity as inputs, and using Cordon et al. (2006) and Archie (1942) for the modeling, are shown in red. The peaks where there is poor agreement of the estimates in red with those in black are where coal layers are present.

Figure 8.3 shows acoustic impedance versus resistivity data from this well and another well from the Nankai Trough, plotted over the template of normalized resistivity versus P-wave impedance, color-coded by saturation on the left and by porosity on the right. The clay content in this template varies from 0 at the top to 0.6 at the bottom. We observe that the data points with the larger gas-hydrate saturation can be modeled assuming a clean sandstone reservoir (Figure 8.3a and 8.3b). However, decreasing gas-hydrate saturation corresponds to increasing clay content. To model the layers with lower gas-hydrate saturation, we must assume higher clay

content (Figure 8.3c and 8.3d). This assumption favorably agrees with the gamma-ray measurements and a published lithologic column for this well by Hato et al. (2006).

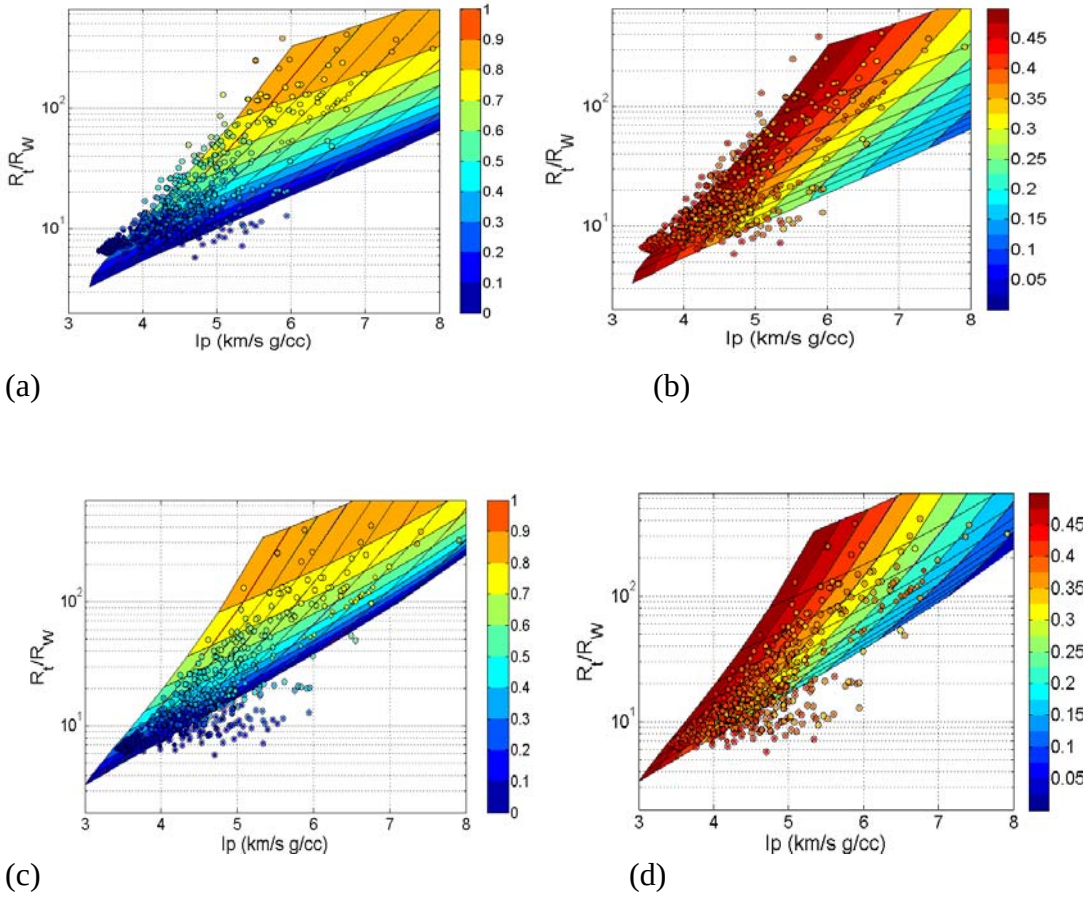

Figure 8.3: Normalized resistivity versus acoustic impedance color-coded by (a) and (c) gas hydrate saturation, and (b) and (d) porosity for two Nankai wells. Template of modeled resistivity and acoustic impedance using Archie (1942) and Cordon et al. (2006) are in the background assuming: (a) and (b) zero clay content; and (c) and (d) 60 % clay content.

8.6 Modeling Catalogue

Using well-log data, we showed that the elastic model by Cordon et al. (2006) and the resistivity model by Archie (1942), as described in the elastic and resistivity

modeling sections above, accurately describe hydrate-bearing sediments. In this section, we will use these models to create a catalogue of P-wave impedance and resistivity response for gas-hydrate–bearing sediments. Both the P-wave impedance and resistivity are highly sensitive to porosity and saturation. P-wave impedance depends on the hydrate saturation to a lesser degree than does resistivity (Figure 8.4).

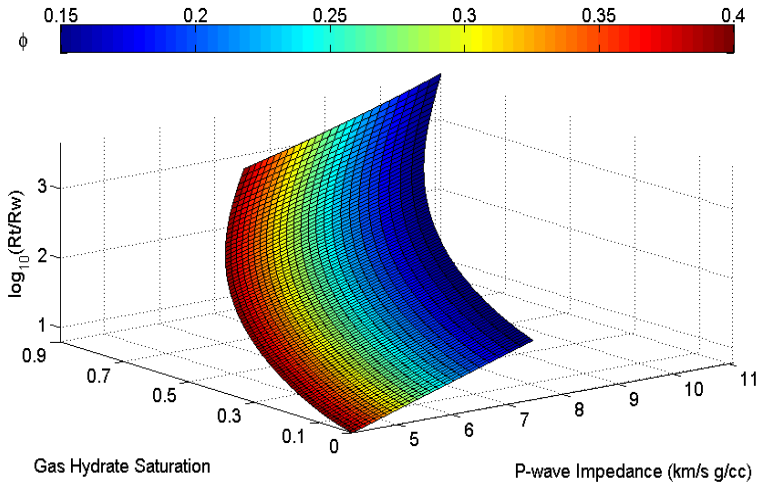

Figure 8.4: Normalized resistivity versus P-wave Impedance and gas hydrate saturation color-coded by porosity in a gas-hydrate sand, characterized using the Cordon et al. (2006) modeling approach.

Different combinations of porosity and hydrate saturation will still give the same P-wave impedance response (Figure 8.5). To discriminate saturation from porosity using elastic data, one may include Poisson's ratio in the analysis. Having Poisson's ratio for the hydrate-bearing sandstone will limit the possible porosity and saturation values of the hydrate layer and, therefore, its resistivity (Figure 8.6).

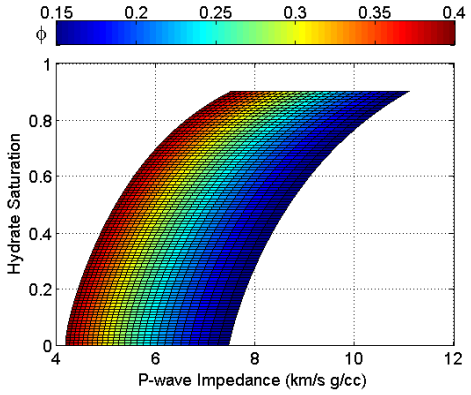

Figure 8.5: Same as 8.4, but a map view from above. The hydrate saturation versus P-wave impedance crossplot is color-coded by porosity.

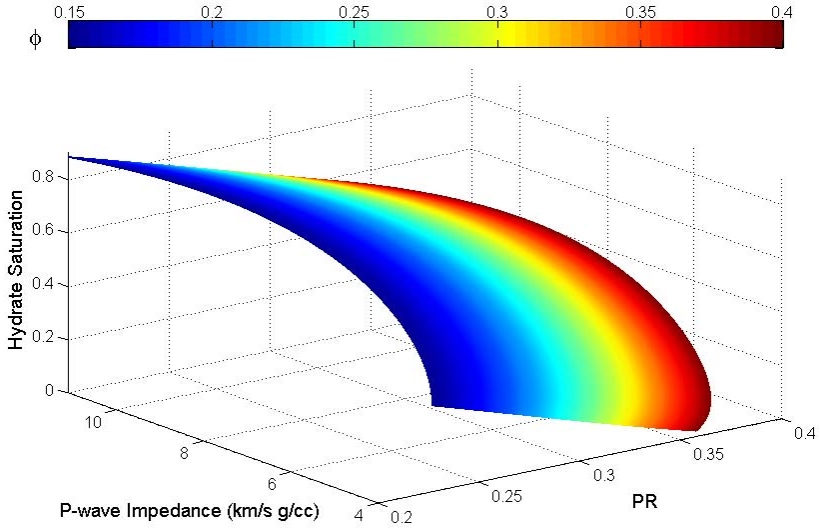

Figure 8.6: Hydrate saturation versus P-wave impedance and Poisson's ratio (PR) color-coded by porosity.

After these observations, the next step was to take a closer look not at the hydrate layer alone, but at the interface of the hydrate and free-gas–saturated layers, where the BSR is found and the strongest seismic response is observed. Can we predict porosity

and saturation, and therefore resistivity in the hydrate layer from the seismic reflectivity in the hydrate–free-gas interface?

We create a model having a 2m-thick 90% hydrate-saturated sand, sandwiched between a shale and a 15% gas-saturated sand. We assume the shale layer to have 40% porosity and 90% clay content, and the sand to have 40, 35, 30, and 20% porosity. The zero-offset seismic response to changing porosity at the base of the hydrates is weak but observable (Figure 8.7). However, if we keep porosity constant at 40%, and change only the saturation of hydrate from 90% to 60, 30, and 0%, the effect is observed in the seismic data only as we look at the AVO response at the hydrate–gas-sand interface, and not at normal incidence, where all seismograms are very similar (Figure 8.8).

Hence, seismic reflectivity plots at different incidence angles for the hydrate–gas-sand interface can help to discriminate porosity and saturation in the hydrate sand, but only if we have excellent seismic resolution and can actually resolve the elastic properties of the hydrate and gas sand. Figure 8.9 shows that using P-P reflectivity at normal incidence and at 30 degrees, we could discriminate the product of porosity and saturation.

A simple way to obtain the resistivity of the hydrate layer would be to compute resistivity for these porosity times saturation values (Figure 8.10), assuming a resistivity model (e.g., a=1, m=2, and n=2). When we plot these normalized resistivity values on top of the normal incidence PP reflectivity versus the PP reflectivity at an incident angle of 30 degrees (Figure 8.11), we see that if the hydrate layer is

resolvable, we can predict from the seismic data an initial resistivity model to use in the hydrates for an EM data inversion. We can also use a gradient-versus-intercept plot, color-coded by resistivity (Figure 8.12). PP reflectivity at zero offset or the intercept at the hydrate–gas interface is negative, and becomes less negative as the offset increases (positive gradient). Hence, AVO analysis can be used to obtain an initial estimate of the saturation and porosity (and therefore the resistivity) in the hydrate layer, if the hydrate-bearing layer is resolvable from seismic data.

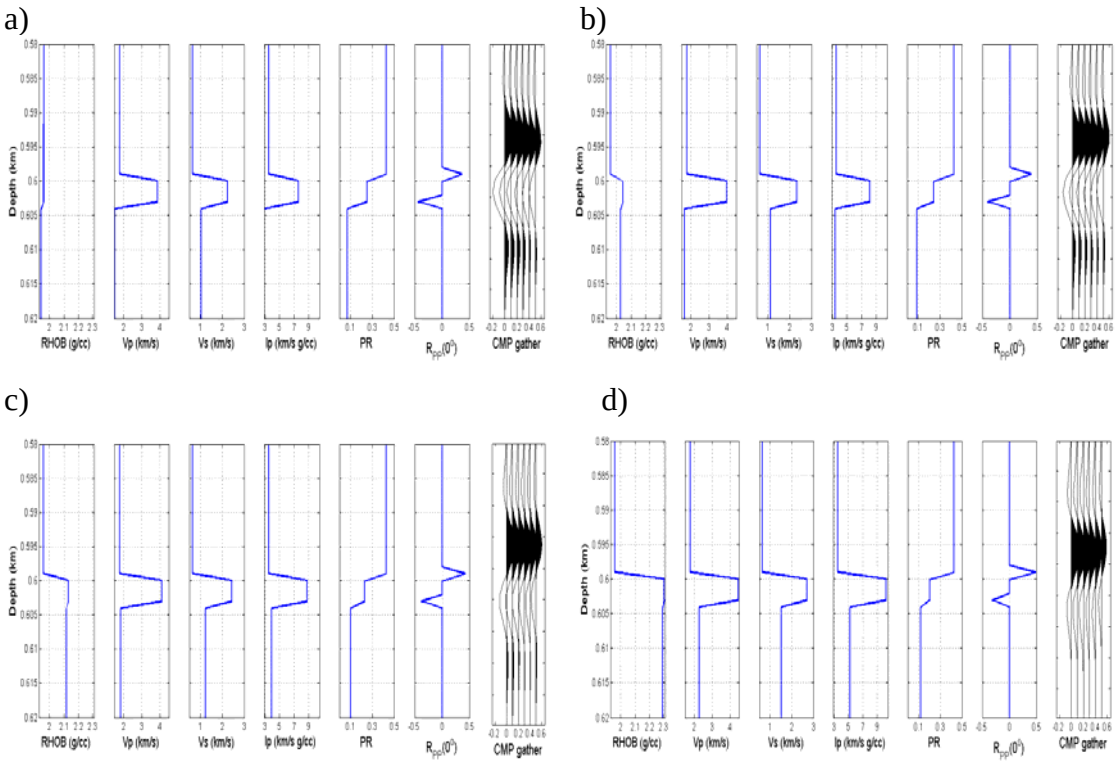

Figure 8.7: Two-meter-thick, 90% hydrate-saturated sand, sandwiched between a shale and a 15% gas-saturated sand. Shale has 40% porosity and 90% clay content. Sand has (a) 40%, (b) 35%, (c) 30% and (d) 20% porosity. From left to right: density, P-wave velocity, S-wave velocity, P-wave impedance, Poisson's ratio, PP reflectivity at normal incidence, and CMP gather (maximum offset shown is 40 degrees).

From the seismograms computed for a time sampling interval of 2 ms (Figure 8.7 and 8.8), considering a hydrate layer 2 m thick, we observe that we cannot resolve the top and bottom of the hydrate layer separately; both events are interfering, causing a response that will depend not only on the sand properties but also on the properties of the shale above.

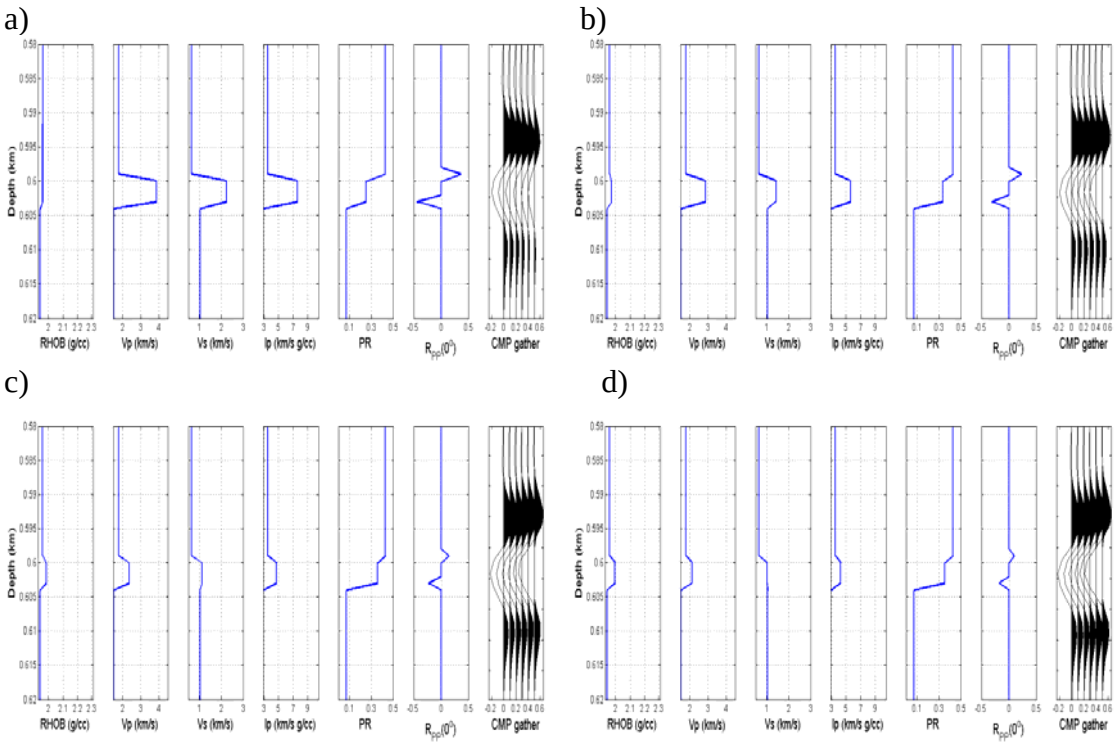

Figure 8.8: Two-meter-thick 40% porosity hydrate-saturated sand, sandwiched between a shale and a 15% gas-saturated sand. Shale has 40% porosity and 90% clay content. Sand has (a) 90%, (b) 60%, (c) 30% and (d) 0% hydrate saturation. From left to right: density, P-wave velocity, S-wave velocity, P-wave Impedance, Poisson's ratio, PP reflectivity at normal incidence, CMP gather (maximum offset shown is 40 degrees).

Therefore, if we invert the seismic data for reflectivity, we obtain a plot of PP reflectivity at normal incidence and at 30 degrees versus hydrate saturation, shown in Figure 8.13. This result is quite different from that in Figure 8.9, where we did not

account for seismic resolution but plotted the actual values of the model. As hydrate content increases, the normal-incidence reflection coefficient becomes less negative, while the separation for the 30-degree reflection coefficient values becomes larger, making it possible to predict the porosity of the hydrate layer in that case. This case assumes that the shale cap is a 40% porosity soft shale; however if the shale has 20% porosity, then it would be very difficult to distinguish between a water-saturated and a 90% hydrate-saturated sandstone with 15% porosity. The same would be true for a 15% hydrate-saturated versus a 90% hydrate- saturated sandstone with 40% porosity (Figure 8.14). Therefore, our ability to predict saturation in the hydrate-bearing sand will depend on its porosity.

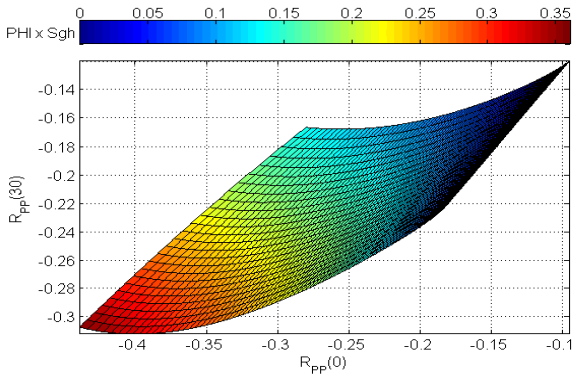

Figure 8.9: PP reflectivity at 30 degrees versus PP reflectivity at 0 degrees for the base of the hydrates, assuming a 15% gas-saturated sand underneath, color-coded by the product of porosity and hydrate saturation.

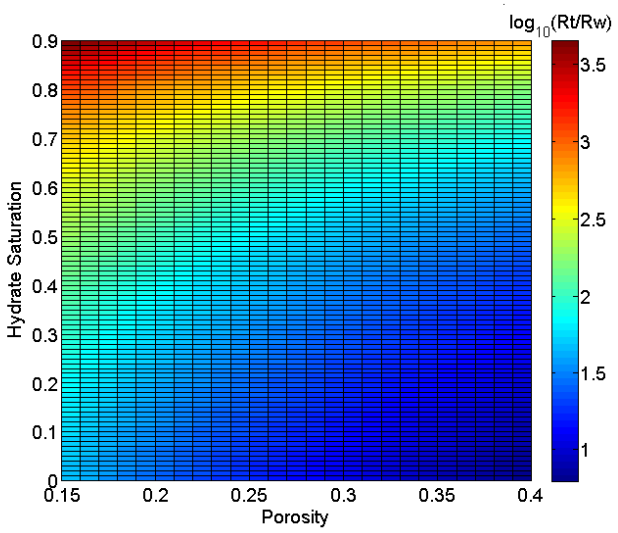

Figure 8.10: Hydrate saturation versus porosity, color-coded by the logarithm of normalized resistivity, using Archie's model used before in Mallik Arctic wells (a=1, m=2).

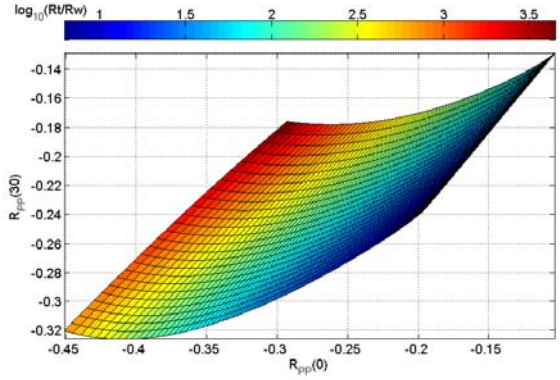

Figure 8.11: PP reflectivity at 30 degrees offset versus normal-incidence PP reflectivity at the interface of gas hydrate and gas sand, color-coded by the logarithm of normalized resistivity, using same Archie's model as in Figure 8.10.

From this modeling, we learned that our ability to predict the hydrate-bearing sand resistivity depends on its thickness; at thicknesses below seismic resolution, it will strongly depend on the overburden properties, particularly those of the shale acting as a cap for the hydrate sand.

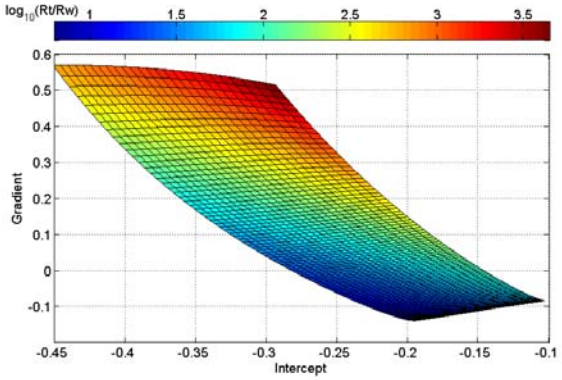

Figure 8.12: Gradient versus intercept at the interface of gas hydrate and gas sand, color-coded by the logarithm of normalized resistivity, using same Archie's model as in Figure 8.10.

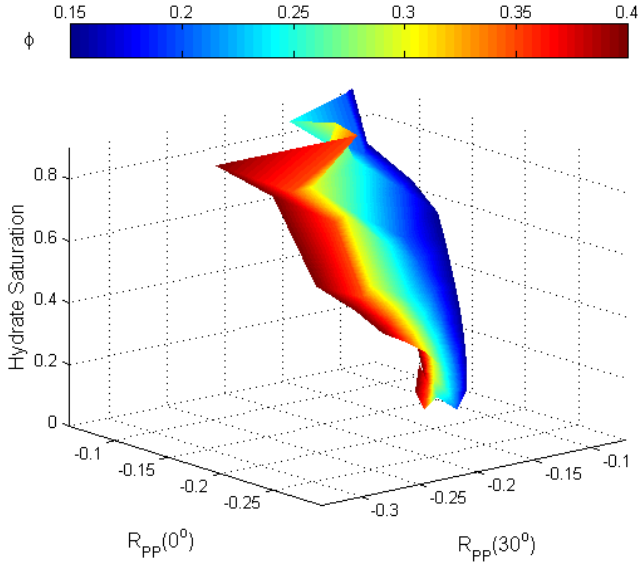

Figure 8.13: Hydrate saturation versus PP Reflectivity at zero degrees versus PP Reflectivity at 30 degrees for the base of the hydrates, assuming a 15% gas-saturated sand underneath, color-coded by porosity. A shale of 40% porosity is assumed above, and the hydrate layer is assumed to be 2 m thick.

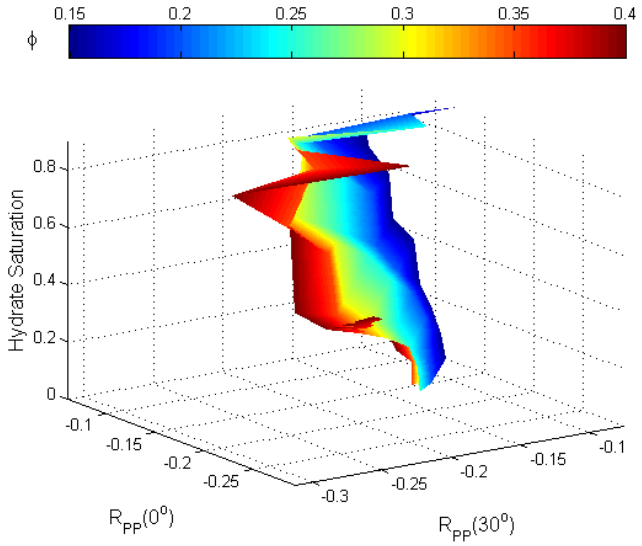

Figure 8.14: Hydrate saturation versus PP Reflectivity at zero degrees versus PP Reflectivity at 30 degrees for the base of the hydrates, assuming a 15% gas-saturated sand underneath, color-coded by porosity. A shale of 20% porosity is assumed above, and the hydrate layer is assumed to be 2 m thick.

8.7 Conclusions

From our analysis, we find that the elastic properties of gas-hydrate–bearing sandstones can be modeled using the soft-sand model by Dvorkin et al. (1999), and assuming that gas hydrate acts as part of the load-bearing matrix as in Cordon et al. (2006). In the same manner, electrical resistivity for the gas-hydrate–bearing sandstones can be modeled using Archie's equation (1942).

Normalized resistivity versus P-wave impedance plots may be very useful to predict reservoir properties, such as porosity and saturation for a gas-hydrate reservoir. Since, in the normalized resistivity–P-wave impedance domain, there is a clear separation of intervals with high gas-hydrate saturation from intervals with low gas-hydrate saturation, even for poorly sorted reservoirs. Therefore; acquiring surface

reflection seismic and controlled-source electromagnetic data over a gas-hydrate reservoir could prove to be very valuable for reservoir characterization.

Our ability to predict porosity and saturation of the hydrate-bearing layer from seismic data alone is highly dependent on its thickness and the properties of the overburden, as we show in our modeling. It is not an impossible task if we have some well-control data that can indicate the appropriate models and properties to use for the overburden. Once we estimate porosity and saturation from the seismic data, we can use these estimates to generate an initial resistivity model for the hydrates to use as a constraint in an EM data inversion. Predicting the presence of a reservoir below hydrates is difficult, and it can be very useful to have an initial resistivity model to constrain the EM properties of the hydrate layer before attempting to invert for the conductivity below.

Chapter 9
Conclusions

The concept of P-wave impedance and resistivity templates is introduced as a tool to estimate porosity and saturation from well log data. Adequate elastic and resistivity models, according to the lithology, cementation, fluid properties must be chosen to construct these templates. These templates can be upscaled to seismic and CSEM scale using Backus average for seismic data, and total resistance for CSEM data.

It is important to be aware of the limitations of lateral and vertical resolution of CSEM data. If the lateral dimensions of the reservoir are smaller or equal to the depth of burial, we may not be able to detect the reservoir, even if we use the appropriate template. This is because when we create the template and upscale it, we are only doing a 1D modeling.

We measured velocity and resistivity in Fontainebleau sandstones in the laboratory, and derived an empirical relation between these two properties at 40MPa effective pressure, which is around 3 km depth at normal pressure gradients. We were not able to test if this relation could be used at well or field data scales (once

appropriate upscaling was applied), since we did not have a field dataset over a stiff sandstone reservoir.

We also found that the resistivity versus P-wave velocity data at 40MPa falls between the Faust (1953) relationship, which works as an upper bound, and the Hacikoylu et al. (2006) expression, which acts as a lower bound.

A relationship between velocity and resistivity laboratory data was also found for a set of carbonates. This expression was not linear, but quadratic, which reveals that velocity and resistivity in this case are not primarily a function of porosity, as in the case of Fontainebleau sandstones. There are other factors that influence this relationship, which include pore geometry, and amount of micritic cement. We observed that the expression is almost linear, but it deviates as we approach lower resistivities. This deviation can be explained by the presence of stiff pores such as moldic or intra-granular pores, which causes high velocity but low resistivity values when water-saturated. In the same way, the effect of micrite cement on velocity is stronger than its effect on resistivity, and that also is responsible for some of the scatter that we observe.

We also modeled both velocity and resistivity using the self-consistent approximation with the same pore or inclusion geometries in both carbonate and sandstone laboratory datasets. In the case of carbonates, we found that we had to include needle-like pores to explain the low resistivity but high velocities. Needle is one of the geometries that allow us to have connected stiff pores. However, we also found that a fraction of compliant pores also had to be included in order to explain the

velocity measurements on the carbonate dataset. Self-consistent model also approximated well the velocity and resistivity laboratory measurements on the Fontainebleau sandstones, using similar aspect ratios for both the velocity and the resistivity.

As far as semi-empirical and empirical models, we observed how the stiff-sand model fit well the Fontainebleau data at 40MPa, including S-wave velocities. Raymer-Hunt-Gardner relation also did a good job at predicting P-wave velocity. Archie's equation with cementation exponent between 1.6 and 2.1 fits the resistivity measurements on the Fontainebleau sandstones. These two relationships can be combined to create a resistivity – P-wave velocity transform for this dataset.

When we attempted to use CSEM data to limit the shallow and low-frequency acoustic impedance trend for seismic inversion, we found that an appropriate elastic and resistivity models must be chosen in order to have a good prediction of acoustic impedance given resistivity. These expressions can be calibrated using well data given particular emphasis to the overburden. We also found at this North Sea reservoir that conventional cross-property relations such as Faust (1953) and Hacikoylu et al. (2006) can over predict the acoustic impedance in friable shaly sediments at shallow depths. In the stiffer deeper lithologies, we observe that Hacikoylu et al. (2006) underpredicts, as expected from our laboratory study in Fontainebleau sandstones. If no well log data is available in the shallow section, using the CSEM-derived resistivity data and an adequate cross-property relation (for example, one based on soft-sand model and Archie's equation) can be a good approach to predict the initial low

frequency shallow acoustic impedance model. Validation tests showed that using the background trend from CSEM data as a constraint in impedance inversion can give a better fit to the acoustic impedance.

As part of our analysis of gas hydrate bearing sandstones, we found that normalized resistivity versus P-wave impedance templates can also be useful to predict reservoir properties, such as porosity and saturation for a gas-hydrate reservoir at well log scale. Porosity and saturation prediction of the hydrate-bearing layer from seismic data alone is highly dependent on its thickness and the properties of the overburden, and requires well-control data that can indicate the appropriate models and properties to use for the overburden. However, it would be interesting to test using a resistivity model obtained from seismic data as the initial input for a CSEM inversion on a gas-hydrate-bearing sandstone.

References

Aligizaki, K, 2006, Pore structure of cement-based materials: testing, interpretation and requirements: Taylor & Francis.

Anderson, C., A. Long, A. Ziolkowski, B. Hobbs, and D. Wright, 2008, Multi-transient EM technology in practice: First break, 26, 93-102.

Andreis, D. and L. MacGregor, 2008, Controlled-source electromagnetic sounding in shallow water: Principles and applications: Geophysics, 73, 1, F21-F32.

Archie, G. E., 1942, The electrical resistivity log as an aid in determining some reservoir characteristics: Trans. Americ. Ints. Mineral. Met., 146, 54-62.

Avseth, P., J. Dvorkin, G. Mavko, and J. Rykkje, 2000, Rock physics diagnostics of North Sea sands: Link between microstructure and seismic properties: Geophysics Research Letters, 27, 2761-2764.

Avseth, P., T. Mukerji, and G. Mavko, 2005, Quantitative Seismic Interpretation. Applying Rock Physics Tools to reduce Interpretation Risk: Cambridge University Press.

Baechle, G., A. Colpaert, G. Eberli, and R. Weger, 2007, Modeling velocity in carbonates using dual porosity DEM model: SEG Annual Meeting Expanded Abstracts, 1589-1592.

Berryman, J. G., and G. W. Milton, 1988, Microgeometry of random composites and porous media: Journal of Physics D, 21, 87–94.

Berryman, J., 1995, Mixture of Rock Properties: Rock Physics and Phase Relations: A Handbook of Physical constants: American Geophysical Union Reference Shelf 3, 205.

Borgomano, J., The Upper Cretaceous carbonates of the Gargano-Murge region southern Italy: A model of platform-to-basin transition: AAPG Bulletin, 84, 10, 1561-1588.

Bosellini, A., M. Morsilli, and C. Neri, Long-term event stratigraphy of the Apulia platform margin: Journal of Sedimentary Research, 69, 6, 1241-1252.

Bourbie, T., and B. Zinszner, 1985, Hydraulic and acoustic properties as a function of porosity in Fontainebleau sandstone: Journal of Geophysical Research, v. 90, B13, 11524-11532.

Brito Dos Santos,W. L., T. J. Ulrych, and O. A. L. De Lima, 1988, Anew approach for deriving pseudovelocity logs from resistivity logs: Geophysical Prospecting, 36, 83–91.

Bruggeman, D., 1935, Berechnung verschiedener physikalischer konstanten von heterogenen substanzen, Ann. Physik. (Leipzig), 24, 636-679.

Brunauer, S., P. Emmett, and E. Teller, 1938, Adsorption of gases in multimolecular layers: J. of the Am. Chem. Soc., 60, 2, 309-319.

Carcione, J., B. Ursin, and J. Nordskag, 2007, Cross-property relations between electrical conductivity and the seismic velocity of rocks: Geophysics, 72, E193-E204.

Carman, P.C., 1961, L'écoulement des gaz à travers les milieux poreux. Bibliothèque des Sciences et des Techniques nucléaires, P.U.F., 52.

Carrara, E., A. Mazzacca, R. Pece, N. Roberti, and T. Vanorio, 1999, Evaluation of porosity and saturation degree by laboratory joint measurements of velocity and resistivity: A model improvement: Pure Applied Geophysics, 154, 211-255.

Castagna, J., M. Batzle, T. Kan, 1993, Rock Physics – The link between rock properties and AVO response: Offset-Dependent Reflectivity – Theory and Practice of AVO Analysis, by J. Castagna and M. Backus. Investigations in Geophysics, 8, SEG, Tulsa, OK, 135-171.

Chand, S and T. Minshull, 2004. The effect of hydrate saturation on seismic attenuation – A case study for Mallik 2L-38 well data, Mackenzie delta, Canada, Geophysical Research Letters 31, L14609.

Chave, A. D. and C.S. Cox, 1982, Controlled Electromagnetic Sources for Measuring Electrical Conductivity Beneath the Oceans 1. Forward Problem and Model Study: J. Geophys. Res., 87, B7, 5327-5338.

Chopra, S., K. Strack, C. Esmersov, and N. Allegar, 2007, Introduction to this special section: CSEM: The Leading Edge, 26 , 3, 323-325.

Claerbout, J. F., 1985, Imaging the earth's interior, Blackwell Scientific Publ.

Collett T. and J. Ladd, 2000, Detection of gas hydrate with downhole logs and assessment of gas hydrate concentrations (saturations) and gas volumes on the Blake Ridge with electrical resistivity log data: Proceedings of the Ocean Drilling Program, Scientific Results, 164, 179-191.

Collett T. and M.W. Lee, 2000, Reservoir characterization of marine and permafrost associated gas hydrate accumulations with downhole well logs: Annals of New York Academy of Sciences, 912, 51–64.

Connolly, P., 1999, Elastic Impedance, The Leading Edge, 18 , 4, 438-452.

Constable, S., and C. Weiss, 2006, Mapping thin resistors and hydrocarbons with marine EM methods: Insights from 1D modeling: Geophysics, 71 , 2, G43-G51.

Cordon, I., J. Dvorkin, and G. Mavko, 2006, Seismic reflections of gas hydrate from perturbational forward modeling: Geophysics, 71, F165-F171.

Domenico, S. N., 1974, Effect of water saturation on seismic reflectivity of sand reservoirs encased in shale: Geophysics, 39, 6, 759-769.

Domenico, S. N., 1976, Effect of brine-gas mixture on velocity in an unconsolidated sand reservoir: Geophysics, 41, 5, 882-894.

Doyen, P. M., 1988, Permeability, conductivity and pore geometry of sandstones: Journal of Geophysical Research, 93, B7, 7729-7740.

Dragoset, B., and J. Gabitzsch, 2007, Introduction to this special section: Low frequency seismic, The Leading Edge, 26, 1, 34-35.

Durand, C, 2003, Improvement of fluid distribution description during floods by combined use of X-ray CT scan and continuous local resistivity measurements: Symposium of the Society of Core Analysts, France.

Dvorkin, J., M. Gutierrez, and A. Nur, 2002, On the universality of diagenetic trends: The Leading Edge, 21 , 1, 40-43.

Dvorkin, J., and A. Nur, 1996, Elasticity of high-porosity sandstones: Theory for two North Sea datasets, Geophysics, 61, 1363-1370.

Dvorkin, J., M. Prasad, A. Sakai, and D. Lavoie, 1999, Elasticity of marine sediments: GRL, 26, 1781-1784.

Dvorkin, J., and R. Uden, 2004, Seismic attenuation in a methane hydrate reservoir: The Leading Edge, 23, 8, 730-732.

Dvorkin, J., J. Walls, R. Uden, M. Carr, M. Smith, and N. Derzhi, 2004, Lithology substitution in fluvial sand: The Leading Edge, 23 , 2, 108-112.

Faust, L.Y., 1953, A velocity function including lithologic variation: Geophysics, 18, 271-288.

Gal, D., J. Dvorkin, and A. Nur, 1998, A Physical Model for Porosity Reduction in Sandstones: Geophysics, 63, 454-459.

Gassmann, F., 1951, Elasticity of porous media: Uber die elastizitat poroser medien: Vierteljahrsschrift der Naturforschenden Gesselschaft, 96, 1-23.

Gibiansky, L.V., and S. Torquato, 1996, Bounds on the effective moduli of cracked materials: Journal of the Mechanics and Physics of Solids, 44, 233–242.

Gomez, C. T., J. Dvorkin, and G. Mavko, 2008, Estimating the hydrocarbon volume from elastic and resistivity data: A concept: The Leading Edge, 27, 6, 710-718.

Gomez, C. T., and R. H. Tatham, 2006, Sensitivity analysis of seismic reflectivity to partial gas saturation: Geophysics, 72, 3, C45 - C57.

Gonzalez, E., T. Mukerji, G. Mavko, and R. Michelena, 2003, Near and far offset P-to-S elastic impedance for discriminating fizz water from commercial gas: The Leading Edge, 22, 1012.

Greenberg, M. L., and J. Castagna, 1992, Shear-wave velocity estimation in porous rocks; theoretical formulation, preliminary verification and applications: Geophysical Prospecting, 40, 195-209.

Griffiths, D., 1989, Introduction to electrodynamics: Prentice Hall, 2nd edition.

Guerin, G., D. Goldberg, and A. Meltzer, 1999, Characterization of in-situ elastic properties of gas-hydrate-bearing sediments on the Blake Ridge: Journal of Geophysical Research, 104, 17781-17796

Hacikoylu, P., J. Dvorkin, and G. Mavko, 2006, Resistivity-velocity transforms revisited. The Leading Edge, 25, 1006-1009.

Han, D., A. Nur, and D. Morgan, 1986, Effects of porosity and clay content on wave velocities in sandstones: Geophysics, 51, no.11, 2093-2107.

Harris, P., and L. MacGregor, 2006, Determination of reservoir properties from the integration of CSEM, seismic, and well-log data: First Break, 24 , 11, 53-60.

Hato, M., Matsuoka, T., Inamori, T., and Saeki, T., 2006, Detection of methane-hydrate-bearing zones using seismic attributes analysis: The Leading Edge, 25 , no.5, 607-609.

Hausenblas, M., 1995, Stress dependence of the cementation exponent: Society of Core Analysts, paper 9518.

Helgerud, M., J. Dvorkin, A. Nur, A. Sakai, and T. Collett, 1999, Elastic-wave velocity in marine sediments with gas hydrates: Effective medium modeling: Geophysical Research Letters, 26, 2021-2024.

Helgerud, M., 2001, Wave speeds in gas hydrate & sediments containing gas hydrate: A Laboratory & modeling study: Ph.D. Dissertation, Dpt. of Geophysics, Stanford University.

Hill, R., 1952, The elastic behavior of crystalline aggregate: Proc. Physical Soc., London, A65, 349-354.

Jackson, P. D., D. T. Smith, and P. N. Stanford, 1978, Resistivity-porosity-particle shape relationships for marine sands: Geophysics, 43, no.6, 1250-1276.

Jacquin, C.G., 1964, Correlation entre la permeabilite et les characteristiques geometriques du gres de Fontainebleau : Revue Inst. Fr. Petrole, 19, 921.

Jannane, M., W. Beydoun, E. Crase, D. Cao, Z. Koren, E. Landa, M. Mendes, A. Pica, M. Noble, G. Roeth, S. Singh, R. Snieder, A. Tarantola, D. Trezeguet, and M. Zie,1989, Wavelengths of earth structures that can be resolved from seismic reflection data: Geophysics, 54, 906–910.

Johansen, S., T. Wicklund, and H. Amundssen, 2007, Interpretation example of marine CSEM data: The Leading Edge, 26, 3, 348-354.

Johnson, D., T. Plona, and H. Kojima, 1986, Probing Porous Media with 1st Sound, 2nd Sound, 4th Sound and 3rd Sound: Physics and chemistry of porous media-II. In: Banavar, J., J. Koplik, and K. Winkler, (eds) Proceedings of the Second International Symposium on the Physics and Chemistry of Porous Media. AlP Conference Proceedings, 154, 243-277.

Kachanov, M., I. Sevostianov, and B. Shafiro, 2001, Explicit cross-property correlations for porous materials with anisotropic microstructures: Journal of the Mechanics and Physics of Solids, 49, 1–25.

Katz, A.J. and A. H. Thompson, 1986, Quantitative prediction of permeability in porous rock: Phys. Rev. B34, 8179 - 8181.

Knackstedt, M., C. Arns, A. Sheppard, T. Senden, R. Sok, Y. Cinar, A. Olafuyi, W. Pinczewski, G. Padhy, and M. Ioannidis, 2007, Pore scale analysis of electrical resistivity in complex core material: Symposium of the Society of Core Analysts, Canada.

Knight, R., 1991, Hysteresis in the electrical resistivity of partially saturated sandstones: Geophysics, 56, 2139-2147.

Knight, R. and A. Endres, 2005, An Introduction to Rock Physics Principles for Near-Surface Geophysics: Near-Surface Geophysics, Edited by Butler, D. Investigations in Geophysics, 13, Soc. of Expl. Geophys., 31-70.

Landauer, R., 1952, The electrical resistance of binary metallic mixtures: J. Appl. Phys., 23, 779-784.
Lee, M. and T. Collett, 2001, Gas hydrate estimation error associated with uncertainties of measurements and parameters: U.S. Geological Survey bulletin, 2182, 1-8.
Lewis, M., M. Sharma, and H. Dunlap, 1988, Techniques for measuring the electrical properties of sandstone core: Soc. of Petroleum Eng. Ann. Tech. Conf., SPE-18178, 697-703.
Lu, S., and G. McMechan, 2004, Elastic impedance inversion of multichannel seismic data from unconsolidated sediments containing gas hydrate and free gas: Geophysics, 69, no.1, 164-179.
Matthews, M., 1986, Logging characteristics of methane hydrate: The Log Analyst, 27, 26-63.
Mavko, G., 1980, Velocity and attenuation in partially molten rocks: Journal of Geophysical Research, 85, no.B10, 5173-5189.
Mavko, G., and T. Mukerji, 1995, Seismic pore space compressibility and Gassmann's relation: Geophysics, 60, no.6, 1743-1749.
Mavko, G., T. Mukerji, and J. Dvorkin, 1998, The Rock Physics Handbook: Cambridge University Press.
Mavko, G., T. Mukerji, and J. Dvorkin, 1998, The Rock Physics Handbook: Cambridge University Press, 1st Edition.
Mavko, G., T. Mukerji, and J. Dvorkin, 2009, The Rock Physics Handbook: Cambridge University Press, 2nd Edition.
Mavko, G., and A. Nur, 1978, The effect of nonelliptical cracks on the compressibility of rocks: Journ. Geophys. Res, 83, B9, 4459-4468.
Mavko, G., and A. Nur, 1997, The effect of a percolation threshold in the Kozeny-Carman relation: Geophysics, 62, 1480–1482.
Metz, F. and D. Knofel, 1992, Systematic mercury porosimetry investigations on sandstones: Materials and Structures, 25, 127-136.
Milsch, H., G. Blocher, and S. Engelmann, 2008, The relationship between hydraulic and electrical transport properties in sandstones: An experimental evaluation of several scaling models: Earth and Planetary Science Letters, 275, 355-363.
Mindlin, R. D., 1949, Compliance of elastic bodies in contact: Trans. SDME, 71, A-259.
Mukerji, T., J. Berryman, G. Mavko, and P. Berge, 1995, Differential effective medium modeling of rock elastic moduli with critical porosity constraints: Geophys. Res. Lett., 22, 555-558.
Mukerji, T., G. Mavko, and C. Gomez, 2008, Estimating low frequency seismic impedance from CSEM resistivity using cross-property rock physics relations, SEG expanded Abstr.27, 1769.
Mukerji, T., G. Mavko, and C. Gomez, 2009, Cross-property rock physics relations for estimating low-frequency seismic impedance trends from electromagnetic resistivity data, The Leading Edge, 28, 94.
Murphy, W. F., 1984, Acoustic measures of partial gas saturation in tight sandstones: Journal of Geophysical Research, V. 89, B13, 11,549-11,559.
Nur, A. and G. Simmons, 1969, The effect of saturation on velocity in low porosity rocks: Earth and Planet Sc. Letters. Amsterdam, 7, 183-193.
Nur, A. and Z. Wang, 1989, Seismic and acoustic velocities in reservoir rocks, Volume 1: Experimental studies, Geophysics Reprint Series no.10, Soc. of Expl. Geophys.
Nur, A., G. Mavko, J. Dvorkin, and D. Galmudi, 1998, Critical porosity: A key to relating physical properties to porosity in rocks: The Leading Edge, 17, 3, 357-362.
O'Connell, R. and B. Budiansky, 1974, Seismic velocities in dry and saturated cracked solids, Journal of Geophysical Research, 79, 5412-5426.
Ødegaard, E. and P. Avseth, 2003, Interpretation of Elastic Inversion Results Using Rock Physics Templates: 65th EAGE conference and Exhibition. Paper E-17.
Olsen, C., T. Hongdul, I. L. Fabricius, 2008, Prediction of Archie's cementation factor from porosity and permeability through specific surface: Geophysics, 73, 2, E81-E87.
Palmer, T., and N. Pallat, 1991, The effect of overburden pressure on formation factor for shaly sands, Trans. 14th European Formation Evaluation Symposium, London, paper M.
Parkhomenko, E. I., 1967, Electrical Properties of Rocks: Monographs in Geosciences. Plenum Press. New York. Translated by George V. Keller.

Pearson, C. F., Halleck, P. M, McGuire, P. L, Hermes, R. E. and Mathews, M. A., 1983, Natural gas hydrate deposits: a review of in situ properties: J. of Physical Chemistry, 87, 21, 4180-4185.

Pickett, G. R., 1972, Practical formation evaluation: G.R. Pickett Inc., Golden, Colorado.

Polak and Rapoport, 1961, On the relation of the velocity of elastic waves to some physical properties of sedimentary rocks: Prikl. Geofiz., V.29.

Polak and Rapoport, 1956, On the relation between electrical and elastic properties in sedimentary rocks: Prikl. Geofiz., V.15.

Prensky, S., 1995, A review of gas hydrates and formation evaluation of hydrate-bearing reservoirs: Transactions of the SPWLA Annual Logging Symposium, vol.36, pp.GGG1-GGG12, Jun 1995.

Raiga-Clemenceau, J., 1977, The cementation exponent in the formation factor – porosity relation: The effect of permeability: Proc. SPWLA 18th Ann. Meeting, paper R.

Ransom, R., 1984, A contribution towards a better understanding of the modified Archie formation resistivity factor relationship: The Log Analyst, 25, 2, 7-12.

Raymer, D., E. Hunt, and J. Gardner, 1980, An improved sonic transit time-to-porosity transform: Proc. SPWLA 21st Ann. Meeting, paper P.

Revil, A., and P. Glover, 1997, Theory of ionic-surface electrical conduction in porous media: Physical Review B, 55, 3, 1757-1773.

Riedel, M., E. Willoughby, M. Chen, T. He, I. Novosel, K. Schwalenberg, R. Hyndman, G. Spence, N. Chapman, and R. Edwards, 2006, Gas hydrate on the northern Cascadia margin: regional geophysics and structural framework. *In* Riedel, M., Collett, T.S., Malone, M.J., and the Expedition 311 Scientists, *Proc. IODP*, 311: Washington, DC (Integrated Ocean Drilling Program Management International, Inc.).

Ruiz, F., and J. Dvorkin, 2007, Rock-physics model for deep-sea shallow calcareous sediment with porous grains: SEG Annual Meeting, 1599-1603.

Schön, J.H., 1996, Physical properties of rocks: Fundamentals and Principles of Petrophysics: Handbook of Geophysical Exploration. Section I, Seismic Exploration: v.18.

Schwartz, L., P. Sen, and D. Johnson, 1989, Influence of rough surface on electrolytic conduction in porous media: Physical Review B, 40, 4, 2450-2458.

Sen, P. N., 1997, Resistivity of partially saturated carbonate rocks with microporosity: Geophysics, 62, no.2, 415-425.

Sharma, M., A. Garrouch, and H. Dunlap, 1991, Effects of wettability, pore geometry, and stress on electrical conduction in fluid-saturated rocks: The Log Analyst, 511-526.

Sheng, P., and A. J. Callegari, 1984, Differential effective medium theory of sedimentary rocks: Appl. Phys. Lett., 44, 738-740.

Spangenberg, E., 2001, Modeling of the influence of gas hydrate content on the electrical properties of porous sediments: Journal of Geophysical Research, vol.106, no.B4, pp.6535-6548, 10 Apr 2001

Spearing, M. and G. P. Matthews, 1991, Modelling Characteristic Properties of Sandstones: Transport in Porous Media, 6, 71-90.

Strack, K.-M., 1992, Exploration with deep transient electromagnetics: Methods in Geochemistry and Geophysics. Elsevier Science Publishers B. V.

Thomas, E.C., 2007, Clay minerals and their effect upon the electrical behavior of shaly sands: Class notes at Denver Well Logging Society.

Vanorio, T., C. Scotellaro, and G. Mavko, 2008, The effect of chemical and physical processes on the acoustic properties of carbonate rocks: The Leading Edge, 27, 8, 1040 – 1048.

Wang, Z. and A. Nur, 1992, Seismic and acoustic velocities in reservoir rocks, Volume 2: Theoretical and Model Studies, Geophysics Reprint Series no.10, Soc. of Expl. Geophys.

Wang, Z. and A. Nur, 2000, Seismic and acoustic velocities in reservoir rocks, Volume 3: Recent Developments, Geophysics Reprint Series no.19, Soc. of Expl. Geophys.

Waxman, M., and L. Smits, 1968, Electrical conductivities in oil-bearing shaly sands: Soc. Petrol. Eng. J., 243, 107-122.

Waxman, M., and E.C. Thomas, 1974, Electrical conductivities in shaly sands: Journal of Petroleum Technology, 213.

Wempe, W., 2000, Predicting flow properties using geophysical data improving aquifer characterization: Ph.D. Dissertation, Dpt. of Geophysics, Stanford University.

Winsauer, W., H. Shearin, P. Masson, and M. Williams, 1952, Resistivity of brine-saturated sands in relation to pore geometry: Bull. Am. Assoc. Petr. Geologists, 36, 2, 253-277.

Winters, W. J., S. Dallimore, T. Collett, K. Jenner, J. Katsube, R. Cranston, J. Wright, F. Nixon, and T. Uchida, 2000, Relation between gas hydrate and physical properties at the Mallik 2L-38 research well in the Mackenzie Delta: Annals New York Academy of Sciences, 94-100.

Worthington, P, 1993, The uses and abuses of the Archie equations; 1, The formation factor-porosity relationship: Journal of Applied Geophysics, 30, 215-228.

Worthington, P, 1997, Petrophysical estimation of permeability as a function of scale: Developments in Petrophysics, edited by M.A. Lovell & P.K. Harvey. Geological Society Special Publications, 22.

Wyllie, M. and A. Gregory, 1953, Formation factors of unconsolidated porous media: Influence of particle shape and effect of cementation: Transactions of AIME, 198, 103-110.

Wyllie, M., A. Gregory, and G. Gardner, 1956, Elastic wave velocities in heterogeneous and porous media: Geophysics, 21, 41-70.

Wyllie, M., A. Gregory, and G. Gardner, 1958, An experimental investigation of factors affecting elastic wave velocities in porous media: Geophysics, 23, 459-493.

Wyllie, M., G. Gardner, and A. Gregory, 1963, Studies of elastic wave attenuation in porous media: Geophysics, 27, 569-589.

Yilmaz, O., 2001, Seismic data Analysis: Investigations in geophysics, 10, Soc. of Expl. Geop.